Phonon-protected superconducting qubits

Mutasem Odeh

Electrical Engineering and Computer Sciences
University of California, Berkeley

Technical Report No. UCB/EECS-2023-269
http://www2.eecs.berkeley.edu/Pubs/TechRpts/2023/EECS-2023-269.html

December 14, 2023

Phonon-protected superconducting qubits

by

Mutasem Odeh

A dissertation submitted in partial satisfaction of the

requirements for the degree of

Doctor of Philosophy

in

Engineering – Electrical Engineering and Computer Sciences

in the

Graduate Division

of the

University of California, Berkeley

Committee in charge:

Professor Alp Sipahigil, Chair
Professor Ming C. Wu
Professor Hartmut Haeffner

Fall 2023

Phonon-protected superconducting qubits

Abstract

Phonon-protected superconducting qubits

by

Mutasem Odeh

Doctor of Philosophy in Engineering – Electrical Engineering and Computer Sciences

University of California, Berkeley

Professor Alp Sipahigil, Chair

The overhead to construct a logical qubit from physical qubits rapidly increases with the decoherence rate. Current superconducting qubits reduce dissipation due to two-level systems (TLSs) by using large device footprints. However, this approach provides partial protection, and results in a trade-off between qubit footprint and dissipation. This work introduces a new platform using phononics to engineer superconducting qubit-TLS interactions. We realize a superconducting qubit on a phononic bandgap metamaterial that suppresses TLS-mediated phonon emission. We use the qubit to probe its thermalization dynamics with the phonon-engineered TLS bath. Inside the phononic bandgap, we observe the emergence of non-Markovian qubit dynamics due to the Purcell-engineered TLS lifetime of 34 µs. We discuss the implications of these observations for extending qubit relaxation times through simultaneous phonon protection and miniaturization.

To my parents, Ayed and Kefah.

Contents

List of Figures

List of Tables

Acknowledgments

I am indebted to my advisor, Alp Sipahigil, for giving me the opportunity to work on this project and guiding me through its obscure valleys. Alp is not only a talented experimental quantum physicist but also a skilled engineer in cryogenics, nanofabrication, and optical/microwave instrument design and setup, from whom I have learned a considerable amount through his innumerable suggestions and methods of thinking. I extend my appreciation to my thesis committee members, Ming Wu, Hartmut Haeffner, and Ali Niknejad for their feedback and constructive criticism. I would also like to thank Boubacar Kanté, for the opportunity to work and learn the craft of integrated photonics and metasurface designs, as well as Eli Yablonovitch, for his engineering insights and unparalleled skill in deconstructing complex ideas to their simplest form.

The need to establish new research laboratories led to the involvement of a large number of people to whom I am deeply grateful. I appreciate their generous giving of time and talent in building a robust and reliable research infrastructure. A recognition to the microwave team starting with Eric Li who carried out the initial design and optimization of phononic crystal, Kadircan Godeneli for TLS-piezoelectricity calculation, Rohin Tangirala for instrument control, and Binhan Hua for sample stage design. This year, we were fortunate to have three talented post-docs join our group whose contributions are already evident in the tedious task of wiring and installing our first dilution fridge unit and ensuring its proper operation. Zihuai Zhang, Haoxin Zhou, and Sherry Zhang, I am much obliged. I extend my appreciation to the optics team who conduct fascinating research on color-center in silicon photonics, to Polnop Samutpraphoot, Lukasz Komza, Jiu Chang, Auden Young, Milena Mathew, Hanbin Song, Yu-Lung Tang, and Yiyang Zhi. I must not forget to acknowledge my colleagues during my work on photonics and metasurfaces, Abdoulaye Ndao, Zhetao Jia, Rushin Contractor, Wanwoo Noh, and Walid Redjem, thank you all for your tangible and intangible positive influence and stimulation of everyday activities.

Pooling resources and technical know-how from our immediate surroundings was imperative for the completion of this work, manifested itself through countless suggestions, many small but several crucial, yet all most valued. My appreciation goes to Irfan Siddiqi and his group for the access of their double-angle evaporator. In particular, to Zahra Pedramrazi, Larry Chen, John Mark, Christian Jünger, and Linus Hyunseong Kim for generously sharing their expertise on Josephson junction and bandaid fabrication. I am grateful to Kasra Nowrouzi, Alexei Marchenkov, and Frank Ogletree at Lawrence Berkeley National Laboratory for their assistance in my initial cooldowns. Not to forget my nanolab fellows, Joseph Schaadt, Nirmaan Shanker, and Suraj Cheema, for their companionship in the clean room over the many nights; Lars Tatum, Jordan Edmund, Steve Volkman, and Sam Tsitrin for their detailed discussions and contributions to the process development of epitaxial Si/SiGe films; Allison Dove and Joanna Bettinger for the valuable lithography tips; Ryan Rivers for the guidance of etch process development; and to the rest of the nanolab staff, who ensure the cleanroom's impossible infrastructure that tend to always break, stands still and robust to serve the researchers.

Arguably, I wouldn't have been able to fulfill the degree requirements without the help and support I received from Shirley Salanio, our EECS graduate director. Shirley is a remarkable person, and her role in ensuring an otherwise turbulent student's journey to be smooth and peaceful, is often dismissed. Thank you, Shirley, I will always be in your debt. Another remarkable person I was fortunate to cross paths with is Leen Ajlouni. Leen exemplified perseverance during hardship and reminded me of my original motives in pursuing higher education; the search for significance and the pursuit of genuine impact. Thank you for your support, Leen, and congratulations on your graduate admission at Tuck school.

To my grandmother, who suddenly and sadly left this world during my Ph.D. study. She didn't know how to read or write, but It was with her when we engineered my first kite. She taught me so much about love, laughter, and what really matters in life. Lastly and most importantly, to my parents, siblings, and nephews, for whom the publication of this dissertation brings to an end a cause of missed companionship. I dedicate this dissertation to their unwavering and unconditional support throughout this journey.

Publications

This dissertation expounds on the following article :

- **Mutasem Odeh**, Kadircan Godeneli, Eric Li, Rohin Tangirala, Haoxin Zhou, Xueyue Zhang, Zi-Huai Zhang, Alp Sipahigil "Non-Markovian dynamics of a superconducting qubit in a phononic bandgap," arXiv:2312.01031 (2023)

Article publications on various projects carried during my Ph.D. study:

- Lukasz Komza, Polnop Samutpraphoot, **Mutasem Odeh**, Yu-Lung Tang, Milena Mathew, Jiu Chang, Hanbin Song, Myung-Ki Kim, Yihuang Xiong, Geoffroy Hautier, and Alp Sipahigil " Indistinguishable photons from an artificial atom in silicon photonics," arXiv:2211.09305 (2022)

- Qinghua Song, **Mutasem Odeh**, Jesus Zuniga-Perez, Boubacar Kante, and Genevet, "Plasmonic Topological Metasurface by Encircling an Exceptional Point," *Science* 373, 1133-1137 (2021).

- **Mutasem Odeh**, Matthieu Dupré, Kevin Kim, and Boubacar Kanté, "Optical Response of Jammed Rectangular Nanostructures," *Nanophotonics* 10, 705-711 (2020)

Chapter 1

Introduction

1.1 Background and motivation

The history of superconductivity dates back to the groundbreaking discovery made by Heike Kamerlingh Onnes in 1911 when he observed the abrupt loss of DC resistance in certain metals as they were cooled below a specific temperature, coining the phenomenon as "superconductivity" [1]. Over the following decades, this discovery cultivated experimental and theoretical interest in superconductivity spread among physicists. A major milestone was reached with the development of the BCS theory by John Bardeen, Leon Cooper, and John Robert Schrieffer in 1957, providing a theoretical explanation for superconductivity based on the formation of Cooper pairs of electrons [2]. In 1962, Brian Josephson suggested that it should be possible for Cooper pairs to tunnel between closely spaced superconductors even in the absence of a potential difference [3]. Shortly after, Anderson and Rowell experimentally verified the effect at Bell Labs in 1964 [4]. The Josephson effect quickly found applications in classical electronics, including millimeter-wave receivers, magnetometers, and the establishment of the voltage standard. A thorough coverage of the classical application of superconductivity can be best found in Theodore Van Duzer's textbook *"Principles of Superconductive Devices and Circuits"* [5].

In 1985, John Clarke, Michel Devoret, and John Martinis at UC Berkeley reported the first observation of quantized energy levels for the phase difference across a current-biased Josephson junction in its zero-voltage state [7]. This was a key milestone in using the Josephson effect to engineer artificial atoms for quantum applications. It was not until 1999 that time-resolved coherent oscillation in a cooper-pair box was observed by Yasunobu Nakamura, Yuri Pashkin, and Jaw-Shen Tsai at NEC Labs in Japan [8], resembling an artificial atom with a coherence time of 2 ns. The modern and stable version of the charge qubit is the transmon qubit which exhibits reduced sensitivity to charge noise and was developed at Yale University in 2006 by Rob Schoelkopf, Michel Devoret, and Steve Girvin [9]. The field flourished thereafter and various qubit topologies and fabrication techniques were developed, pushing the coherence time up to a couple of hundreds microseconds with

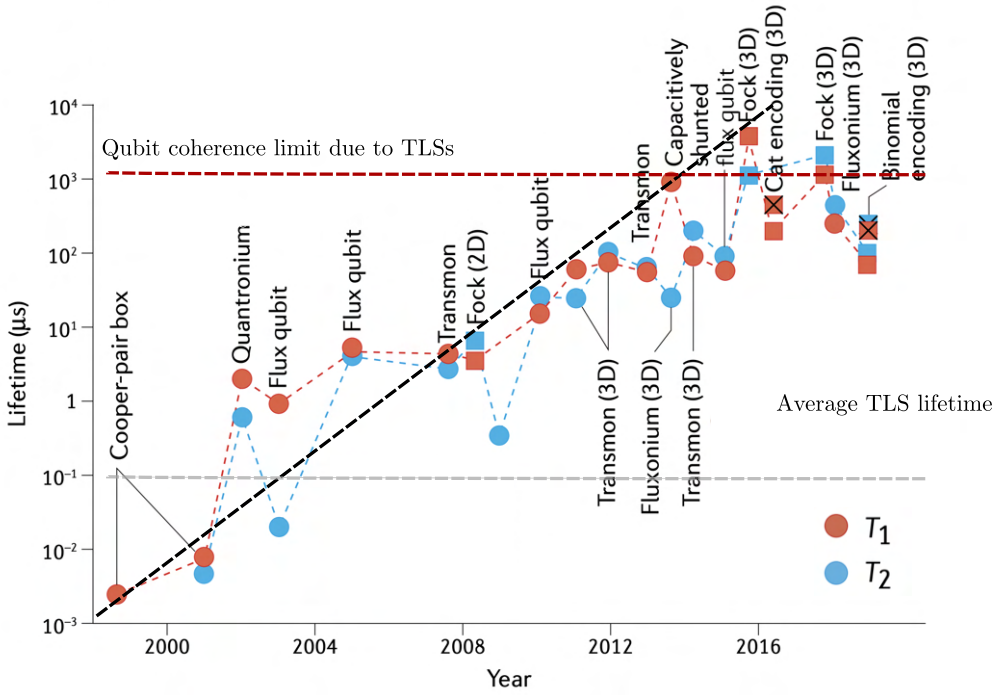

Figure 1.1: Coherence time evolution (T_1, T_2) of superconducting qubit over the past few decads, adapted from [6].

above 99 % single and two-qubit gate fidelities.

Achieving high-coherence physical qubits enables building error-corrected logical qubits, which serve as the building blocks for a fault-tolerant quantum processor that is ideally capable of running arbitrarily long computations to arbitrary precision. The computational space of a quantum processor grows as 2^N for N logical qubits. Superposition and entanglement between the qubits enable parallel computation for selected problems that cannot be attained by classical computational methods. For example, the quantum search algorithm developed by Grover requires only $\mathcal{O}(\sqrt{n})$ steps instead of $\mathcal{O}(n)$ on a classical computer[10]. Simple quantum algorithms have been implemented [11, 12], demonstrations of quantum error correction have been approached [13], and quantum supremacy has been claimed [14]. However, further advancement necessitates significant improvements in the underlying physical qubits coherence and relaxation times, which witnessed limited improvement over the last decade, as can be noticed from Fig. 1.1. There are many sources of qubit decoherence, but evidence always points to one major culprit: Two-level systems.

Tunneling two-level systems (TLSs) are commonly understood to be defects consisting of a single atom or a group of atoms that can tunnel between two sites within disordered or amorphous solids. TLSs are present on interfaces, surfaces, or within bulk dielectrics such

as deposited films or substrates, and are known to contain both elastic and electric dipole moments and a broad spectrum of tunneling states. Their discovery is not particularly new, and their signature was visible when measuring the specific heat of glassy non-crystalline solids at cryogenic temperatures [15]. The revived interest in TLS within the superconducting qubit community is due to their detrimental influence on qubit coherence. TLS act like tiny piezoelectric transducers that mediate qubit coupling to a dissipative phononic bath [16].

Categorically, there are two major approaches to address the TLS issue in superconducting qubit devices: (i) reducing TLS presence through proper material selection and careful fabrication flow [17, 18]; and (ii) reducing qubit-TLS electric-field coupling via larger qubit geometry [19]. In this thesis, we investigate a novel third approach that focuses on suppressing the TLS relaxation rate via the use of a phononic bandgap metamaterial, which in return, causes a Purcell enhancement of the qubit lifetime under certain conditions.

1.2 Thesis overview

In Chapter 2, we review the essential theories related to this work. We begin by examining concepts in circuit quantum electrodynamics, the standard tunneling model of TLS, methods for open quantum systems, and the design principles of phononic bandgap metamaterials and their usage in shielding superconducting quantum devices. In Chapter 3, we discuss material choice, fabrication flow, process optimization, and device packaging of a phonon-protected superconducting qubit on a full-bandgap phononic metamaterial using a silicon-on-insulator platform. Additionally, we investigate epitaxial Si/SiGe superlattice as a 1D phonon shield. Chapter 4 delves into the experimental setup which comprises a ^{3}He$-^4$He dilution refrigerator and an FPGA-based microwave controller that is used for time-domain and frequency-domain device characterization. The key experimental results are presented in Chapter 5, while Chapter 6 concludes and summarizes the work with an outlook for future directions.

Chapter 2

Theory of a phonon-protected qubits

This chapter provides a pedagogical presentation of the theories related to phonon-protected superconducting qubits. The chapter commences with a brief discussion of the field of circuit quantum electrodynamics (cQED) with an emphasis on transmon qubits, the Jaynes–Cummings (JC) model, and the standard tunneling model of defect two-level system (TLS). A subsequent section briefly presents the main methods to deal with open quantum systems with an emphasis on TLS incoherent interactions and the Solomon equations. Next, the chapter introduces the theory of phononic bandgap metamaterial and its usage in suppressing TLS phonon decay. The final section discusses the design of the phonon-protected superconducting qubit that is studied in this thesis. More detailed discussions and derivations can be found in Refs [20, 21, 22, 23].

2.1 Circuit quantum electrodynamics

The field of circuit quantum electrodynamics (cQED) is a rapidly progressing area of research that explores the interaction between quantized electromagnetic fields and artificial atoms in the microwave frequency range. A typical qubit system consists of a non-linear resonator (e.g., transmon) that is capacitively coupled to a linear readout resonator. The readout resonator is used to read the qubit state while protecting it from decoherence. The interaction is best described by the Jaynes-Cummings model, which is presented in this chapter. In practice, the frequency range in such systems is between 2–10 GHz, with spatial dimensions on the order of a sub/few wavelengths ($\sim$1–10 mm). This justifies the usage of a simple lumped-element circuit representation of the system while maintaining high description accuracy. Furthermore, several classical circuit analysis techniques and simulation methods can be applied to aid in the design of complex quantum systems.

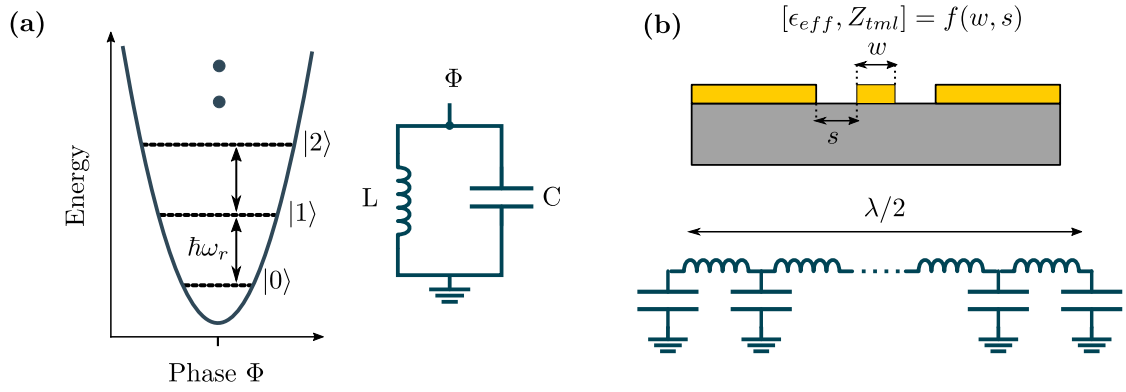

Figure 2.1: Quantum harmonic oscillator: (a) energy levels of lumped LC resonator, and (b) $\lambda/2$ coplanar waveguide transmission line resonator.

2.1.1 Quantum harmonic oscillator

A quantum harmonic oscillator is a physical system that consists of a particle (microwave photon in this case) moving in a quadratic energy potential. A simple parallel LC resonator with inductance L and capacitance C carries such potential, as illustrated in Fig. 2.1(a). The angular resonant frequency is $\omega_r = 1/\sqrt{LC}$ and the characteristic impedance is $Z_r = \sqrt{L/C}$. The total energy in the system is the sum of the capacitor energy $E_C = Q^2/2C$ and the inductor energy $E_L = \Phi^2/2L$, noting the charge $Q(t) = \int_{t_0}^{t} dt' I(t')$ and the flux $\Phi(t) = \int_{t_0}^{t} dt' V(t')$. Trusting Dirac's wisdom in quantization and promoting the charge and flux variables to noncommuting observables that satisfy the commutation relation $[\hat{\Phi}, \hat{Q}] = i\hbar$, the quantized Hamiltonian is

$$\hat{H}_{LC} = \underbrace{\frac{\hat{Q}^2}{2C}}_{E_C} + \underbrace{\frac{\hat{\Phi}^2}{2L}}_{E_L} \tag{2.1}$$

It is useful to recast the Hamiltonian in terms of the creation ($\hat{a}^\dagger$) and annihilation ($\hat{a}$) operators that create or remove a photon of energy ω_r from the LC resonator. The relations are

$$\hat{\Phi} = \Phi_{zpf}(\hat{a}^\dagger + \hat{a}), \quad \hat{Q} = iQ_{zpf}(\hat{a}^\dagger - \hat{a}) \tag{2.2}$$

with $\Phi_{zpf} = \sqrt{\hbar Z_r/2}$ and $Q_{zpf} = \sqrt{\hbar/2Z_r}$ being the characteristic magnitude of the zero-point fluctuations of the flux and the charge observables, respectively, satisfying the Heisenberg uncertainty $\Phi_{zpf}Q_{zpf} = \hbar/2$. High impedance resonators have large voltage fluctuations ($V_{zpf} = Q_{zpf}/2C = \omega\sqrt{\hbar Z/2} \approx 20 - 100\mu V$) and thus large electric-dipole interaction when

capacitively coupled to other qubits or resonators. With the newly defined operators, we can rewrite the Hamiltonian as

$$\hat{H}_{LC} = \hbar\omega_r(\hat{a}^\dagger\hat{a} + 1/2) \tag{2.3}$$

with eigenstates that satisfy $\hat{a}^\dagger\hat{a}\,|n\rangle = n\,|n\rangle$ for $n = 0, 1, 2, 3, ...$

Finite-length transmission lines (TL) are commonly used in building planar high-quality factor resonators. The structures host distinct resonant frequencies (similar to a two mirrors Fabry–Pérot cavity) and can be studied by normal mode decomposition where each normal mode can be thought of as an independent harmonic oscillator. The total Hamiltonian is $\hat{H}_{tml} = \sum_0^\infty H_{LC}^m = \sum_0^\infty \hbar\omega_m(\hat{a_m}^\dagger\hat{a_m})$ with ω_m being the frequency of the normal mode m and $\hat{a_m}^\dagger$, $\hat{a_m}$ are the creation and annihilation operator of that mode. In this thesis, we use $\lambda/2$ coplanar waveguide (CPW) TL resonators that has open boundaries at both of its ends, as illustrated in Fig. 2.1(b). The resonator characteristic impedance Z_{tml} and effective permittivity ϵ_{eff} are the two main properties of the TL that can be adjusted by controlling the trace width s and ground spacing w. For a TL of length l, the fundamental resonance frequency is $f_0 = c/2l\sqrt{\epsilon_{eff}}$. An expression for the resonator input impedance around f_0 can be approximated as in [24]

$$Z_{in} = Z_{tml}\coth(i\beta l) = \frac{Z_{tml}}{i(\Delta\omega\pi/\omega_0)}\Big|_{\omega\approx\omega_0} \tag{2.4}$$

The above simple single pole transfer function can be mapped to a parallel LC resonator with lumped capacitance and inductance of

$$C = \frac{\pi}{2\omega_0 Z_{tml}}, \quad L = \frac{2Z_{tml}}{\pi\omega_0} \tag{2.5}$$

2.1.2 Transmon qubit

The equal spacings of energy-levels in a quantum harmonic oscillator makes it challenging to confine the Hilbert space to the subspace of a two-level qubit system and observe quantum behavior. Breaking the equal energy spacing without introducing losses can be done via the Josephson junction (JJ) circuit element. The typical Josephson junction consists of two superconducting islands separated by a few nanometer-thick dielectric, as illustrated in Fig. 2.2(a). Brian Josephson showed that cooper pairs can tunnel between the islands without dissipation. The dynamics are given by the following two Josephson equations:

$$I = I_c\sin\phi, \tag{2.6}$$

$$\frac{\mathrm{d}\phi}{\mathrm{d}t} = \frac{2\pi}{\Phi_0}V \tag{2.7}$$

where I_c is the junction's critical current (the maximum current that the junction can support before cooper pairs are broken), ϕ is the phase difference between the two superconducting

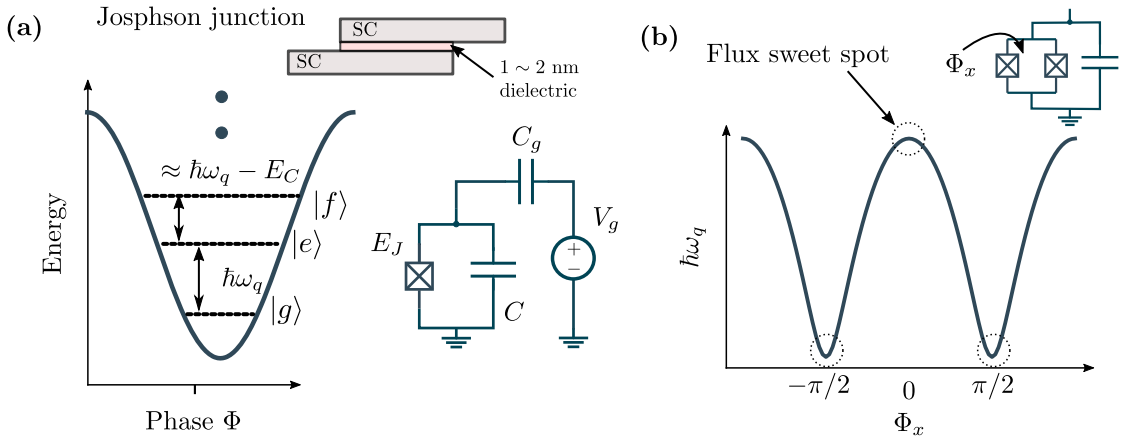

Figure 2.2: Transmon qubit: (a) circuit schematic and energy levels spacing, and (b) tunable transmon using a SQUID.

islands, and $\Phi_0 = h/2e$ is the flux quantum. We can deduce from these two equations the presence of dissipationless DC when $V = 0$, and a dissipationless AC when $V = V_0$ with a frequency of $f_j = V_0/\Phi_0$, as long as $I < I_c$. By integrating the second JJ equation and substituting it in the first JJ equation while noting that $\phi(t) = 2\pi\Phi(t)/\Phi_0$, we can see that the JJ is a nonlinear inductor that relates the current and phase through a Josephson inductance given by

$$L_J(\Phi) = \left(\frac{\partial I}{\partial \Phi}\right)^{-1} = \frac{\Phi_0}{2\pi I_c}\frac{1}{\cos(2\pi\Phi/\Phi_0)} \tag{2.8}$$

The energy stored in the JJ can then be calculated as

$$E = \int dt V(t) I(t) = I_c \int dt \left(\frac{\mathrm{d}\Phi}{\mathrm{d}t}\right) \sin\left(\frac{2\pi}{\Phi_0}\Phi\right) = -E_j \cos\left(\frac{2\pi}{\Phi_0}\Phi\right) \tag{2.9}$$

where $E_J = \Phi_0 I_c/2\pi$ is the Josephson energy. A simple qubit can be built by replacing the linear inductor in an LC resonator with the JJ non-linear inductor. Doing so will introduce inharmonicity that will break the equal energy spacing of the LC resonator, rendering the energy potential to be that of an artificial atom, as illustrated in Fig. 2.2(a). Substituting Eq. 2.9 in place of the inductive energy E_L in Eq. 2.1, we have

$$\begin{aligned} \hat{H}_T &= \frac{\hat{Q}^2}{2C} - E_j \cos\left(\frac{2\pi}{\Phi_0}\hat{\Phi}\right) \\ &= 4E_C\hat{n}^2 - E_j \cos\left(\frac{2\pi}{\Phi_0}\hat{\Phi}\right) \end{aligned} \tag{2.10}$$

where $E_C = e^2/2C$ is the charging energy, and $\hat{n} = \hat{Q}/2e$ is the charge number operator. The impedance can be obtained similar to the LC resonator by substituting the inductance

in Eq. 2.8 to obtain

$$Z_T = \frac{\Phi_0}{\pi e}\sqrt{\frac{E_C}{2E_J}} \tag{2.11}$$

The qubit impedance determines the amount of fluctuation in the Hamiltonian energy due to external charge or flux perturbations. Charge fluctuations in the qubit's environment are unavoidable and cause large perturbations in the energy levels leading to qubit dephasing. This can be mitigated by working in the transmon regime (low impedance qubit) where $E_J/E_C >> 1$ and can be attained using a large capacitor and a small JJ [9]. This can be seen from Eq. 2.10; when E_C is large, the eigenstates of the Hamiltonian are approximately equal to that of the charge operator, making it very sensitive to charge fluctuations in the environment. Working in the transmon regime will suppress the charge noise exponentially at the expense of weaker sacrifice of the inharmonicity $\sim (E_J/E_C)^{-1/2}$, rendering it one of the most used qubit modalities in highly coherent superconducting circuits.

The energy levels of $\hat{H_T}$ can be calculated numerically or obtained approximately with a polynomial expansion of the cosine terms, a discussion that we omit here and can be found in [20]. It can be shown that in the transmon regime with a typical ratio $E_J/E_C \approx 20-100$, the transmon frequency is

$$\omega_q \approx \sqrt{8E_C E_J}/\hbar - E_C/\hbar \tag{2.12}$$

with an inharmonicity of

$$\alpha = (E_{12} - E_{01})/\hbar \approx -E_C/\hbar \tag{2.13}$$

That inharmonicity $\alpha/2\pi$ falls in the range from 100–300 MHz which is larger than the transition linewidth and can be spectrally resolved.

Finally, the transmon energy levels can be made tunable by tuning the flux in a superconducting quantum interference device (SQUID) formed by a loop of two parallel JJs, as illustrated in Fig. 2.2(b). The qubit Hamiltonian is

$$\hat{H_T} = \frac{\hat{Q}^2}{2C} - E_{J1}\cos\left(\hat{\phi_1}\right) - E_{J2}\cos\left(\hat{\phi_2}\right) \tag{2.14}$$

In the presence of external flux Φ_x that penetrates the SQUID loop, flux quantization mandates that $\phi_1 - \phi_2 = 2\pi\Phi_x/\Phi_0 = 2\pi n$. The Hamiltonian can then be rewritten to resemble that of a fixed frequency transmon

$$\hat{H_T} = 4E_C\hat{n}^2 - E_j(\Phi_x)\cos\left(\hat{\phi} - \phi_0\right) \tag{2.15}$$

where the tunable Josephson energy $E_J(\Phi_x)$ is given by

$$E_J(\Phi_x) = E_{J\Sigma}\cos\left(\frac{\pi\Phi_x}{\Phi_0}\right)\sqrt{1 + d^2\tan^2(\frac{\pi\Phi_x}{\Phi_0})} \tag{2.16}$$

with $\hat{\phi} = (\hat{\phi_1} + \hat{\phi_2})/2$, $E_{J\Sigma} = E_{J1} + E_{J2}$, $d = (E_{J2} - E_{J1})/E_{J\Sigma}$, and $\phi_0 = d\tan(\pi\Phi_x/\Phi_0)$. Therefore, a SQUID loop in place of a single JJ represents a flux tunable transmon with

periodic frequency as a function of the threaded flux $\omega_q(\Phi_x) \approx \sqrt{8E_C|E_J(\Phi_x)|}/\hbar - E_C/\hbar$. We note that symmetric JJs ($d = 0$) in a SQUID loop allow tuning the qubit frequency from zero all the way to its maximum value, whereas asymmetric JJs ($d \neq 0$) reduce the tuning range with the benefit of desensitizing the qubit from flux noise. In both cases, however, there are regions termed as the *flux sweet spots*, where the dephasing vanishes to first order, resulting in an attractive region of qubit operation, as illustrated in Fig. 2.2(b).

2.1.3 Capacitive coupling

In cQED, we are often confronted with the task of finding the Hamiltonian of a system from its coupled simpler subsystems. There are two types of coupling axes in cQED: (i) transverse coupling ($\sigma_{x,y}\sigma_{x,y}$) which involves energy exchange and can be done via capacitive coupling ($H_{int} = C_g V_1 V_2$), and (ii) longitudinal coupling ($\sigma_z\sigma_z$) which doesn't involve energy exchange and can be done via mutual inductive coupling ($H_{int} = M_{12} I_1 I_2$) [21]. Transverse coupling is commonly used in cQED to couple a transmon qubit with a readout resonator, whereas longitudinal coupling is used to couple a flux line to the SQUID of a tunable transmon. In this section, we will focus on transversal coupling and find the Hamiltonian of a system from its capacitively coupled subsystems. Consider two LC resonators, a and b, that are capacitively coupled with capacitance C_g, as illustrated in Fig. 2.3. In the limit of weak coupling ($C_g \ll C_a, C_b$), it can be shown that the system Hamiltonian [20]:

$$\hat{H} = \hat{H}_a + \hat{H}_b + \hat{H}_{int} \tag{2.17}$$

with

$$\hat{H}_{int} = \frac{C_g}{C_a C_b} \hat{Q}_a \hat{Q}_b \tag{2.18}$$

Substituting the charge operator of LC resonator $\hat{Q}$ and applying the rotating-wave approximation (RWA), we obtain

$$\begin{aligned} \hat{H}_{int} &= -\frac{C_g}{C_a C_b} Q^a_{zpf} Q^b_{zpf} (\hat{a}^\dagger - \hat{a})(\hat{b}^\dagger - \hat{b}) \\ \hat{H}_{int} &\approx -\hbar g (\hat{b}^\dagger \hat{a} + \hat{b}\hat{a}^\dagger) \end{aligned} \tag{2.19}$$

with the single photon-rabi frequency

$$\boxed{g = \frac{C_g}{C_a C_b} \frac{Q^a_{zpf} Q^b_{zpf}}{\hbar}} \tag{2.20}$$

The capacitive interaction can be generalized to other subsystems, and can be simply obtained by substituting the proper charge operator $\hat{Q}$ in Eq. 2.18 with that of involved subsystems. Here we list the operators for the LC resonator, truncated transmon (TLS), voltage drive source, and infinite transmission line. We will explain the origin of the last two in the following sections.

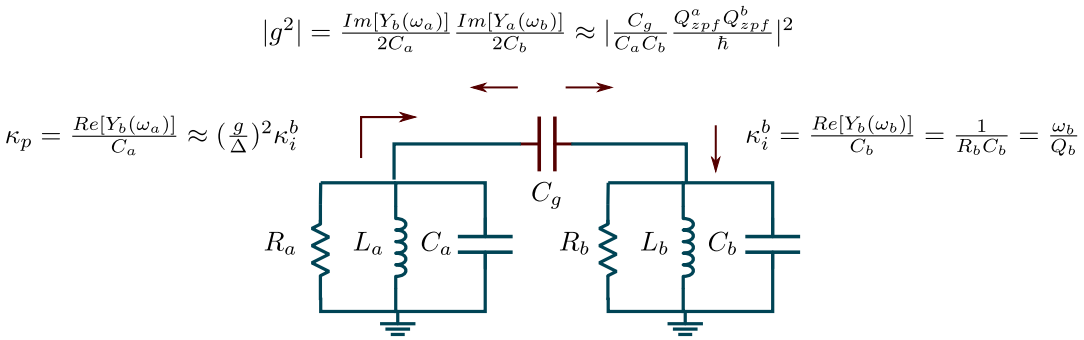

Figure 2.3: Capacitive coupling of two dissipative LC resonators.

$$\hat{Q}_{LC} = i\sqrt{\frac{\hbar}{2Z_r}}(\hat{a}^\dagger - \hat{a}), \tag{2.21a}$$

$$\hat{Q}_T = i\sqrt{\frac{\hbar}{2Z_T}}(\hat{\sigma}^+ - \hat{\sigma}^-), \tag{2.21b}$$

$$Q_{drive} = C_d V_d, \tag{2.21c}$$

$$\hat{Q}_{tml}(x) = i\int_0^\infty d\omega \sqrt{\frac{\hbar\omega c}{\pi v}}\cos\Big(\frac{\omega x}{v}\Big)(\hat{b}^\dagger_\omega - \hat{b}_\omega) \tag{2.21d}$$

2.1.4 Classical circuit analysis

For more complex circuits, the magnitude of the coupling strength $|g|$ can be obtained from classical circuit analysis and takes the following general form

$$\boxed{|g(\omega_r)|^2 = \frac{Im[Y_b(\omega_a)]}{2C_a}\frac{Im[Y_a(\omega_b)]}{2C_b}} \tag{2.22}$$

We note that $Y_b(\omega_a)$ is the admittance of subsystem b seen by the eye of subsystem a (Including C_g) at the frequency of system a. Vice versa for $Y_a(\omega_b)$ as illustrated in Fig. 2.3. To arrive at the expression of Eq. 2.20 using Eq. 2.22, we have to assume the states are dressed and not entangled which occurs at: (i) large detuning ($|\omega_a - \omega_b| \gg g$)and (ii) weak coupling $C_g \ll C_a, C_b$. In this limit $Y_b(\omega_a) \approx \omega_a C_g$ and $Y_a(\omega_b) \approx \omega_b C_g$ from which Eq. 2.20 directly follow.

Finally, and as we will see in the following sections, the real part of the admittance is related to ohmic losses and thus dissipation, as illustrated in Fig. 2.3. An important expression that allows us to extract the quality factor of a resonator due to self dissipation is:

$$\boxed{\kappa_i^b = \frac{Re[Y_b(\omega_b)]}{C_b} = \frac{\omega_b}{Q_b}} \tag{2.23}$$

Similarly, cross dissipation (Purcell decay), which accounts for the dissipation of one system through another, takes the following form [25]:

$$\boxed{\kappa_p = \frac{Re[Y_b(\omega_a)]}{C_a}} \tag{2.24}$$

2.1.5 Driven two-level system

Let us assume that we capacitively couple a voltage source to a transmon, as illustrated in Fig. 2.2(a). The system Hamiltonian can be constructed from the subsystems by substituting Eq. 2.21(b) and (c) in Eq. 2.18, truncate the energy levels to the first two, and note that $(\hat{\sigma}^+ - \hat{\sigma}^-) = -i\hat{\sigma}_y$, we have

$$\hat{H}_d = \frac{-\hbar\omega_q}{2}\hat{\sigma}_z + \Omega(t)\hat{\sigma}_y \tag{2.25}$$

where ω_q is the transmon frequency and $\Omega(t)$ is time dependent Rabi frequency and is given by

$$\Omega(t) = gV_g(t) = \frac{C_g}{\hbar C}\sqrt{\frac{\hbar}{2Z_T}}V_g(t) \tag{2.26}$$

Because we are interested only in the effect of the external drive, we hide the time dependence of the transmon evolution by entering the rotating frame through the rotation operator $\hat{R} = \exp(-i\omega_q t\hat{\sigma}_z/2)$

$$\hat{H}_{int} = \hat{R}\hat{H}_d\hat{R}^\dagger = \hbar\Omega(t)e^{-i\omega t\hat{\sigma}_z/2}\hat{\sigma}_y e^{i\omega t\hat{\sigma}_z/2} \tag{2.27}$$

Assuming the drive is $\Omega(t) = \Omega_0\sin(\omega t + \phi)$ with detuning $\delta\omega = \omega - \omega_q$, substituting in the previous equation, and eliminating the 2ω terms (RWA), we have

$$\hat{H}_{int} = \frac{-\hbar\Omega_0}{2}(\cos(\delta\omega t + \phi)\hat{\sigma}_x - \sin(\delta\omega t + \phi)\hat{\sigma}_y) \tag{2.28}$$

On-resonance ($\delta\omega = 0$), the drive leads to a purely latitudinal rotation on the Bloch sphere with an axis of rotation determined by the phase of the drive ϕ and rotation frequency of $\Omega_0/2\pi$. Finally, when the qubit frequency does not match the drive frequency $\delta\omega \neq 0$, the Hamiltonian H_{int} has a residual $\hat{\sigma}_z$ and the rotation axis will be outside the XY plan precessing at a frequency $\delta\omega\hat{\sigma}_z/2$.

2.1.6 Jaynes–Cummings model

Capacitive coupling of a readout resonator to a qubit is a commonly deployed method to read the qubit state. In the presence of a resonator tone, the qubit state can be measured and preserved, whereas, in the absence of a resonator tone, the qubit evolves freely with high coherence, leading in principle to a quantum nondemolition (QND) measurement scheme. The Jaynes–Cummings model is an exactly solvable model that describes such interaction and is discussed in this section. Consider a two-level system coupled to an LC resonator as

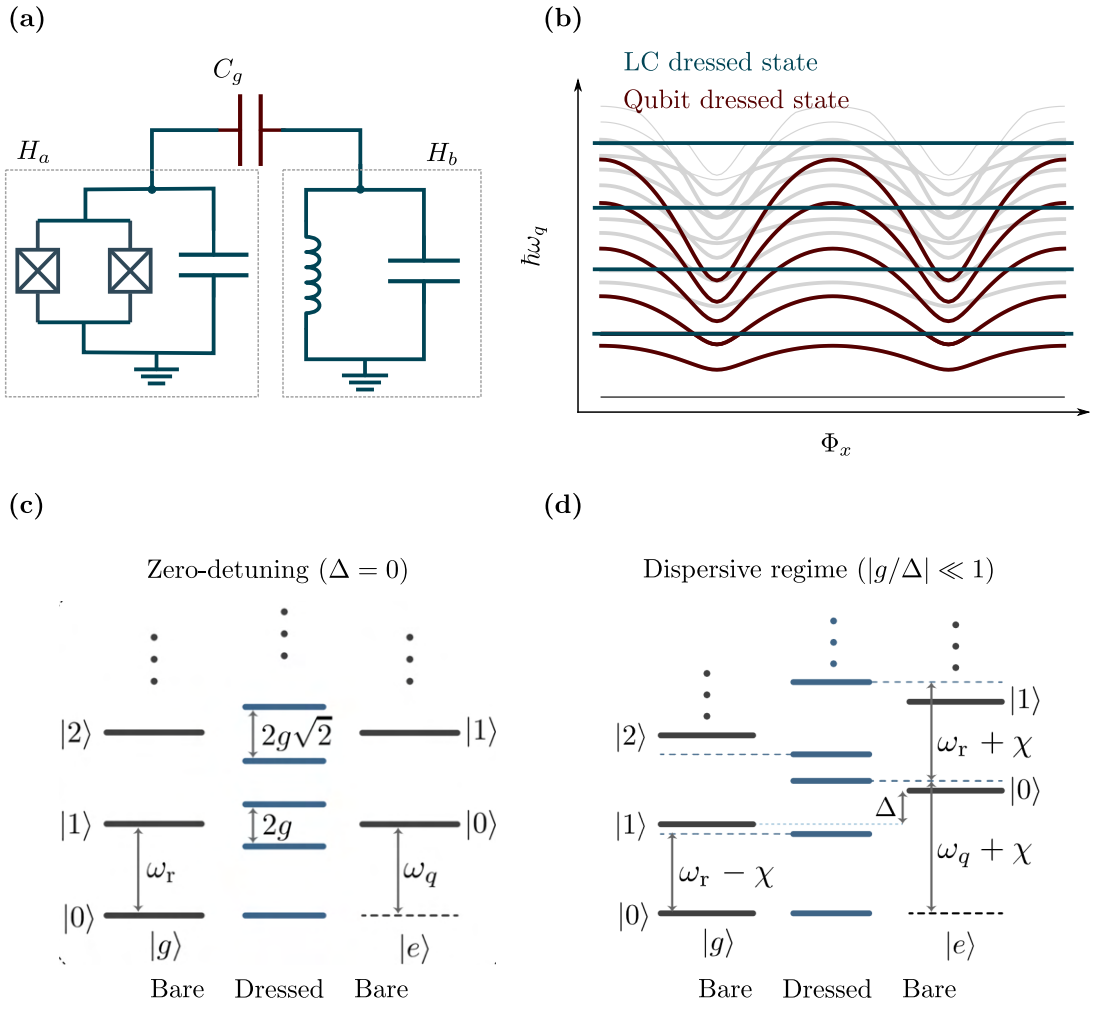

Figure 2.4: Jaynes–Cummings model: (a) schematic of resonator-transmon qubit system, (b) energy levels in the dispersive regime, (c) energy spectrum at zero detuning $\Delta = 0$, and (d) energy spectrum in the dispersive limit $|g/\Delta| \ll 1$.

illustrated in Fig. 2.4(a). We can obtain the Hamiltonian of the system from its subsystems by substituting Eq. 2.21(a) and (b) in Eq. 2.18 to obtain

$$\hat{H}_{JC} = \underbrace{\hbar\omega_r \hat{a}^\dagger \hat{a}}_{\text{field}} + \underbrace{\frac{\hbar\omega_q}{2}\hat{\sigma}_z}_{\text{atom}} + \underbrace{\hbar g(\hat{a}^\dagger \hat{\sigma}_- + \hat{a}\hat{\sigma}_+)}_{\text{interaction}} \tag{2.29}$$

with $\hat{\sigma}_+ = |e\rangle\langle g|$, $\hat{\sigma}_- = |g\rangle\langle e|$, $\hat{\sigma}_z = |e\rangle\langle e| - |g\rangle\langle g|$, and the single-photon Rabi frequency

$$\begin{aligned} g &= \frac{C_g}{2C_rC_T}\sqrt{\frac{1}{Z_rZ_T}} \\ &= \omega_r\frac{C_g}{C_T}(\frac{E_J}{2E_C})^{1/4}\sqrt{\frac{\pi Z_r}{R_k}} \end{aligned} \tag{2.30}$$

where the resistance quantum $R_k = h/e^2 \approx 25.8\,\mathrm{k}\Omega$. The above Hamiltonian is exactly solvable and can be diagonalized via Bogoliubov-like unitary transformation of the bare states [20]. The spectrum consists of dressed state doublets $|\overline{g,n}\rangle, |\overline{e,n-1}\rangle$ with eigen energies

$$\begin{aligned} E_{\overline{g,n}} &= \hbar n\omega_r - \frac{\hbar}{2}\sqrt{\Delta^2 + 4g^2n} \\ E_{\overline{e,n-1}} &= \hbar n\omega_r + \frac{\hbar}{2}\sqrt{\Delta^2 + 4g^2n} \end{aligned} \tag{2.31}$$

and eigenstates

$$\begin{aligned} |\overline{g,n}\rangle &= \cos(\theta_n/2)\,|g,n\rangle - \sin(\theta_n/2)\,|e,n-1\rangle \\ |\overline{e,n-1}\rangle &= \sin(\theta_n/2)\,|g,n\rangle + \cos(\theta_n/2)\,|e,n-1\rangle \end{aligned} \tag{2.32}$$

where $\theta_n = \arctan(2g\sqrt{n}/\Delta)$.

On resonance ($\Delta = 0$), the dressed states are maximally entangled and the energy splitting is $2g\sqrt{n}$, as illustrated in Fig. 2.4(c). However, the transmon is typically operated in the dispersive regime ($|g/\Delta| \ll 1$), where the qubit and resonator are weakly entangled and maintain approximately their original eigenstates with slight dispersive shift χ in their eigenenergies, as shown in Fig. 2.4(b) and (d). Applying Taylor expansion ($\sqrt{1+x} \approx 1 + x/2$) to Eq. 2.31, the dress state eigen energies are:

$$\begin{aligned} \bar{\omega_r} &= \omega_r \pm \chi, \\ \bar{\omega_q} &= \omega_q + \chi, \\ \chi &= \frac{g^2}{\Delta}, \\ n_{crit} &= (\frac{\Delta}{2g})^2, \end{aligned} \tag{2.33}$$

where the dispersive approximation is valid when the number of photons in the cavity $n \ll n_{crit}$. It is now clear to see that the resonator frequency shift by 2χ when the qubit state change from the ground state $|g\rangle$ to the excited state $|e\rangle$. This forms the base of measurement in modern superconducting qubits. We also note the qubit frequency is also Lamb shifted by χ when $n = 0$ and by an additional AC-Stark shift when $n \neq 0$.

Typically, the amount of dispersive shift differs significantly from the simplified JC model due to the multilevel nature of the transmon. We use the SCqubit python package to compute the energy levels precisely. An approximate analytical expression can also be obtained

by Schrieffer-Wolff or Bogoliubov transformation, leading to the following dispersive Hamiltonian [20]:

$$\hat{H}_{JC} \approx \hbar\bar{\omega_r}\hat{a}^\dagger\hat{a} + \frac{\hbar\bar{\omega_q}}{2}\hat{\sigma}_z + \hbar\chi\hat{a}^\dagger\hat{a}\hat{\sigma}_z \tag{2.34}$$

The crucial observation is that in the dispersive limit, the term commutes with σ_z. This guarantees that the interaction does not change the qubit state during the measurement operation. The corrected eigenenergies are

$$\begin{aligned}
\bar{\omega_r} &= \omega_r - \frac{g^2}{\Delta+\alpha} \\
\bar{\omega_q} &= \omega_q + \frac{g^2}{\Delta} \\
\chi &= -\frac{g^2 E_C/\hbar}{\Delta(1+\Delta/\alpha)} \\
n_{crit} &= \frac{1}{2j+1}\left(\frac{|\Delta+j\alpha|^2}{4g^2} - j\right), \quad j = 0, 1, ...
\end{aligned} \tag{2.35}$$

with the transmon inharmonicity $\alpha \approx -E_c/\hbar$, we note that the readout resonator experiences a Lamb shift $\Lambda = g^2/(\Delta+\alpha)$, which is termed punch-out, as will be discussed in the measurement section.

2.1.7 Defect two level systems (TLSs)

Tunneling two-level systems (TLS) are commonly understood to be defects consisting of a single atom or a group of atoms that can tunnel between two sites within disordered or amorphous solids. TLSs are present on interfaces, surfaces, or within bulk dielectrics such as deposited films or substrates, and are known to contain both elastic and electric dipole moments and a broad spectrum of tunneling states, as illustrated in Fig. 2.5(a). As a result, they are unavoidable and commonly coupled parasitically to superconducting qubits causing coherence degradation in the qubit's relaxation (T_1) and dephasing (T_2) time. The origin of tunneling two-level systems (TLS) remains elusive, and various proposals have been put forth to explain their microscopic nature. Proposed explanations for TLS formation include atom tunneling, electrons-electron tunneling, spins, and magnetic impurities [16].

Irrespective of their microscopic origin, the standard tunneling model (STM) describes the universal behavior of TLS as a particle that can exist in one of two energetically similar configurations, as shown in Fig.2.5(b). These configurations are modeled as two minima in an asymmetric double-well potential which is separated by a barrier. The energy asymmetry of the double well potential is labeled ϵ and may be due to the width or shape of the wells. At sufficiently low temperatures, thermal activation over the barrier is suppressed and the dynamics are governed by quantum tunneling through the barrier at a rate of Δ_0. The effective Hamiltonian takes the form

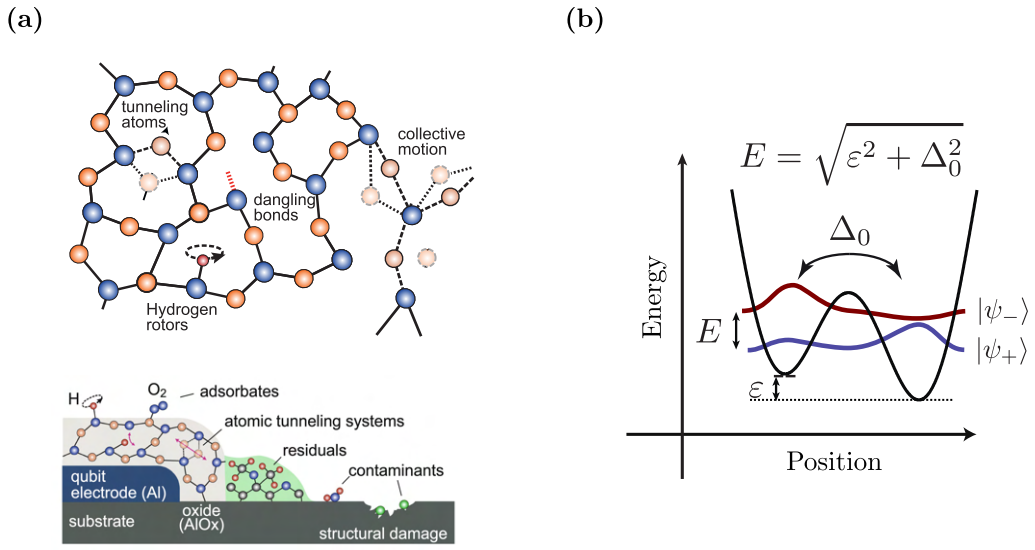

Figure 2.5: Two-level systems: (a) TLS microscopic origin, and (b) the standard tunneling model (STM) adapted from[16].

$$H_{TLS} = \frac{1}{2}\begin{pmatrix} \epsilon & \Delta_0 \\ \Delta_0 & -\epsilon \end{pmatrix} = \frac{1}{2}\epsilon\sigma_z + \frac{1}{2}\Delta_0\sigma_x \tag{2.36}$$

with the Pauli matrices in the position basis $\sigma_z^{(p)} = |R\rangle\langle R| - |L\rangle\langle L|$ and $\sigma_x^{(p)} = |R\rangle\langle L| + |L\rangle\langle R|$. Diagonalizing the Hamiltonian gives

$$\begin{aligned} H_{TLS} &= \frac{1}{2}E\sigma_z \\ E &= \sqrt{\epsilon^2 + \Delta_0^2} \end{aligned} \tag{2.37}$$

where the eigenstates are

$$\begin{aligned} |\psi_+\rangle &= \sin(\theta/2)\,|L\rangle + \cos(\theta/2)\,|R\rangle \\ |\psi_-\rangle &= \cos(\theta/2)\,|L\rangle - \sin(\theta/2)\,|R\rangle \end{aligned} \tag{2.38}$$

Using Wentzel–Kramers–Brillouin (WKB) theory, we can estimate the value of Δ_0 in terms of the barrier height V, wells spacing d, and the effective mass m

$$\begin{aligned} \Delta_0 &= \hbar\omega_0 e^{-\lambda} \\ \lambda &= \sqrt{\frac{2mV}{\hbar^2}}d \end{aligned} \tag{2.39}$$

Due to the randomized nature of TLS, the STM assumes a uniform distribution of ϵ and λ, which can also be expressed in term in term of the energy E and tunneling rate Δ_0

$$\begin{aligned} P(\epsilon,\lambda)d\epsilon d\lambda &= P_0 d\epsilon d\lambda \\ P(E,\Delta_0)dE d\Delta_0 &= P_0 \frac{E}{\Delta_0\sqrt{E^2-\Delta_0^2}} d\Delta_0 dE \end{aligned} \tag{2.40}$$

We can then calculate the density of state ρ_{TLS} by integrating the probability distribution over all Δ_0

$$\rho_{TLS}(E) = \int_{\Delta_0^{min}}^{E} P(E,\Delta_0)d\Delta_0 = P_0 \ln \frac{2E}{\Delta_0^{min}} \approx D_0 \tag{2.41}$$

Which is approximatly constant over the energy range of interest.

TLS almost always shows dissipative dynamics, and the principal origin of dissipation and decoherence in two-level systems (TLS) can be attributed to their interaction with phonon modes within their host material. This is primarily due to the susceptibility of the asymmetry energy ϵ to lattice strains, which induces a dissipation channel between the TLS and the phonon modes allowed in the system.

$$\epsilon = 2\gamma \cdot \mathbf{S} + 2\mathbf{p}.\mathbf{E} + \epsilon_0 \tag{2.42}$$

with tensor γ defining the TLS coupling strength to the strain field $\mathbf{S}$, and the dipole moment $\mathbf{p}$ defining the coupling strength to the electric field $\mathbf{E}$. Typical values are $|\gamma| \approx 1\,\text{eV}$ and $p \approx 0.3\,\text{eÅ}$. Therefore, TLS can be thought of as a tiny piezoelectric transducer residing on the qubit surface, absorbing electric field energy from the qubit and dissipating it to the environment via phonon emission.

2.2 Open quantum systems

The quantum systems discussed thus far were isolated (transmon, resonator, capacitive coupling), permitting unitary evolution of the state vectors (Hermitian Hamiltonian) and preserving the canonical structures of the system (commutation relations). In practice, quantum systems are coupled to their environment, either intentionally for control and readout or unintentionally to a large number of degrees of freedom (e.g. TLS ensemble) that cause dissipation. In this section, we will visit briefly some of the mathematical frameworks that help model open-quantum systems in a tractable way, as the full system-bath Hamiltonian features a continuum of modes that is very difficult to simulate.

First, we present the Lindblad-form Markovian master equation, which is a set of differential equations that describes the time evolution of the density matrix of the system of interest in a bosonic bath containing an infinite number of degrees of freedom (DOF). Despite the large number of DOF, the Master's equation is typically left with a few numerically tractable variables under certain environment assumptions. Next, we present the input-output formalism which can be thought of as the Heisenberg picture analog of the Master's equation

(Schrödinger picture). We can then use the developed input-output theory to derive Purcell decay, which describes how one system will decay through coupling to another dissipative system; the Fermi-Golden rule, which describes the dissipation when coupled to a continuum of non-dissipative states; and the coherent exchange between two dissipative systems.

All the mentioned treatments up to this point assume a Markovian (memoryless) environment that has no backaction on the system of interest. Non-Markovian dynamics are more complex to treat and are active subjects of research, both theoretically and experimentally. In the last section, we briefly review a recent development that derives and applies the Solomon equations for qubits and two-level systems bath the resembles a non-Markovian environment [26].

2.2.1 Lindblad master equation

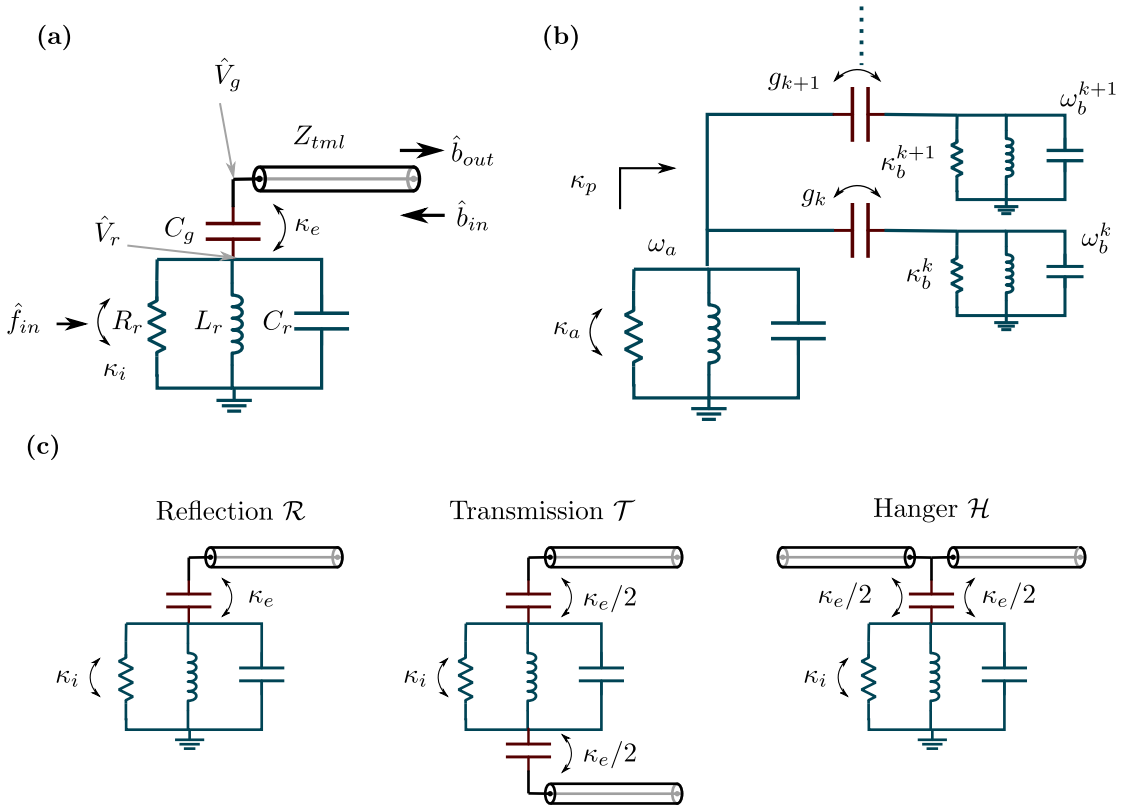

Figure 2.6: Harmonic oscillator coupled to dissipative environments: (a) infinite-length transmission line, (b) a bosonic bath of damped resonators, and (c) coupling configurations.

An ohmic resistor in cQED can be modeled by a transmission line resonator with a

length that extends to infinity, as depicted by Fig. 2.6(a). This will lead to densely packed normal modes with $\omega = ck$ dispersion relation, and thus must be treated in the continuum limit. The derivation follows the standard quantization procedure to that of an LC resonator except for the presence of an infinite number of resonances. The derivation is omitted for the virtue of brevity and can be found in [27]. In summary, we obtain the Lagrangian from the telegraph equations, extract the Hamiltonian through Legendre transformation, and calculate the Heisenberg equations of motion which will result in massless-like Klein-Gordon equation, the solutions of which are the operators for each normal mode hosted by transmission line that are finally substituted back in the Hamiltonian to have:

$$\hat{H}_{tml} = \int_0^\infty d\omega \hbar\omega \hat{b}_\omega^\dagger \hat{b}_\omega \tag{2.43}$$

where $\hat{b}_\omega^\dagger, \hat{b}_\omega$ are the creation an annihilation operators of mode ω and they obey the bosonic commutation relations $[\hat{b}_\omega \hat{b}_{\bar{\omega}}^\dagger] = \delta(\omega - \bar{\omega})$, and $[\hat{b}_\omega \hat{b}_{\bar{\omega}}] = [\hat{b}_\omega^\dagger \hat{b}_{\bar{\omega}}^\dagger] = 0$. The position-dependent charge and flux operators are given by

$$\begin{aligned} \hat{\Phi}_{tml}(x) &= \int_0^\infty d\omega \sqrt{\frac{\hbar}{\pi\omega c v}} \cos\Big(\frac{\omega x}{v}\Big)(\hat{b}_\omega^\dagger + \hat{b}_\omega) \\ \hat{Q}_{tml}(x) &= i\int_0^\infty d\omega \sqrt{\frac{\hbar\omega c}{\pi v}} \cos\Big(\frac{\omega x}{v}\Big)(\hat{b}_\omega^\dagger - \hat{b}_\omega) \end{aligned} \tag{2.44}$$

with the speed of wave in the transmission line $v = 1/\sqrt{lc}$ where l and c is the inductance and capacitance per unity length, respectively. The above operators can be understood as the charge/flux at one point on the transmission line (delta function) which is the sum of all the harmonic modes (Fourier transform on operators).

Now, let us assume that an LC resonator is capacitively coupled to the above infinite transmission line at $x = 0$ and $R_r = 0$. The Hamiltonian of the system can be obtained by substituting Eq. 2.21(a) and (d) in Eq. 2.18 , applying the RWA, and assuming high-Q LC resonator that responds only to a small bandwidth around $\omega_r = 1/\sqrt{L_r C_r}$, and thus $g(\omega) \approx g(\omega_r)$, we have

$$\hat{H} = \hat{H}_{LC} + \hat{H}_{tml} - \hbar g(\omega_r) \int_0^\infty d\omega (\hat{a}\hat{b}_\omega^\dagger + \hat{a}^\dagger \hat{b}_\omega) \tag{2.45}$$

with

$$g(\omega_r) = \frac{C_g}{cC_r}\sqrt{\frac{1}{2Z_r}}\sqrt{\frac{\omega_r c}{\pi v}} = \frac{C_g}{\sqrt{C_r}}\sqrt{\frac{Z_{tml}\omega_r^2}{2\pi}} \tag{2.46}$$

The above equation means that the interaction is dissipative (coupling to a bosonic bath) and the photon decay rate (resonator linewidth) is

$$\kappa_e = 2\pi g(\omega_r)^2 = \frac{Z_{tml}\omega_r^2 C_g^2}{C_r} \tag{2.47}$$

which can also be found classically using Eq. 2.23 and assuming a small coupling capacitance C_g:

$$\kappa_e = \frac{Re[Y(\omega_r)]}{C_r} \approx \frac{Z_{tml}\omega_r^2 C_g^2}{C_r} \tag{2.48}$$

Now, under the well-established Born-Markov approximation, the density matrix of the system evolves as

$$\dot{\rho} = -i\Big[\hat{H}_{LC}, \rho\Big] + \underbrace{\kappa(\bar{n}_k + 1)\mathcal{D}[\hat{a}]\rho}_{\text{photon loss}} + \underbrace{\kappa\bar{n}_k\mathcal{D}[\hat{a}^\dagger]\rho}_{\text{photon absorption}} \tag{2.49}$$

where $\bar{n}_k$ is the number of thermal photons in the transmission line and the dissipator is defined as

$$\mathcal{D}[\hat{O}]\bullet = \hat{O}\bullet\hat{O}^\dagger - \frac{1}{2}\{\hat{O}^\dagger\hat{O}, \bullet\} \tag{2.50}$$

with $\{.,.\}$ being the anticommutator. The last term corresponds to photon absorption from the bath which is typically negligible as $\bar{n}_k \to 0$ at low temperatures. Eq. 2.49 can be easily adapted to the transmon or TLS by simply replacing the $\hat{a}/\hat{a}^\dagger$ with $\hat{\sigma}_-/\hat{\sigma}_+^\dagger$. Assuming the qubit is cold enough $\bar{n}_k = 0$ and adding a phenomenological model that accounts for dephasing, we have

$$\dot{\rho} = -i\Big[\hat{H}_T, \rho\Big] + \underbrace{\gamma\mathcal{D}[\hat{\sigma}_-]\rho}_{\text{Depolarization}} + \underbrace{2\gamma_\phi\mathcal{D}[\hat{\sigma}_-^\dagger\hat{\sigma}_+]\rho}_{\text{Dephasing}} \tag{2.51}$$

From here, we can define two important characteristic times of decoherence

$$\begin{aligned} T_1 &= \frac{1}{\Gamma_1} \\ T_2 &= \frac{1}{\Gamma_2} = (\frac{\Gamma_1}{2} + \Gamma_\phi)^{-1} \end{aligned} \tag{2.52}$$

The T_1 time is the characteristic lifetime for the qubit to relax from the $|e\rangle$ to $|g\rangle$ state as it exchanges energy with the environment. The T_2 time is the characteristic lifetime of the coherent superposition, which has a contribution from both the pure dephasing Γ_ϕ and depolarization Γ_1. The factor of 2 comes from the fact that T_1 is a timescale for probability decay whereas phase coherence is a measure of amplitude. Dephasing occurs when the frequency of the qubit is unstable, scrambling the phase evolution of the superposition state. This can be visualized on the Bloch sphere, where a detuning of the qubit from the rotating frame would precess the state vector around the Z-axis, scrambling the phase.

There are subtle distinctions between the depolarization Γ_1 and dephasing Γ_ϕ. Depolarization Γ_1 captures longitudinal relaxations of the qubit, it involves energy exchange (inelastic), is a resonant phenomenon (small bandwidth), is caused by transverse noise (capacitive), and is fundamentally irreversible. On the other hand, Γ_ϕ capture transversal relaxations, it doesn't involve energy exchange (elastic), is not a resonant phenomenon (wide bandwidth), is caused by longitudinal noise (inductive), and can in principle be reversed.

2.2.2 Input-output theory

The input-output theory is formulated on the level of the Heisenberg equation of motions to describe the time evolution of the field amplitudes $\hat{a}(t)$ inside a cavity and its relation with scattered fields $\hat{b}_{in}$, $\hat{b}_{out}$ or external quantum noise $\hat{f}_{in}$. Let's assume the transmission line in Fig. 2.6(a) is impedance matched to Z_{tml}. We are interested in deriving an expression of the cavity field amplitude $\hat{a}$ around ω_r. First, we apply Kirchhoff's current law on the resonator node

$$\begin{aligned} \hat{I}_{out} - \hat{I}_{in} &= \hat{I}_g \\ \frac{\hat{V}_{out} - \hat{V}_{in}}{Z_{tml}} &= \frac{\hat{V}_r - \hat{V}_g}{1/i\omega_r C_g} \\ \frac{\hat{V}_{out} - \hat{V}_{in}}{Z_{tml}} &= \frac{C_g}{C_r}\hat{I}_r \end{aligned} \tag{2.53}$$

where in the last expression, we have used $\hat{V}_g = 0$ (resonance/weak damping) and $\hat{V}_r = \hat{I}_r/i\omega_r C_r$. Noting that $\hat{V} = \dot{\hat{\Phi}}$ and $\hat{I} = \dot{\hat{Q}}$, we substitute the transmission line flux operator (Eq. 2.44) in the LHS and the resonator charge operator (Eq. 2.2) on the RHS. With some arrangements, we can show

$$\boxed{\hat{b}_{out}(t) - \hat{b}_{in}(t) = \sqrt{\kappa_e}\hat{a}(t)} \tag{2.54}$$

where κ_e is given by Eq. 2.48 and the square root emphasizes that we are dealing with amplitudes. The input/output fields are defined as:

$$\hat{b}_{out/in}(t) = \frac{i}{\sqrt{2\pi}}\int_{-\infty}^{\infty} d\omega(\hat{b}_{\omega}^{\dagger(out/in)} + \hat{b}_{\omega}^{(out/in)}) \tag{2.55}$$

Now, by the superposition theorem from classical circuit analysis, let us turn off all the external sources. The circuit can then be simplified to a simple parallel RLC circuit with a total decay rate of $\kappa = 1/RC$. Keeping this thought in mind, we concede by applying Kirchhoff's law on the parallel RLC resonator

$$\begin{aligned} \hat{I}_C + \hat{I}_L + \hat{I}_R &= 0 \\ \ddot{\hat{Q}} + \frac{\dot{\hat{Q}}}{RC} + \frac{\hat{Q}}{LC} &= 0 \end{aligned} \tag{2.56}$$

where in the second line, we wrote all the variables in terms of the charge operator $\hat{Q}$. If we neglect the fast rotating frame by writing

$$\begin{aligned} \hat{Q} &= Q_{zpf}\hat{a}e^{-i\omega_r t} \\ \dot{\hat{Q}} &\approx Q_{zpf}(-i\omega_r\hat{a})e^{-i\omega_r t} \\ \ddot{\hat{Q}} &\approx Q_{zpf}(-\omega^2\hat{a} - 2i\omega_r\dot{\hat{a}})e^{-i\omega_r t} \end{aligned} \tag{2.57}$$

and substituting back in Eq. 2.56, we have

$$\dot{\hat{a}} = -\frac{\kappa}{2}\hat{a} + i\Delta\hat{a} \tag{2.58}$$

with the detuning $\Delta = \omega - \omega_r$. The factor of 2 in κ emphasizes an amplitude decay $\exp\{\kappa\hat{a}(t)/2\} = \sqrt{\exp\{\kappa\hat{a}(t)\}}$.

Now turning on the external sources, It is easy to see now the new input-output relation is

$$\boxed{\dot{\hat{a}} = -\frac{\kappa}{2}\hat{a} + i\Delta\hat{a} + \sqrt{\kappa_e}\hat{b}_{in} + \sqrt{\kappa_i}\hat{f}_{in}} \tag{2.59}$$

with the input fields $\hat{b}_{in}$ $\hat{f}_{in}$ are added using Eq. 2.54 where as the damping $\kappa = \kappa_e + \kappa_i$, with κ_e given by Eq. 2.48 and $\kappa_i = 1/R_rC_r$. The input field $\hat{a}_{in}$ is a stochastic quantum field that represents vacuum fluctuations and resistance noise.

Relating to the classical world, we take the expectation value $\hat{a} \to \langle\hat{a}\rangle$. It is straightforward to see that under steady-state input field and assuming $\hat{f}_{in} = 0$

$$\langle\hat{a}\rangle = \frac{\sqrt{\kappa_e}\,\langle\hat{a}_{in}\rangle}{\kappa/2 - i\Delta} \tag{2.60}$$

The input power is $P_{in} = \hbar\omega\,\langle\hat{a}_{in}\hat{a}_{in}\rangle$ and the number of photons circulating the cavity is

$$\bar{n}_{cav} = \frac{\kappa_e}{\Delta^2 + (\kappa/2)^2}\frac{P}{\hbar\omega} \tag{2.61}$$

whereas the transmission scattering parameter takes a Lorentzian lineshape

$$\boxed{\mathcal{R} = \frac{\langle\hat{a}_{out}\rangle}{\langle\hat{a}_{in}\rangle} = \frac{(\kappa_i - \kappa_e)/2 - i\Delta}{(\kappa_i + \kappa_e)/2 - i\Delta}} \tag{2.62}$$

The derivation above of the scattering parameter is for a resonator in the reflection configuration $\mathcal{R}$. We can derive other common coupling configurations, illustrated in Fig. 2.6(c), such as the transmission configuration $\mathcal{T}$ and hanger configuration $\mathcal{H}$, by simply noting that

$$\boxed{\mathcal{T} = \frac{1 - \mathcal{R}}{2} = \frac{\kappa_e/2 - i\Delta}{(\kappa_i + \kappa_e)/2 - i\Delta}} \tag{2.63}$$

$$\boxed{\mathcal{H} = \frac{1 + \mathcal{R}}{2} = \frac{\kappa_i/2 - i\Delta}{(\kappa_i + \kappa_e)/2 - i\Delta}} \tag{2.64}$$

2.2.3 Purcell effect, Fermi's golden rule, and coherent exchange

The Purcell effect is a phenomenon named after the physicist Edward Purcell, which describes the enhancement or suppression of the spontaneous emission rate of an atom once placed in a

cavity. A closely related concept is Fermi's Golden Rule, developed by Enrico Fermi and Paul Dirac, which describes the spontaneous emission rate of an atom due to the coupling to a continuum of states. In this section, we will derive the two phenomena from the input/output formalism we have developed in the previous section. Additionally, we will show that under certain conditions, a coherent exchange of energy can occur between the subsystems.

Let us consider resonator A to be capacitively coupled to a bath of resonators B_k, resembling the environment, as illustrated in Fig. 2.6(b). From here on, we will dismiss quantum fluctuations and use the expectation value notation $\langle \hat{a} \rangle \rightarrow a$. Taking the expectation value of Eq. 2.59 and noting that $\left\langle \hat{f}_{\text{in}} \right\rangle = 0$, we have:

$$\begin{aligned} \dot{a} &= -\frac{\kappa_a}{2} \langle a \rangle + i \sum_k g_k b_k \\ \dot{b}_k &= -\frac{\kappa_b^k}{2} b_k + i\Delta_k b_k + i g_k a \end{aligned} \tag{2.65}$$

with $\Delta_k = \omega_a - \omega_b^k$. The objective of this section is to evaluate the cross relaxation rate of resonator A due to the resonator bath B.

The Purcell decay

Under the condition of an overdamped environment ($\kappa_{b,k} \gg \kappa_a, g_k$), we can apply the adiabatic elimination technique and set $\dot{b} \approx 0$. From the second part of Eq. 2.65 we have

$$b_k = \frac{i g_k}{\kappa_b^k/2 - i\Delta_k} a \tag{2.66}$$

substituting it back in the first part of Eq. 2.65, we obtain

$$\dot{a} = -(\frac{\kappa_a}{2} + \sum_k \underbrace{\frac{\kappa_b^k}{2} \frac{g_k^2}{(\kappa_b^k/2)^2 + \Delta_k^2}}_{\text{Purcell}})a + i \sum_k \frac{g_k^2 \Delta_k}{(\kappa_b^k/2)^2 + \Delta_k^2} a \tag{2.67}$$

The first term expresses the decay experienced by resonator A, which includes two parts: the internal decay κ_a, and the Purcell decay due to the coupled resonators B_k with a Lorentzian line shape:

$$\boxed{\kappa_p = \sum_k \frac{g_k^2}{(\kappa_b^k/2)^2 + \Delta_k^2} \kappa_b^k} \tag{2.68}$$

We note that at far detuning ($\Delta_k \gg \kappa_b^k$), the decay rate is $\kappa_p \approx (g_k/\Delta_k)^2 \kappa_b^k$ which is proportional to the loss rate κ_b^k. On the other hand, around resonance ($\Delta \approx 0$), the decay rate is $\kappa_p =\approx 4g_k^2/\kappa_b^k$ which is inversely proportional to κ_b^k. This can be understood as suppressing the decay in the latter enhances the DOS locally which promotes energy exchange and therefore dissipation of resonator A.

Fermi's golden rule

Assuming resonator A is in the excited state and resonators B_k are in their ground state, we proceed by integrating the second part of Eq. 2.65:

$$b_k(t) = ig_k \int_0^t a(t')e^{-i(\Delta_k - i\kappa_b^k/2)(t'-t)}dt' \tag{2.69}$$

substituting it back in the first part, gives

$$\dot{a} = -\frac{\kappa_a}{2}a - \sum_k |g_k|^2 \int_0^t a(t')e^{-i(\Delta_k - i\kappa_b^k/2)(t'-t)}dt' \tag{2.70}$$

In the long time limit, the integrand above is only appreciable when $t = t'$. We can therefore assume $a(t') = a(t)$ and take it outside the integral, and also approximate the exponent to a unity. This will yield

$$\int_0^t e^{-i(\Delta_k - i\kappa_b^k/2)(t'-t)}dt' = \frac{i(1 - e^{i(\Delta_k - i\kappa_b^k/2)t})}{\Delta_k - i\kappa_b^k/2} \approx \frac{i}{\Delta_k - i\kappa_b^k/2} \tag{2.71}$$

If we take the limit as $\kappa_b^k \to 0$ and using Sokhotski–Plemelj theorem in complex analysis, we have

$$\lim_{\kappa_e \to 0} \frac{i}{\Delta_k - i\kappa_b^k/2} = \pi\delta(\Delta_k) + i\mathcal{P}\frac{1}{\Delta_k} \tag{2.72}$$

substituting it back in the first part, gives

$$\dot{a} = -a \underbrace{(\pi \sum_k |g_k|^2 \delta(\Delta_k))}_{\kappa_f/2} - i \underbrace{\sum_k |g_k|^2 \mathcal{P}\frac{1}{\Delta_k}}_{\Delta_{Stark}} \tag{2.73}$$

Where the decay-rate part is the well know Fermi-Golden rule

$$\boxed{\kappa_f = 2\pi \sum_k |g_k|^2 \delta(\Delta_k)} \tag{2.74}$$

It is worth noting that in the Purcell derivation, we assumed the environment to be overdamped ($\kappa_b^k \gg \kappa_a, g$). On the other hand, in the Fermi derivation, we assumed $a(t') = a(t)$. Both assumptions ensure that there is no bath backaction on the resonator A and no interactions occurring in between resonators B_k. In other words, resonator A is examined on timescales much shorter than the timescale over which the environment changes or, equivalently, when the environment is overdamped and doesn't change on an even longer timescale.

Coherent exchange

If we consider a single strongly coupled resonator in the environment ($g_1 \gg \kappa_a + \kappa_b$) that is in resonance with A ($\Delta = 0$), we can find from Eq. 2.65 that

$$\ddot{a} + \frac{\kappa_a + \kappa_b}{2}\dot{a} - g^2 a = 0 \tag{2.75}$$

which represents a hybridized state with a decay rate equal to the sum of the two individual coupled resonators ($\kappa_a + \kappa_b$) and an exchange frequency of $2g$. The field amplitude of resonator A takes the following form

$$\boxed{a = e^{-\kappa_s/2t}\cos(2gt)} \tag{2.76}$$

with $\kappa_s = (\kappa_a + \kappa_b)$. As will be seen later, this feature can be used to probe and study strongly coupled individual TLS using a tunable probe qubit.

Qubit-TLS interaction

TLS are atomic-sized electric dipoles that usually couple capacitively to the qubit. In the single-excitation limit, both the qubit and TLS can be treated as linear resonators, and their dynamics follow Eq. 2.65. Let us consider a qubit with a lifetime of 10 µs interacting with a single TLS. The typical lifetime of TLS is around 100 ns and can reach up to 1 ms if the phonon decay is suppressed using a phononic crystal (as will be shown later). Assuming a TLS resides at the edge of a closely spaced capacitor electrode where the electric field is

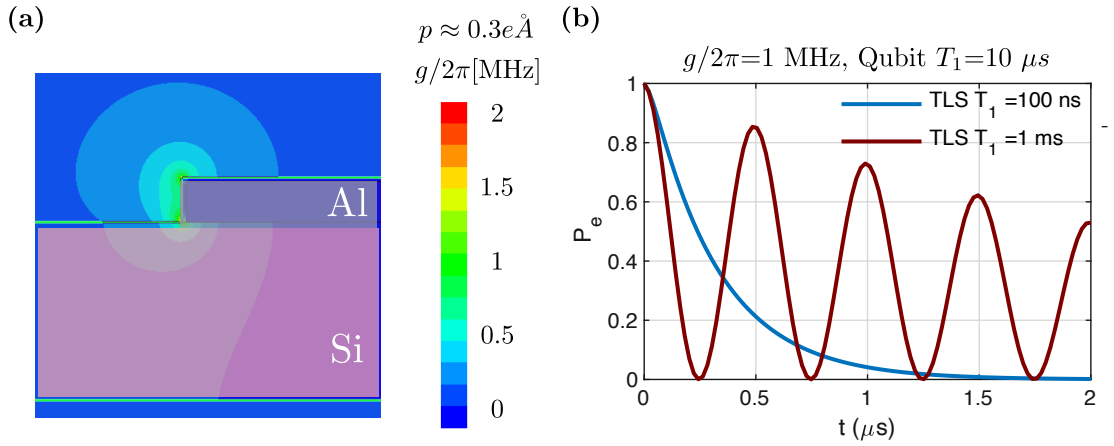

Figure 2.7: Qubit-TLS interaction: (a) coupling strength g through electrostatic simulation of closely spaced capacitor electrodes, and (b) qubit population dynamics that is on resonance with a TLS with a lifetime of 100 ns and 1 ms.

maximum, the coupling strength can be simulated by noting that $g = \mathbf{p}.\mathbf{E}/\hbar$ where $\mathbf{p}$ is the electric dipole moment of the TLS and is around $0.2\,\mathrm{e\AA}$. The simulation results are shown in Fig. 2.7(a), giving an average coupling strength of $g/2\pi = 1\,\mathrm{MHz}$.

Using this information, we can solve for the qubit decay rate as it interacts with the decaying TLS by solving the coupled differential equation numerically (Eq. 2.65). When the TLS is overdamped with respect to the coupling strength g and the qubit lifetime, the qubit experiences an exponential Purcell decay as in Eq. 2.68. On the other hand, coherent Qubit-TLS interaction occurs when the coupling strength exceeds the relaxation rates of both the TLS and Qubit, resulting in oscillatory exchange of population at a frequency of $2g$, as illustrated in Fig. 2.7(b) and as given by Eq. 2.76.

2.2.4 Solomon equations

When the qubit is coherently coupled to an ensemble of TLSs, and the dynamics involve multiple excitations, the physics encompasses highly correlated many-body states that are complex to compute and analyze. In fact, it is the intractable simulation of these many-body states that makes building quantum computers appealing in the first place. Fortunately, with increasing decoherence in the system, one can expect a transition from coherent oscillations to a regime where the qubit populations follow a simple rate equation, similar in structure to the Solomon equations used to describe the dipolar relaxation of spin systems [28]. In this section, we briefly review the key formulas used in this work where the detailed derivations can be found in Ref [26].

The system is modeled assuming the qubit with population p_q is coupled to a countable number of TLSs with populations p_t^k. We denote Γ_q and Γ_t^k as the intrinsic relaxation rates of the qubit and the kth TLS, respectively. A general form of the Purcell decay rate Γ_{qt}^k can be derived from the Bloch-Redfield master equation and is given by

$$\Gamma_{qt}^k = \frac{2g_k^2\Gamma_m}{\Gamma_m^2 + \Delta_k^2}, \tag{2.77}$$

where Δ_k is the detuning between the qubit and the kth TLS, g_k represents their transverse coupling strength, and the mutual decoherence is described by $\Gamma_m = (\Gamma_q + \Gamma_t^k)/2$ in the absence of dephasing. We note that this is a more general form of Purcell decay than what was derived previously and Eq. 2.68 can be obtained by assuming that the TLS has a much larger decay rate than the qubit such that $\Gamma_m \approx \Gamma_t^k/2$. In the limit where the mutual decoherence of the qubit and TLS is sufficiently strong ($\Gamma_m > g_k$), the interaction is incoherent, and the population dynamics are governed by the Solomon rate equations:

$$\dot{p}_q = -\Gamma_q(p_q - p_{th}) - \sum_k \Gamma_{qt}^k(p_q - p_t^k) \tag{2.78}$$

$$\dot{p}_t^k = -\Gamma_t(p_t^k - p_{th}) - \Gamma_{qt}^k(p_t^k - p_q) \tag{2.79}$$

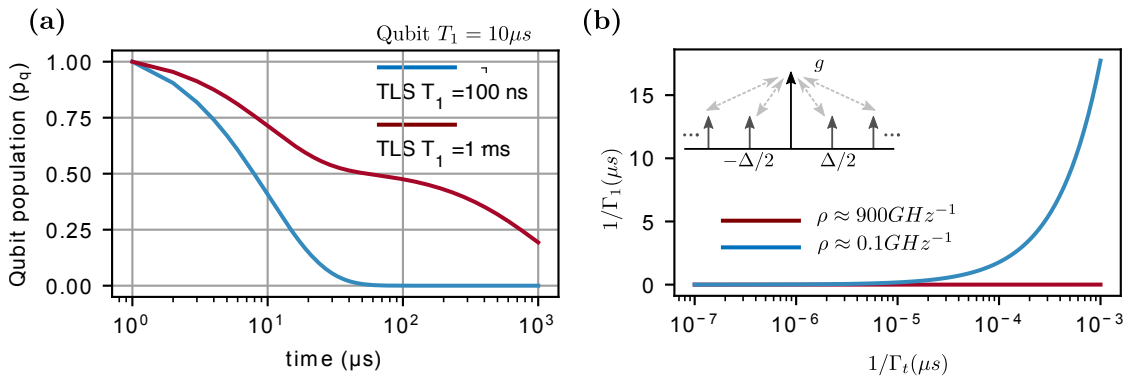

Figure 2.8: Qubit-TLS ensemble interaction: (a) biexponential qubit decay for different TLS lifetimes, and (b) qubit versus TLS lifetime for uniformly distributed TLSs.

From the initial conditions, one can determine the upward and downward transition rates of the qubit

$$\Gamma_\uparrow(t) = \dot{p}_q(t)|_{p_q=0} \text{ and } \Gamma_\downarrow(t) = -\dot{p}_q(t)|_{p_q=1}, \tag{2.80}$$

from which, the qubit decay rate and its equilibrium population can be determined

$$\Gamma_1 = \Gamma_\uparrow(t) + \Gamma_\downarrow(t) = \Gamma_q + \sum_k \Gamma_{qt}^k \tag{2.81}$$

$$p_{eq}(t) = \frac{\Gamma_\uparrow(t)}{\Gamma_1} = \frac{\Gamma_q p_{th} + \sum_k \Gamma_{qt}^k p_t^k(t)}{\Gamma_1}. \tag{2.82}$$

In the special case of identical Purcell decay rates ($\Gamma_{qt}^k = \Gamma_{qt}$) with a large number of TLSs, the TLSs evolve independently of the qubit with $p_t^*(t) \approx p_{t,0}^* e^{-\Gamma_t t}$. By substituting the assumptions into Eq. 2.78, the qubit population obeys then the following differential equation

$$\dot{p}_q = -\Gamma_1(p_q - p_{th}) + \Gamma_q^{TLS} p_{t,0}^* e^{-\Gamma_t t}, \tag{2.83}$$

where $\Gamma_q^{TLS} = \sum_k \Gamma_{qt}^k$ is the sum of the Purcell decay rates. It can be shown that in the case of long-lived TLSs ($\Gamma_t \ll \Gamma_1$), an approximate solution to the above differential equation is a biexponential with fast and slow decay parts that encode the qubit and TLS relaxation rates, respectively. The slowly varying amplitude of population decay for the TLSs can be obtained by setting $\dot{p}_q = 0$ (adiabatic elimination), from which the approximate solution to Eq. 2.83 can be obtained:

$$\boxed{p_q(t) \approx p_{q,0}^* e^{-\Gamma_1 t} + \frac{\Gamma_q^{TLS}}{\Gamma_1} p_{t,0}^* e^{-\Gamma_t t} + p_{th}} \tag{2.84}$$

We can see from Fig. 2.8(a) that the decay dynamics for a qubit with a lifetime of 10 µs, coupled to a short-lived TLS bath ($1/\Gamma_t = 100$ ns), is predominantly single exponential decay,

resembling a typical Markovian environment. In contrast, when it's coupled to a long-lived TLS bath ($1/\Gamma_t = 1\,\text{ms}$), the decay is biexponential, indicating a strong non-Markovian bath dynamics.

2.2.5 Purcell decay rate of uniformly distributed TLSs

When the TLSs are spread in frequency and equally spaced by a period Δ with a single coupling strength g and mutual decoherence rate Γ_m (see inset of Fig. 2.8(b)), an analytical expression for the Purcell decay rate can be obtained as follows:

$$\Gamma_q^{TLS} = \sum_k \frac{2g^2\Gamma_m}{\Gamma_m^2 + \Delta_k^2} \tag{2.85}$$

$$= \sum_{h=-\infty}^{\infty} \frac{ab^2}{b^2 + (h - bc)^2} \tag{2.86}$$

$$\Gamma_q^{TLS} = \pi ab \frac{\sinh(2\pi b)}{\cosh(2\pi b) - \cos(2\pi bc)} \tag{2.87}$$

where $a = 2g^2/\Gamma_m$, $b = \Gamma_m/\Delta$, $c = \Delta_0/\Gamma_m$ with Δ_0 being the shift of the periodic TLS with respect to the qubit and can take any value between $\Delta_0 \in \{0, \Delta/2\}$. In the limit of sparse TLSs ($b \to 0$), the sum can be terminated to the few nearest interacting TLSs, and the decoherence follows the Purcell formula $\Gamma_q^{TLS} \approx (g/\Delta)^2\Gamma_t$ (Eq. 2.68). In the limit of dense TLSs ($b \to \infty$), Eq. 2.87 is approximately equal to πab and $\Gamma_q^{TLS} \approx 2\pi g^2\rho$ which is the Fermi's golden rule and is independent of the TLS relaxation time (Eq. 2.74). Fig. 2.8(b) is a plot of $1/\Gamma_q^{TLS}$ as a function of $1/\Gamma_t$, where we can note a clear switch from Purcell limit to Fermi-limit as the TLS density increases.

2.3 Phononic bandgap engineering

Having established that TLSs mediate dissipation between the qubit and a phonon bath, and the qubit decay follows the Purcell formula ($\Gamma_q^{TLS} \approx (g/\Delta)^2\Gamma_t$) as long as the TLS density is kept low, one might be tempted to design a mechanical Purcell filter that suppresses TLS dissipation (Γ_t) and consequently the qubit dissipation due to TLSs (Γ_q^{TLS}). This can be achieved by reducing the phonon density of states (ρ_{ph}) using a phononic bandgap metamaterial. This is evident when reading Fermi's golden rule for the TLS-phonon bath dynamic, where $\Gamma_t \propto 2\pi g_{ph}^2\rho_{ph}$. A phononic bandgap is a range of frequencies within which elastic waves cannot propagate in a material, and the material behaves as an insulator for sound waves.

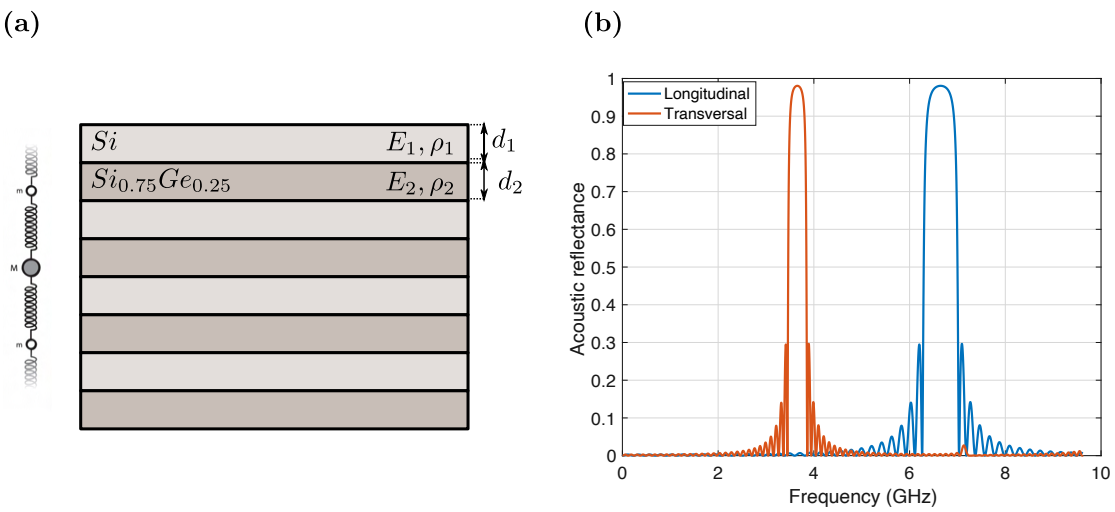

Figure 2.9: Phononic superlattice: (a) schematic of Si/SiGe phononic superlattice, and (b) reflection spectrum at normal incidence for the longitudinal and transversal acoustic modes.

2.3.1 Phononic superlattice

A stratified medium with an alternating two-material stack (e.g., Si/SiGe superlattice) supports transversal and longitudinal elastic waves and has a lumped-element representation of a spring-mass system with two alternating masses, as illustrated in Fig. 2.9(a). The one-dimensional scalar wave equation for this system is [29]:

$$\frac{\partial^2 U_i}{\partial z^2} + k_i^2 U_i^2 = 0 \tag{2.88}$$

with the dispersion relation $\kappa_i = \omega / v_i$. The scalar equation hold also true for electromagnetic waves (photonic superlattice), as well as its lumped-element representation (LC resonator). The velocities are summarized below:

$$\begin{array}{ll} \text{Elastic wave} & \text{EM wave} \\ v_i^L = \sqrt{\dfrac{\lambda_i + 2\mu_i}{\rho_i}}, v_i^T = \sqrt{\dfrac{\mu_i}{\rho_i}} & v_i = \sqrt{\dfrac{1/\bar{\mu}_i}{\epsilon_i}} \\ \text{mass spring} & \text{LC} \\ v_i = \sqrt{\dfrac{k_i'}{m_i'}} & v_i = \sqrt{\dfrac{1/L_i'}{C_i'}} \end{array} \tag{2.89}$$

where $[\lambda_i, \mu_i]$ are Lamé's first and second parameters, respectively, defining the stress-strain relation in an elastic medium; $[\epsilon_i, \bar{\mu}_i]$ are the permittivity and permeability for a propagating

electromagnetic wave; $[k_i, m_i]$ are the spring constant and mass of the spring-mass system; and $[L_i, C_i]$ are the inductor and capacitance in the LC resonator system. Unlike EM wave, both transversal and longitudinal elastic waves are supported in the superlattice and propagate with different speeds $[v_i^L, v_i^T]$. In solid mechanincs, the Lamé constants are connected with the Young's modulus E, shear modulus G, and the Poisson ratio ν by

$$\begin{aligned} \mu = G &= \frac{E}{2(1+\nu)}, \\ \lambda &= \frac{E\nu}{(1+\nu)(1-2\nu)} \end{aligned} \tag{2.90}$$

For an infinite-length 1D stack, the energy bands can be solved analytically similar to the Kronig-Penney model for an electron in a one-dimensional potential (Eigenmode formulation). Here, we proceed with a finite-length stack and follow the transfer matrix method. The transmission ($t_{i,j}$) and reflection ($r_{i,j}$) coefficients can be obtained by applying the boundary conditions at the i, j interface, obtaining

$$t_{i,j} = \frac{2Z_i}{Z_i + Z_j}, \quad r_{i,j} = \frac{Z_i - Z_j}{Z_i + Z_j}, \tag{2.91}$$

where the impedence

$$\begin{array}{ll} \text{Elastic wave} & \text{EM wave} \\ Z_i = v_i \rho_i & Z_i = v_i \mu_i \end{array} \tag{2.92}$$

The transfer matrix at the interface i, j ($\mathbf{T_{i,j}}$) and after propagating through a single layer i ($\mathbf{P_i}$) are given by

$$\mathbf{T_{i,j}} = \frac{1}{t_{i,j}} \begin{bmatrix} 1 & r_{i,j} \\ r_{i,j} & 1 \end{bmatrix}, \quad \mathbf{P_i} = \begin{bmatrix} \exp(-ik_i d_i) & 0 \\ 0 & \exp(ik_i d_i) \end{bmatrix} \tag{2.93}$$

Thus, the net propagation for a pair of layers $\mathbf{M}$ and an n-pair of layers $\mathbf{M_N}$ can be obtained as follows

$$\begin{aligned} \mathbf{M} &= \mathbf{P_1 T_{12} P_2 T_{21}} \\ \mathbf{M_N} &= \mathbf{M^{(N)}} \end{aligned} \tag{2.94}$$

Now, in order to design a frequency-bandgap where all waves are fully reflected, momentum conservation requires that

$$\begin{aligned} &k_{wave} + k_{crystal} = -k_{wave} \\ &2\pi/\lambda + 2\pi n/\Lambda = -2\pi/\lambda \\ &\Lambda = n\lambda/2 \end{aligned} \tag{2.95}$$

The period can be divided between the two slabs optimally based on their respective velocities

$$d_1 = \frac{v_1}{4f_B}, \quad d_2 = \frac{v_2}{4f_B} \tag{2.96}$$

The transfer matrix can then be solved numerically. A plot of the power reflected for 20 layers of $Si/Si_{0.75}Ge_{0.25}$ phononic superlattice is shown in Fig. 2.9(b). A few analytical approximations can be made for the reflected power

$$R = \frac{(k_2)^{2N} - (k_1)^{2N}}{(k_2)^{2N} + (k_1)^{2N}} \tag{2.97}$$

It is clear that the larger the difference between k_1 and k_2, the larger the reflection, and as $N \to \infty$, we have a complete bandgap ($R \to 1$). The bandgap width Δf_0 around the center frequency f_0 also follows the contrast $k_2 - k_1$ and is independent of N, as in:

$$\frac{\Delta f_0}{f_0} = \frac{4}{\pi} \arcsin\left(\frac{k_2 - k_1}{k_2 + k_1}\right) \tag{2.98}$$

2.3.2 2D phononic crystal

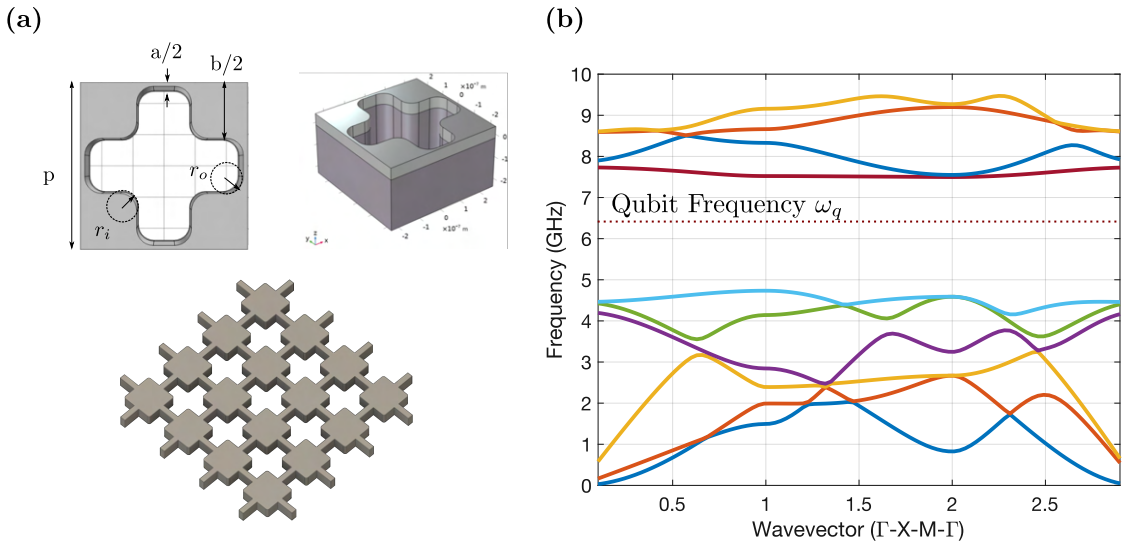

Figure 2.10: 2D phononic crystal: (a) simulated phononic bandgap unit cell with parameters $a = 70\,\text{nm}$, $b = 320\,\text{nm}$, $p = 445\,\text{nm}$, $r_i = 47\,\text{nm}$, and $r_o = 29\,\text{nm}$; and (b) the frequency band diagram of the optimized unit cell.

A complete phononic bandgap can be achieved by generalizing the phononic superlattice to two dimensions and suspending the membrane in a vacuum to eliminate out-of-plane acoustic waves. The membrane can be realized by shaping the silicon device layer of an silicon-on-insulator substrate and then releasing it, as will be discussed in section 3.1. The

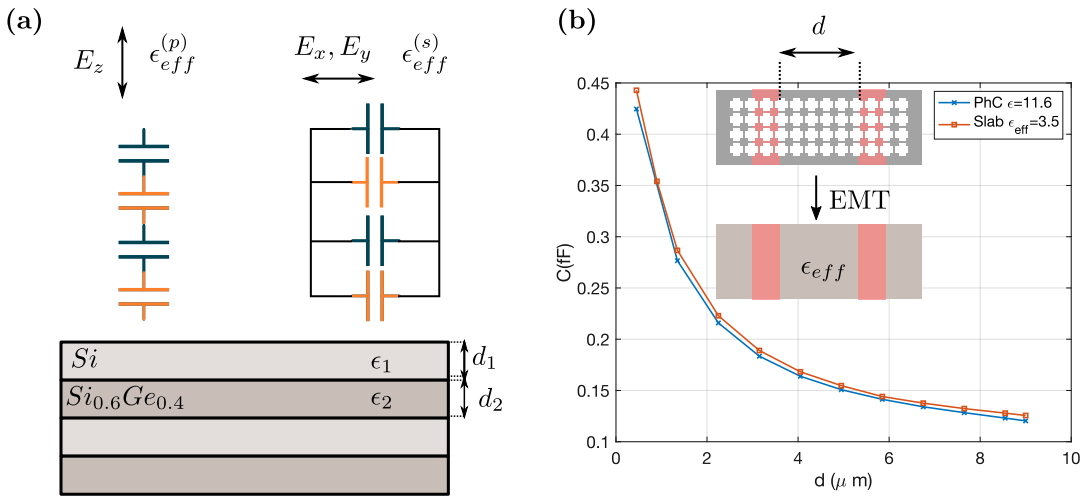

Figure 2.11: Effective medium description of: (a) 1D phononic superlattice obtained through analytical expression, and (b) 2D phononic crystal obtained through electrostatic simulation.

unit cell parameters and the periodic 2D arrangement are shown in Fig. 2.10(a). Using COMSOL Multiphysics, careful elastic simulation and optimization can yield a bandgap of 2.5 GHz centered around the qubit frequency 6.3 GHz, as shown in Fig. 2.10(b).

2.3.3 Effective medium theory

The vast scale difference between the features of the phononic crystal (∼50 nm) and the qubit capacitance used in this work (260 µm × 60 µm) posed a problem in the electrostatic simulation of the qubit parameters. This issue was addressed by resorting to the effective medium description of the phononic crystal. Effective medium theory is useful in describing phenomena on a length scale much larger than the typical scale of inhomogeneity [30]. The problem can be cast as follows: What is the permittivity of a homogeneous slab that will store the same amount of energy as the actual subwavelength phononic crystal?

$$\epsilon_{eff} E_0^2 = \frac{1}{V} \int \epsilon(\vec{r}) E^2(\vec{r}) dV \tag{2.99}$$

where the average field is

$$E_0 = \frac{1}{V} \int E(\vec{r}) dV \tag{2.100}$$

For the case of a 1D phononic superlattice, the analytical expressions of effective permittivity can be simply obtained by looking at the equivalent lumped-capacitance representation for

perpendicular and parallel electric fields, as shown in Fig. 2.11(a), and are given by

$$\begin{aligned} \frac{1}{\epsilon_{eff}^{(s)}} &= \frac{d_1}{\epsilon_1} + \frac{d_2}{\epsilon_2} \\ \epsilon_{eff}^{(p)} &= d_1\epsilon_1 + d_2\epsilon_2 \end{aligned} \tag{2.101}$$

For the 2D phononic crystal case where the electrical field is predominantly planar, we find through electrostatic simulation that an effective permittivity, $\epsilon_{eff} = 3.5$ of a homogeneous slab between two metal electrodes separated by a spacing d, yields the same capacitance as that of the original phononic crystal substrate, as illustrated in Fig. 2.11(b). The results are in good agreement with both the experimental data and the interdigitated capacitor simulation under periodic boundary conditions.

2.4 Qubit design parameters and simulation

In table 2.1, we list the design parameters of the qubit-resonator system along with the main results of the simulated composite system using the SCQubit package [31]. The design requirements are as follows:

- A qubit with a flux-insensitive point located at the center of the phononic bandgap (6.3 GHz) and a tunability range that crosses the band edge (5 GHz).
- Operating in the transmon regime ($E_j \gg E_c$) across the frequency range of the study (4.5–6.3 GHz).
- Sufficient inharmonicity to support fast 100 ns single-qubit gates.
- The qubit relaxation time ($T_1 \approx 1\,\mu s$) should not be limited by the Purcell decay through the readout resonator or the XY control line ($T_1 \ll T_1^{RO}, T_1^{XY}$).
- A fast readout measurement pulse ($1/\kappa_e < 0.5\,\mu s$) combined with a strong dispersive shift ($\chi > \kappa_e/2$).
- SQUID mutual inductance (M) balancing Z-line critical current and qubit dephasing.

Readout resonator		
Frequency	ω_r	7.1 GHz
Decay rate	$\kappa_e/2\pi$	1 MHz
Loaded quality factor	Q_e	6.9×10^3
resonator-bus coupling capactince	C_k	9.6 fF
LC Impedence	Z_{LC}	31.8 Ω
TL effective permittivity	ϵ_{eff}	2.3
TL length	l	12.2 mm
TL Impedence	Z_{tml}	50 Ω
Transmon		
Frequency max	ω_q^{max}	6.3 GHz
Josephson energy	$E_J^{max}/2\pi$	30 GHz
Josephson inductance	L_J^{max}	5.4 nH
Critical current	I_c	30 nA
Charging energy	$E_c/2\pi$	180 MHz
Charging capacitance	C_q	107 fF
Impedance	Z_T	224 Ω
Charge zero point flucutaion	Q_{zpf}	3 e
Phase zero point fluctuation	ϕ_{zpf}	0.05 Φ_0
Inharmonicity	$\alpha/2\pi$	192 MHz
Mutual inductnce	M	4 pH
Flux quantum current	I_{ϕ_0}	2 mA
SQUID asymmetry	d	0
Control capacitance	C_{XY}	60 aF
Transmon-resonator coupling (6.3 GHz)		
Detuning	Δ	0.7 GHz
Coupling coefficient	g	45 MHz
Coupling capacitance	C_g	2.75 fF
Dispersive shift	χ	0.63 MHz
Lamb shift	Λ	3 MHz
Qubit purcell decay (6.3 GHz)		
Readout resonator	T_1^{RO}	35 µs
Control line	T_1^{XY}	371 µs

Table 2.1: Qubit-resonator system parameters

Chapter 3

Device fabrication and packaging

Realizing highly coherent superconducting qubits requires precise and stringent control of the device fabrication and packaging steps. Material choice, process variation, surface termination, and the qubit surroundings dictate its coherence, ranging from a few nanoseconds up to hundreds of microseconds. The first section of this chapter describes the developed fabrication process used to realize phonon-protected superconducting qubits on a silicon-on-insulator (SOI) platform, followed by further discussions on material selection, process optimization, and experimental observations. The second section discusses the packaging process, including the design of a copper casing for thermalization and electromagnetic shielding, in addition to the design of radio frequency printed circuit boards (PCB) that act as a multi-layer interposer to perform signal fan-out.

3.1 Device fabrication

Monocrystalline silicon is the backbone material in the semiconductor industry and can currently be refined up to "nine-9s" purity (99.9999999%). Such a nearly defect-free single crystal with a wide bandgap of 1.12 eV, high dielectric constant $\epsilon_r = 11.5$, low microwave losses at cryogenic temperatures ($1/Q_{Si} \approx 10^{-6}$) [32], and robust process industrialization make it an attractive choice for hosting and scaling quantum processors. For a qubit that runs at a frequency of 6 GHz, the loss tangent of silicon sets an upper limit to a qubit relaxation time to $T_1 \approx 1$ ms. This is under the assumption of a unity participation ratio (all the EM field is in the silicon material). In practice, such a lifetime can hardly be reached as it's limited by other dominant loss mechanisms such as TLS, quasiparticles, vortices, and surface piezoelectricity [33], setting a typical transmon lifetime to $T_1 \approx 50\,\mu$s [19, 34].

In particular, using SOI platform permits the co-fabrication of electronic, photonic, and mechanical elements alongside superconducting qubits, thereby unlocking rich opportunities for chip-scale integration of vital quantum moduli. Examples include electro-opto-mechanical transducers and photonic links for qubit transduction and control [35, 36]. Since the bottom oxide (BOX) layer has a high density of TLS and, therefore, a large tangent loss $1/Q_{SiO_2} \approx$

10^{-3}, the oxide has to be etched, and the device has to be suspended. Despite removing the oxide, transmons on SOI have an order of magnitude lower coherence time compared to the bulk silicon substrate. This is potentially due to an increase in surface area and artifacts of the smart-cut process used to make SOI wafers, resulting in $T_1 \approx 1$–$4\,\mu$s [37, 38].

Besides the substrate material, the choice of the superconducting metal and its deposition method has a strong impact on the qubit performance. Aluminum is a type-I superconductor with a critical temperature $T_c \approx 1.2\,\mathrm{K}$ and critical magnetic field $H_c \approx 10\,\mathrm{mT}$. Experimental studies have focused on Al films due to their long-term stability and the self-limiting nature of its native oxide, allowing it to be used reliably and routinely to fabricate Josephson junctions. Nonetheless, other superconductors have shown enhanced qubit lifetime compared to that of Al, including Niobium ($T_1 \approx 100\,\mu$s) and Tantalum ($T_1 \approx 300\,\mu$s) [18]. However, unlike Aluminium, Nb and Ta react with the vapor HF (VHF), which is a critical process used to release the qubit from the lossy BOX layer. Therefore, in this work, we use an all-Al process as our material choice.

3.1.1 Process flow

The multistep fabrication process and the fabricated device images are shown in Fig. 3.1. The SOI wafer used (supplied by Shin-Etsu) features a float zone silicon device layer with a thickness of 220 nm and a crystal orientation of 100 ($\rho \geq 3\,\mathrm{k\Omega\,cm}$). The BOX is a 3 µm-thick layer of SiO_2 on top of a Czochralski-grown silicon handle layer with a thickness of 725 µm ($\rho \geq 3\,\mathrm{k\Omega\,cm}$). The wafer, protected with a resist coating, is downsized from 8″ to 6″ (by MicroPE). Before deposition, the wafer is cleansed with H_2SO_4 and H_2O_2 (piranha solution) to remove organic residues, dipped in HCl to remove metallic contamination, and then in HF to remove the native oxide. Next, 50 nm of aluminum is sputtered at a rate of 15 nm/min. Since the contrast between materials with similar atomic numbers is poor under electron microscopy, and considering that the atomic masses of Si and Al are 28 U and 27 U, respectively, Nb metal (93 U) is used for subsequent electron-beam lithography (EBL) alignments. To define the markers, a 1 µm-thick AZ-MIR 701 resist is exposed (Heidelberg MLA150), developed in MF-26A, and then descummed in O_2 plasma. Next, a 200 nm-thick Nb layer is sputtered at a rate of 28 nm/min, followed by an 1165 liftoff process. The wafer is then protected with resist and diced into 10 mm×10 mm dies for device processing.

The phononic crystal and release holes are then defined. Given the significant membrane size, proximity effect correction (PEC) was set up through BEAMER to address dose distortion. The pattern is subsequently exposed onto 200 nm CSAR resist in an EBL step. The resist is cold-developed in AR600-546, and the pattern is transferred through two consecutive dry etching steps: a 50 nm aluminum etch using a Cl_2/BCl_3 chemistry, followed by a 220 nm silicon etch using $Cl_2/HBr/O_2$ chemistry. The addition of O_2 helps preserve the aluminum thin bridges and corners from being thinned and rounded during the silicon etch. The sample is immediately immersed in water to passivate the chlorinated aluminum, followed by resist stripping in 80 °C 1165 remover for 30 min.

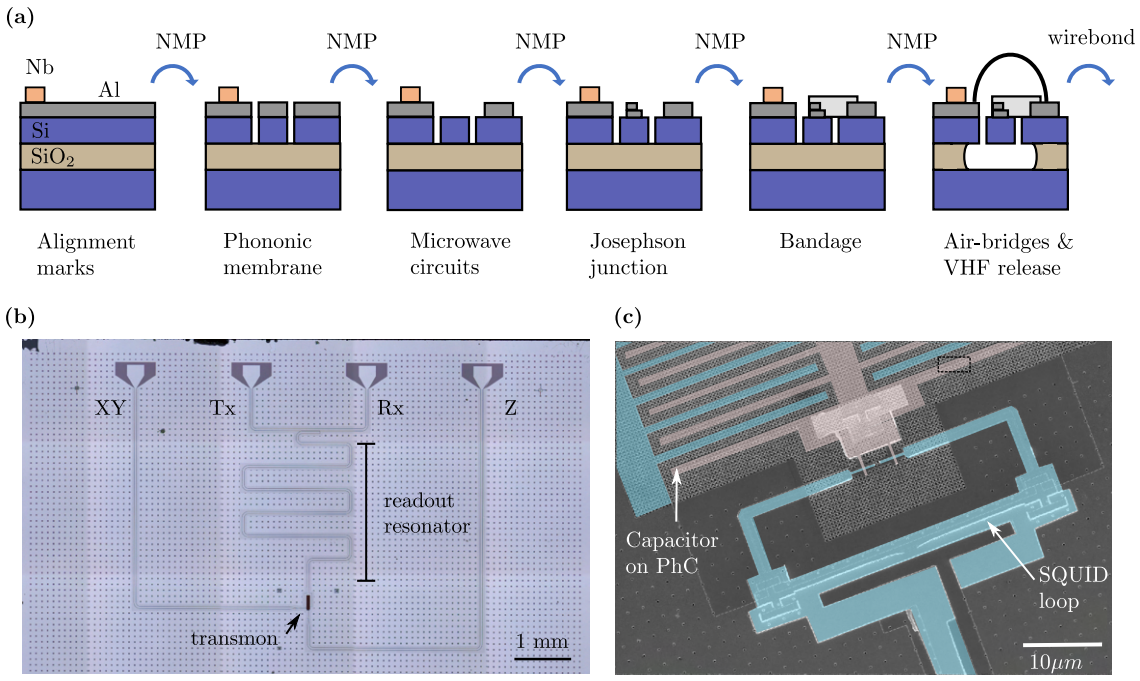

Figure 3.1: Phonon-protected qubit fabrication: (a) process flow, (b) microscope image of the fabricated chip, and (c) false-colored scanning electron micrographs of the transmon.

Next, the microwave circuit is defined by patterning 400 nm PMMA A6 resist in an EBL step. To mitigate stitching errors, a 10 µm field overlap is employed, along with a 2-multipass exposure configured using BEAMER. The resist is developed in MBIK/IPA at a 1:3 ratio, and the pattern is transferred by dry etching 50 nm of Al and 30 nm of Si. The silicon over-etching improves the surface for the Josephson junction evaporation. The sample is once again treated with water to passivate the chlorinated aluminum, and the resist is stripped by a 30 min soak in 80 °C 1165 remover.

The Josephson junctions (JJ) are defined through EBL exposure of a 400 nm/200 nm EL9/CSAR bilayer resist. The exposed resist is then sequentially cold-developed (MBIK-IPA 1:3/AR600-546) and gently descummed in O_2 plasma. The sample is loaded into a double-angle evaporator (Plassys MEB550) and pumped down to a base pressure of 4×10^{-8} mTorr with the assistance of Ti guttering. The subsequent steps are carried out in the following order: a 30 nm Al evaporation at coordinates ($\theta = 45$, $\phi = 45$); dynamic oxidation at 20 mbar for 20 min; another 30 nm Al evaporation at ($\theta = 45$, $\phi = -90$); and a 40 nm Al evaporation at ($\theta = 45$, $\phi = 90$). The evaporation during all these steps is conducted at a rate of 0.3 nm/sec. The liftoff process is carried out by soaking the sample for 2 h in a 50 °C acetone bath, followed by a 30 min soak in 80 °C 1165 remover.

A second EBL step was employed to define a bandage layer. An ion milling process was

used to remove the native oxide layer from the Al, followed by an Al evaporation step at $(\theta = 0, \phi = 0)$, conducted at a rate of 1 nm/sec, resulting in a thickness of 200 nm. A liftoff and cleaning process similar to the one used in the JJ step was carried out. This step also served to increase the Z-line CPW thickness from 50 nm to 250 nm, allowing for a larger current capacity and avoiding heating issues. Aluminum wire bonds were used as airbridges to mitigate slot-line modes, which happen to be at lower frequencies than the main mode in released SOI CPW resonators. This step precedes the releasing process as wire bonding near suspended devices may induce structural collapse.

The device is then released using vapor HF through a 4 µm isotropic oxide etch, conducted at a rate of 36 nm/min. Finally, the sample is mounted and wire-bonded onto a PCB enclosed by a copper box for measurement. The complete set of process parameters is detailed in Appendix A.

3.1.2 Aluminium ethcing vs. liftoff

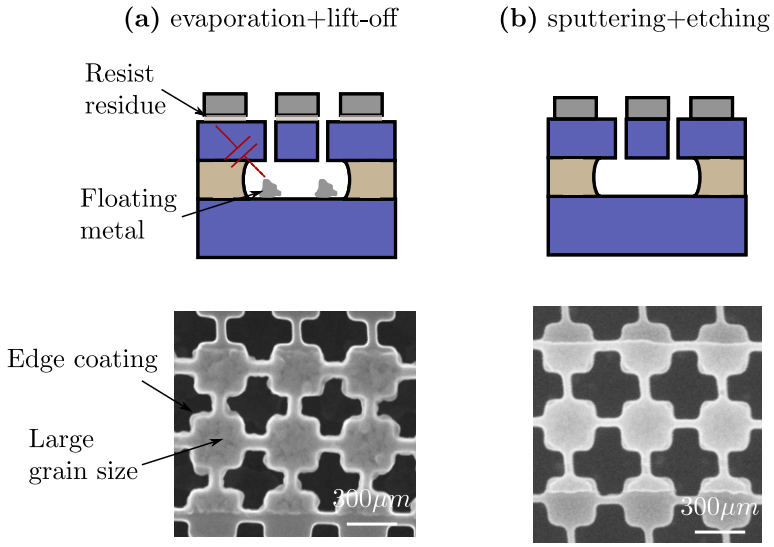

Figure 3.2: Superconducting metal on phononic crystal through (a) Si-etch, e-beam evaporation, liftoff; and (b) Al-sputter, Si-etch, Al-etch.

Most Al deposition attempts on SOI for qubit fabrication were done through e-beam evaporation followed by a liftoff step [37, 38]. However, subtractive processes, such as Al Molecular-beam epitaxy (MBE) or sputtering followed by etching, have the advantage of a cleaner dielectric-metal interface and thus fewer trapped TLSs. This is particularly important given the high electric field at the metal-substrate interface due to the high permittivity

of silicon ($\epsilon_r = 11.5$). A cleaner surface also implies high-quality crystal growth of the superconducting metal [39]. A review of the deposition methods and their influence on the qubit performance can be found in [18].

Subtractive processes are particularly appealing when it comes to defining superconducting metals on a phononic crystal; MBE and sputtering can yield smaller grain sizes than evaporation processes, and the etching process allows the definition of sharp and fine phononic crystal features, whereas evaporation blurs the structure due to sidewall coating. A comparison test was conducted, and the effects can be seen in Fig. 3.2. We also note that evaporation leaves residual metal at the BOX layer that is trapped below the membrane upon VHF releasing. This will compromise the phononic crystal shielding effect, as part of the E-field will couple to a floating Al terminal at the handle substrate, causing dissipation.

Two major issues have to be taken care of when depositing Al using a pulsed-DC magnetron sputtering system. First, the process has to be optimized such that the grain size is as small as possible. This can be achieved by using low power DC values, high sputtering pressure, and a high Argon flow rate [40], along with ensuring an oxide-free interface [41]. Second, Al spiking—caused by electromigration when pure Al is sputtered—can lead to local damage to the Al film. This issue increases with temperature and continues to happen until a diffusion equilibrium is reached. While this is not crucial for planar structures, it can be detrimental for vertical ones (e.g., parallel plate capacitors). This problem can be mitigated by sputtering a 1% Al-Si alloy or by using a Ti/TiN buffer [42]. Both methods and their influence on qubit relaxation time are still the subject of investigation.

3.1.3 Chlorine-based Al/Si etch

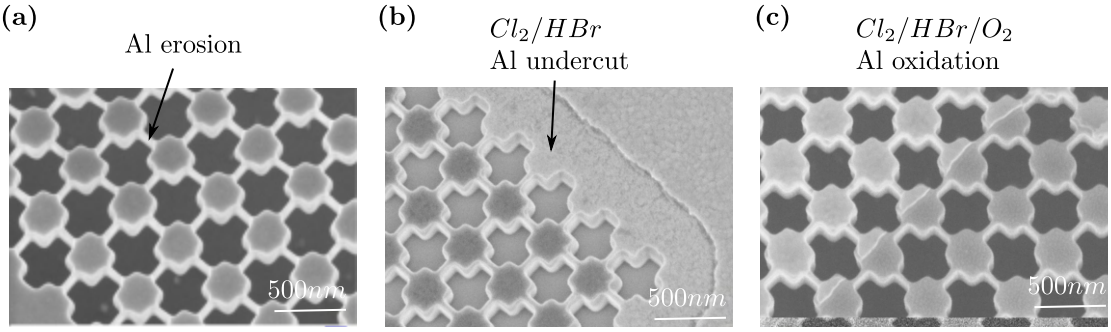

Figure 3.3: Chlorine-based Al/Si etch: (a) Phononic crystal bridge erosion due to poor resist selectivity, (b) Al undercut during the Si etch step, and (c) the effect of Al-oxidation in preventing the undercut.

Chlorine-based chemistries are used to etch both Al and Si. The main difficulty arises

concerning the etching of sub-50 nm phononic crystal features. In order to pattern such dimensions, electron beam lithography has to be used on a sub-200 nm positive-tone resist. However, the resist has to be selective enough to handle the etch of 50 nm Al and 220 nm Si. Although after a few rounds of optimization, resist selectivity was sufficient for large structures, it was not the case for sub-100 nm features used in the phononic crystal, as the resist at the edges tends to erode faster, sometimes causing an electric disconnection, as can be seen in Fig. 3.3(a).

A significant enhancement can be attained by thermally bonding the chip to a carrier wafer before etching using Santovac 5 diffusion pump oil. To increase the selectivity, the etching plasma has to be tuned more towards chemical etching than physical etching while maintaining anisotropy. This can be achieved by controlling the ICP/RF power and the etching/passivating gas ratio. In etching Si, Cl_2/HBr/O_2 chemistry is used. Although HBr alone is known to produce anisotropic Si features, Cl_2 is added to the plasma to increase the etching rate and selectivity [43]. In etching Al, Cl_2/BCl_3 chemistry is used. Although Cl_2 alone readily etches Al, it does not attack Al oxide unless the surface is subjected to ion bombardment, which is typically achieved through BCl_3 gas [44]. However, we observed that the optimized Si etch recipe causes a significant isotropic etch in the Al layer due to the high concentration of Cl_2 radicals, as can be seen in Fig.3.3(b). This has been fixed by the addition of a small amount of O_2 that can oxidize the Al surface to Al_2O_x and stop the under-etch at the expense of lower selectivity [45]. The final etched phononic crystal structure is shown in Fig.3.3(c).

A final remark on the choice of defining the phononic crystal before the microwave layer: We observed that if the microwave layer is defined first, the CSAR resist sticks very strongly and hardens to the Si exposed surfaces during the phononic crystal etch due to the elevated temperature. The resist was very difficult to remove, detrimentally affecting the yield, adhesion, and quality of the subsequent Josephson junction evaporation steps. The issue was resolved by defining the phononic crystal first and then the microwave layer. That is also the choice behind using a 400 nm-thick PMMA so that it covers uniformly the topography of the etched phononic crystal.

3.1.4 Josephson junction and bandage

The Josephson junction and bandage are critical parts of the qubit and are the most sensitive in terms of fabrication, as illustrated in Fig. 3.4(a). To operate in the transmon regime ($E_J \gg E_C$), the junction critical current I_c is typically in the range of 10–100 nA, corresponding to JJ area of 0.02–0.1 μm^2. Therefore, a pocket of a few unit cells in the phononic crystal is made to accommodate the JJ, as can be seen in Fig. 3.4(b). This will, nonetheless, compromise the phononic crystal bandgap by allowing subgap cavity modes. The small nature of the JJ implies that a few nanometer fluctuations in its size can result in a hundred megahertz shift in the transmon frequency (ω_q). This large sensitivity mandates a precise and controlled fabrication process and routine test structures to monitor I_c drift and fluctuations, as illustrated in Fig. 3.4(d). This can be done by noting that I_c can be related to the room

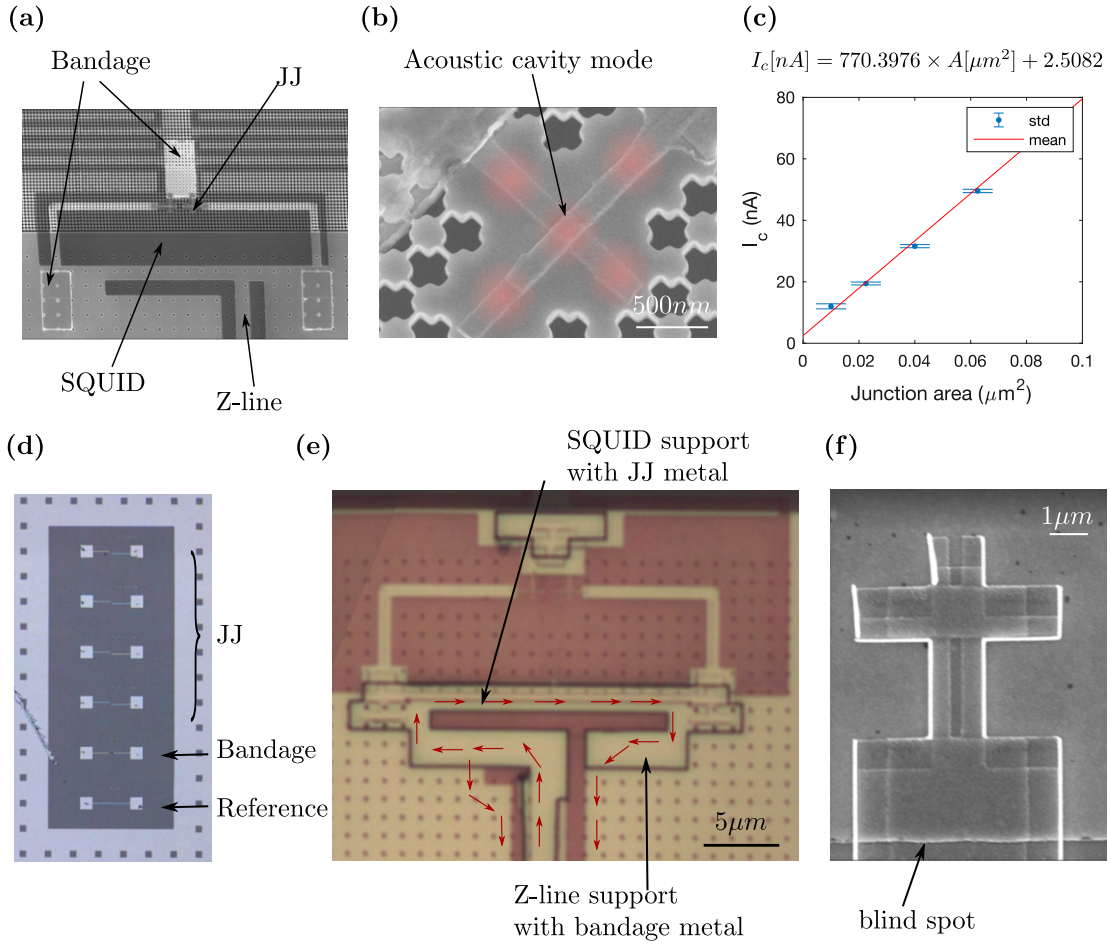

Figure 3.4: Josephson junction: (a) SEM image of the qubit SQUID section, (b) JJ on a phononic crystal island, (c) critical current vs junction area plot constructed with the Ambegaokar-Baratoff formula, (d) JJ and bandage room temperature test structures, (e) microscope image of the SQUID area, and (f) cross structure.

temperature measurement of the junction resistance R_n via the Ambegaokar-Baratoff formula [46]:

$$I_c = \frac{\pi\Delta(T)}{2eR_n}\tanh[\frac{\Delta(T)}{2k_BT}]$$
$$I_c \approx \frac{\pi\Delta(0)}{2eR_n} \quad (T \gg T_c) \tag{3.1}$$

where $\Delta(T)$ is the superconducting gap energy, approximately $\Delta(0) \approx 170\,\mu$eV for Al. The slope of the critical current I_c vs. JJ areas is routinely used as a calibration measurement, as shown in Fig. 3.4(c). The metal-metal interface between the evaporated junctions and the rest of the circuitry contains a native oxide due to the separate evaporation steps, resulting in a stray junction at the contact area. The contribution of stray junctions to the qubit Hamiltonian is negligible when the stray junction area is made larger. Additionally, the associated TLS losses decrease as the junction area increases, as the voltage drop due to an increase in capacitance, $V = Q/C$ [47]. Making the overlap large was not possible in our qubit, as it would deteriorate the quality of the phononic bandgap. An in-situ ion-milling step can be done to remove the native oxide, but it will also damage the silicon substrate, negatively influencing the qubit coherence. The approach taken is to use a separate lithography step followed by ion milling, metal evaporation, and liftoff to galvanically connect the JJs with the rest of the microwave circuit, in a process known as "bandage," as can be seen in Fig. 3.4(a).

We've experienced many failed attempts, and here we list the lessons learned and remarks noted to reliably fabricate a tunable transmon on SOI:

- We observed variability in I_c ranging from 200–400 nA when performing the JJ test on a bare SOI substrate compared to an SOI surface where the sputtered aluminum was etched (due to induced roughness). A change in I_c is also observed during variable cleaning times in heated 1165 remover and post-baking steps (due to junction annealing). These observations indicate that a consistent fabrication flow must be followed to lock the qubit frequency, and the JJ test structure should follow the same process flow as the qubit. An additional 30 nm silicon over-etch was found to be highly effective in JJ adhesion and yields. Additionally, performing a descum process before the JJ evaporation step not only reduces residual resist trapped underneath the junction but also helps achieve reproducible JJ resistance and, thus, a controlled qubit frequency [48].

- The JJ pads have an area of $4\,\mu\text{m}^2$ and evaporated on top of around 5 nm native AlO_x dielectric, corresponding to a parasitic capacitance of 70 fF. Without a bandage (or a failed bandage process), the parasitic capacitance was observed to drastically reduce the qubit frequency from 6 GHz to 2–3 GHz. A careful ion-milling process was developed, and additional bandage test structures were incorporated on every qubit fabricated chip. The bandage resistance can be measured at room temperature and be compared to a short circuit reference line to detect any process mistakes, as shown in Fig. 3.4(d).

- Due to the nature of angle evaporation of the JJ, if care is not taken, some narrow blind spots won't be metalized, causing a discontinuity in the JJ metal, as seen in Fig. 3.4(f). Also, it is advisable to have all three JJ metal layers and the microwave Al layer to be exposed and in contact with the bandage metal to ensure a full galvanic

connection among them. This was achieved by the following cross-structure, shown in Fig. 3.4(f).

- Even with a clean and precise JJ fabrication process, junction aging—temporal drift in the junction resistance over time—occurs and must be controlled. One explanation of its origin is that the tunnel barrier might incorporate aluminum hydrates where the OH group may stem from organic resist residuals or from water dissociation at the aluminum oxide interface [49]. It was shown that better long-term stability is obtained when junctions are annealed at a few hundred degrees Celsius in a vacuum, which was tested for a few of our qubits after releasing the device [50]. We abandoned this step as the vacuum oven used was contaminated, and the process is left for future investigation.

- A failed bandage can prevent a closed DC loop in the SQUID, preventing the qubit from being tunable. We use JJ metal across the entire loop to assure an uninterrupted connection in case of a failure in the bandage process, as shown in Fig. 3.4(e).

- An issue was faced in tuning the qubit through the Z-line, as we were reaching the superconducting critical current of Al, which is around $100\,\mathrm{GA\,m^{-2}}$. The narrowest region in the Z-line has a thickness of 50 nm and a width of 1 µm, allowing a critical current of $\pm 5\,\mathrm{mA}$. We need $\pm 0.5\,\mathrm{mA}$ to achieve one flux quantum, giving a mutual inductance of 2 pH. Although this is less than the critical current, we faced occasional heating issues that prevented full tuning of the qubit. The problem was addressed by avoiding the release of the Z-line (better thermalization through the BOX) and supporting the Z-line with an additional 200 nm of Al through the bandage evaporation process, as illustrated in Fig. 3.4(e).

3.1.5 Device release

Releasing all the microwave circuits is a crucial step as the underlying SiO_2 hosts a high density of TLS. It also prevents acoustic radiation into the substrate, completing the acoustic bandgap. This can be done by etching release holes in the Si layer followed by isotropic oxide etch. It is well known that Al is heavily corroded in common aqueous acids and alkaline solutions due to the formation of $[Al(H_2O)_6]^{3+}$, $[Al_2(OH)_2]^{4+}$, and $[Al_7(OH)_{16}]^{5+}$ complexes. However, this corrosion seems to be inhibited in concentrated HF acid. This is due to the following reaction that produces AlF_3, which is hardly soluble in anhydrous media [51].

$$2\,\mathrm{Al} + 6\,\mathrm{HF} \longrightarrow 2\,\mathrm{AlF_3} + 3\,\mathrm{H_2} \tag{3.2}$$

Therefore, concentrated HF can be employed to release Al-SOI devices. It has been found that the same applies in vapor HF (VHF) processes, and Al is not heavily corroded during anhydrous HF vapor treatment. VHF is becoming a convenient method to release SOI devices as it doesn't require the sensitive critical point drying step that is typically needed

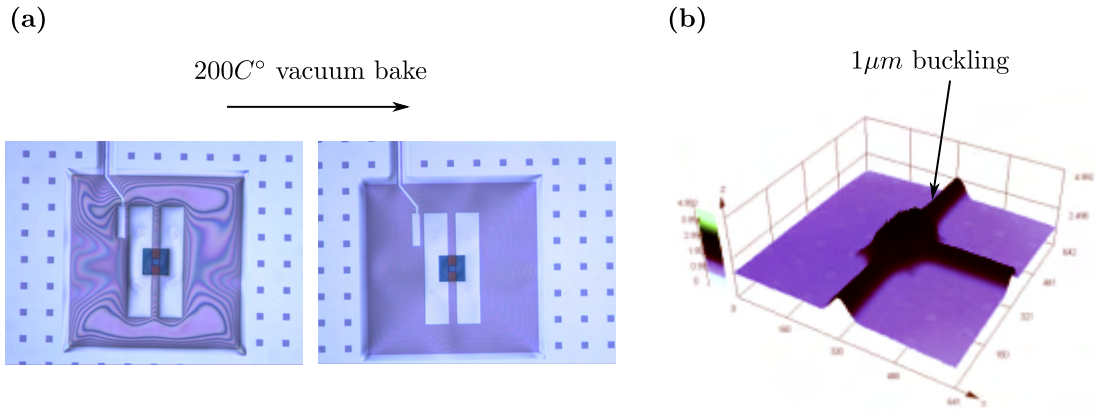

Figure 3.5: Device release: (a) water condensation and membrane stress addressed by a vacuum bake, and (b) upward 1 μm buckling of a suspended qubit.

to reduce surface tension due to the capillary force of water (stiction). A gaseous etchant also penetrates smaller features more easily and allows longer undercuts. However, the Al-HF reaction can still be provoked by the condensation of water formed during the etching of the oxide.

$$4\,\mathrm{HF} + \mathrm{SiO_2} \longrightarrow \mathrm{SiF_4(g)} + 2\,\mathrm{H_2O} \tag{3.3}$$

Therefore, pressure, temperature, and etch rate have to be carefully monitored to avoid such condensation. We observed a small condensation of water under large areas that are not well-vented, in addition to undulation in the suspended membrane suggesting built-up stress. Both issues were addressed by the same vacuum backstep used to stabilize the Josephson junction (200 °C for 2 h), as can be seen in Fig. 3.5 (a). Qubits with an area up to 300×300 μm can be fully suspended and are typically buckled upward by 1 μm (Fig. 3.5 (b)).

3.1.6 Ground plane engineering

Establishing a lossless strong ground plane is an important task for realizing robust quantum circuits. We discuss two used stratgies.

First, when simulating thin superconductors, it is common practice to assume a perfect electric conductor (PEC) boundary condition, where the tangential E-field $E_t = 0$. For real normal conductors, the EM field decays exponentially (normal skin effect) with depth $\delta = \sqrt{2/\omega\sigma\mu}$, and the surface impedance can be calculated as $Z_s = E_t/H_t = (1+j)\sqrt{\omega\mu/2\sigma}$, which can be used in simulation as a correction. For superconductors and at a frequency well below their energy gap frequency Δ, the EM field decays exponentially (anomalous skin effect) with a London penetration depth λ_L, which is independent of frequency. The surface

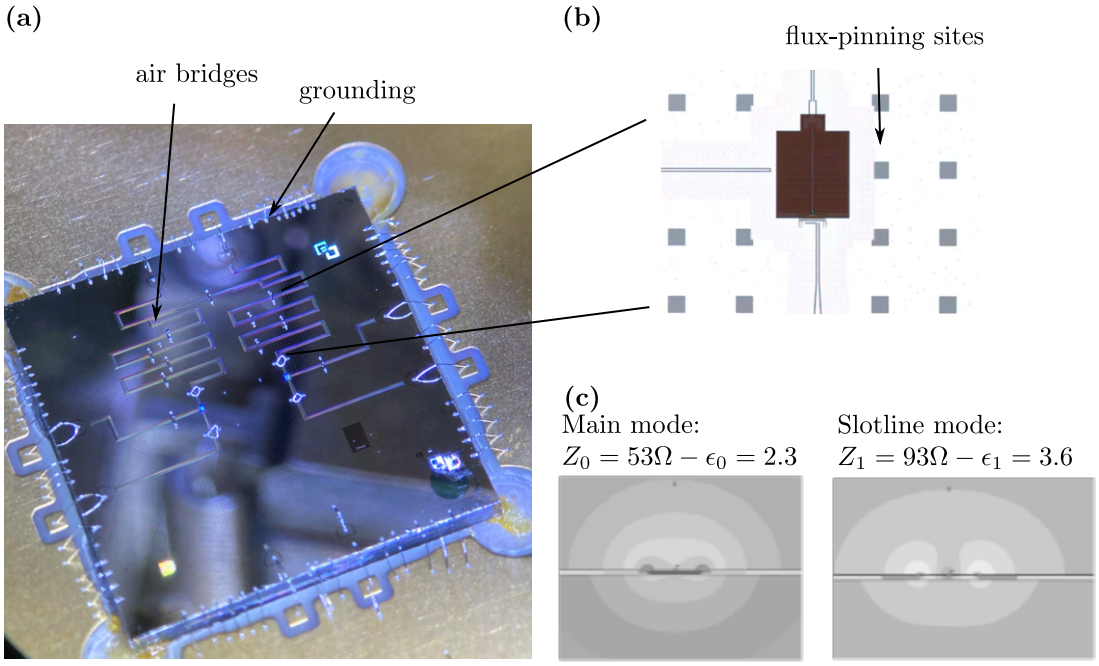

Figure 3.6: Ground plane engineering: (a) Chip-scale image showing airbridge and ground wire bonds, (b) Flux-pinning sites, and (c) Mode profile simulation of suspended CPW on SOI.

impedance is then $Z_s = E_t/H_t = j\omega\mu_0\lambda_L$, and it is modeled by a simple sheet inductance of $L_s = \mu_0\lambda_L$. For aluminum, $\lambda_L \approx 16\,\text{nm}$, $L_s \approx 20\,\text{fH}/\square$, and at 6 GHz, $Z_s \approx 700\,\mu\Omega/\square$. The point is, for long distances (on a chip scale), a large impedance develops between different ground planes, causing issues including: (i) Z-line current distribution that affects the SQUID flux, and (ii) CPW slotline modes. Slotline modes are high-order modes that arise when there is high impedance between the two ground planes of the CPW and can be excited by discontinuities or asymmetries. Unlike CPW on a Si substrate, CPW on an SOI substrate tend to have a slot-line mode with larger effective permittivity than the main mode. This leads, for example, to the slot-line frequency for the readout resonator to be closer to the qubit frequency, exacerbating the Purcell decay, as illustrated in Fig. 3.6(c). There are two main approaches to mitigate the discussed issues. The first approach is to strengthen the ground with as many wire bonds as possible with the PCB ground. The second grounding approach, known as *airbridges*, is used to short both sides of the CPW waveguide manually with a short wire-bond [52, 53], as shown in Fig. 3.6(a). However, we noticed that the friction power used in wire bonding - if done closely to the transmon- can cause the released structure to collapse; therefore, we first form the airbridges and then release the structure.

Second, aluminum is a type-1 superconductor, and superconductivity is abruptly destroyed via a first-order phase transition when the strength of the applied magnetic field rises above a critical value $H > H_c$. Even at $H < H_c$, superconductors rarely exhibit a complete field expulsion (Meissner effect), and grain boundaries, normal inclusions, and other defects serve to trap flux in the form of superconducting vortices (even in thin-film type-I superconductors). A vortex is a supercurrent that circulates around a core that is non-superconducting (metal) with a suppressed order parameter, causing decoherence to nearby qubits and resonators. The minimum field required for a vortex to form on a strip waveguide of width W is proportional to Φ_0/W^2, where Φ_0 is the flux quantum [54]. In our fabricated device, the largest width is the ground plane, and flux-pinning sites (square cheesing) were used throughout the chip to minimize this effect by reducing the total area and pinning the vortex far from the qubit once generated [55], as shown in Fig. 3.6(b).

3.2 Device packaging

The susceptibility of qubits to their environment mandates careful microwave package design to reduce and limit qubit relaxation and dephasing times. The purpose of packaging is to suppress qubit coupling to the environment's electromagnetic noise yet allow low-noise communication conduits to control and read the qubit state. Additionally, the packaging should serve as a thermal sink for excess and latent thermal energy accumulated during qubit operation. In this section, we discuss the shield designs and the PCB used to enclose and package the phonon-protected superconducting qubit, with a detailed discussion available in Ref. [56].

3.2.1 RF cavity shield

Decoherence channels couple to a qubit through its electric or magnetic dipole moment. For transmon qubits, the electric dipole moment presently dominates. One way to suppress unwanted environment coupling is to use a qubit planar symmetry that has a suppressed dipole moment (which radiates easily to free-space modes) and enhanced high-order multipole moments (non-radiating). A better approach is to define the qubit environment by placing it in a metallic cavity with a low density of electromagnetic states around the qubit frequency, as depicted in Fig. 3.7(a) [57]. This is analogous, in principle, to the reduction of the density of states (DOS) of acoustic modes by placing the qubit on a phononic crystal. To increase the package fundamental mode frequency and suppress material-induced losses, the chip is suspended to form a cavity above and below it, which can be lumped-modeled (at subwavelength dimensions) by two parallel capacitors C_t and C_b, as depicted by Fig. 3.7(b). The inductor L_w is determined by the wirebonds connecting the PCB and the chip ground net. Each 1 mm-length wirebond of 25 µm diameter is approximately modeled by a 1 nH inductor. It is intuitive then to see that increasing the fundamental mode frequency ($\omega = 1/\sqrt{L_\mathrm{w}(C_\mathrm{t} + C_\mathrm{b})}$) can be done by reducing the capacitance (increasing the top and bottom

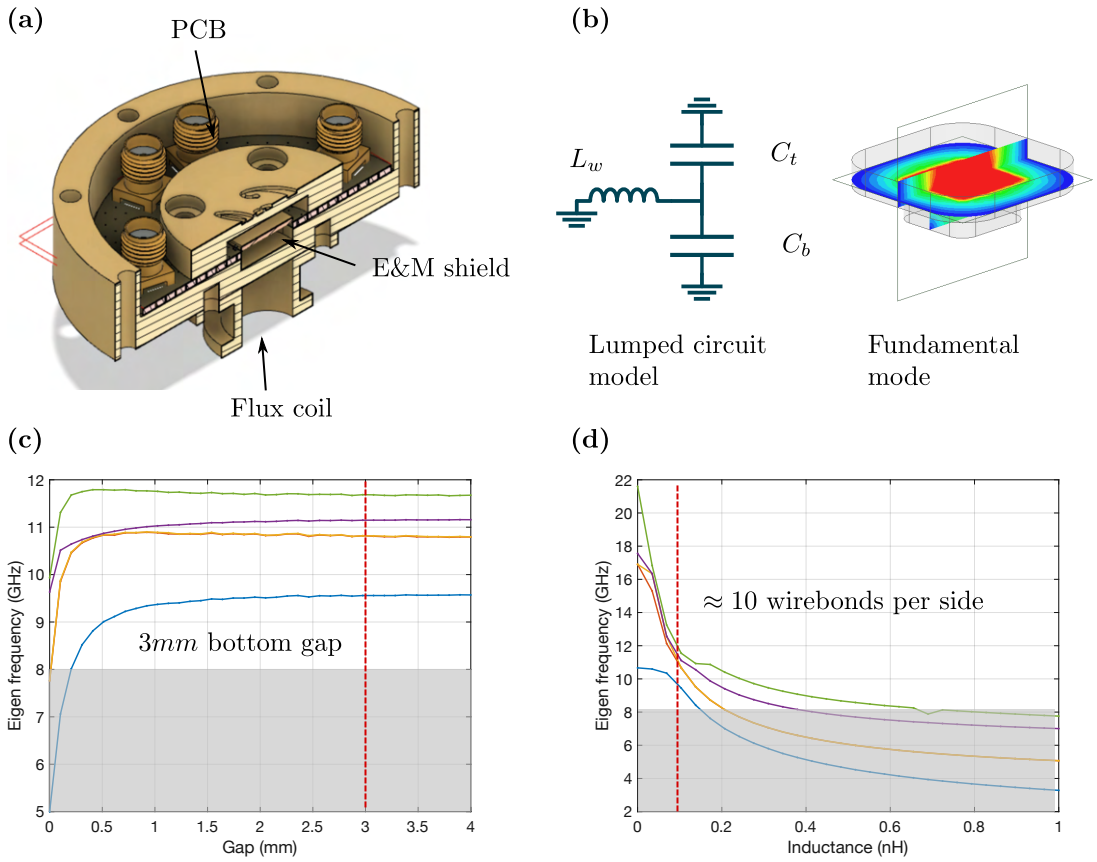

Figure 3.7: Shielding cavity design: (a) CAD drawing ; (b) lumped circuit model and E-field profile of the fundamental mode; (c), cavity modes as a function of bottom cavity height; and (d) cavity modes as a function of the inductance per chip side.

cavity length) or reducing the inductance (using a large number of parallel wirebonds). More complex circuit models were studied for higher frequency and chip size [58]. A full EM eigenmode simulation (Ansys HFSS) was performed to calculate the normal modes of the cavity. The top cavity was fixed to 3 mm, and the bottom cavity length and inductance per chip side were varied, as shown in Fig. 3.7(c) and (d), respectively. To pust the first fundamental frequency above 9 GHz, we set the length of the bottom cavity to 3 mm and require a minimum of 40 ground wirebonds, which corresponds to 0.1 nH inductance per chip side. The Purcell decay of the qubit due to the cavity shield can be calculated in a similar fashion to the qubit-readout resonator using equation Eq. 2.68.

The choice of the shield's material is also important. Tunable transmons are particularly sensitive to magnetic field fluctuations. Consequently, magnetic metals (e.g., Nickel)

or materials with magnetic compounds are generally avoided. Materials with high magnetic permeability, such as mu-metal, can be used as part of the dilution refrigerator to suppress magnetic field fluctuations, as will be discussed in Chapter 4. Another approach is to incorporate type-I superconductors, such as aluminum, in the package body. Once such a material turns superconducting, it expels the magnetic field from its core due to the Meissner effect, as long as the magnetic field does not exceed a specific material- and temperature-dependent threshold. In addition, aluminum has reduced ohmic losses as it superconducts but still suffers from the TLS of its surface oxide. This also means high-quality factor cavity modes and thus low Purcell decay via Eq.2.68. A disadvantage of aluminum is its poor thermal conductivity (a superconductor is a perfect conductor of charge but a poor conductor of heat). Oxygen-free high-conductivity copper is a common choice for shielding, particularly for high-thermal load applications. The thermal conductivity of copper decreases linearly with temperature and reaches a value of approximately $0.5\,\mathrm{W\,cm^{-1}\,K^{-1}}$ at 20 mK. On the other hand, the thermal conductivity of superconducting aluminum decreases exponentially faster at similar temperatures and is around $0.025\,\mathrm{W\,cm^{-1}\,K^{-1}}$ at 20 mK. Regardless of the metal choice, at cryogenic temperatures, heat flow from the chip is almost entirely dominated by Kapitza boundary resistance at the interfaces, and high pressure should be applied when mounting [59]. Finally, when copper is used, an external flux coil can be used to apply global magnetic fields to bias all qubits, as shown in Fig.3.7(a). In this work, we used both aluminum and copper interchangeably.

3.2.2 PCB and wirebonding

A 4-layer 1.2 mm-thick PCB was designed as an interposer between the SMA connectors and the chip launchpads. A buried CPW waveguide was used to isolate the lines from environmental noise and, more importantly, to protect the lines from physical contact with the top grounded lid that forms the shielding cavity, as illustrated in Fig. 3.8(a). The embedded CPW is defined in layer 2 (L2) and is impedance-matched with the coaxial cables and the chip CPW (Z =50 Ω). Good impedance matching leads to lower insertion losses and improved signal integrity, both of which are critical for high-fidelity qubit control and readout. In particular, when operating the readout resonator in the transmission mode rather than the reflection mode, a slight impedance imbalance between the input and output ports results in an asymmetric Lorentzian line shape that complicates the fitting process [60]. Additionally, impedance mismatch of the PCB waveguide allows the formation of an interposer cavity mode that has a Purcell decay of the qubit via Eq. 2.68. *Impedance-process-control* was also requested from the PCB vendor to ensure precise control of the impedance values.

Straight surface mount SMA connector is fixed at one end of the waveguide and the center pins are soldered to a pad at the L1 layer. Large reflection was observed at the SMA interface due to the proximity of the underneath ground plane in the L2 layer. Anti-pads - void areas around the SMA pad - on the L1 and L2 layers were used to reduce parasitic capacitance and thus reflection. To transfer the signal from and to the L2 layer, *via-in-pad*

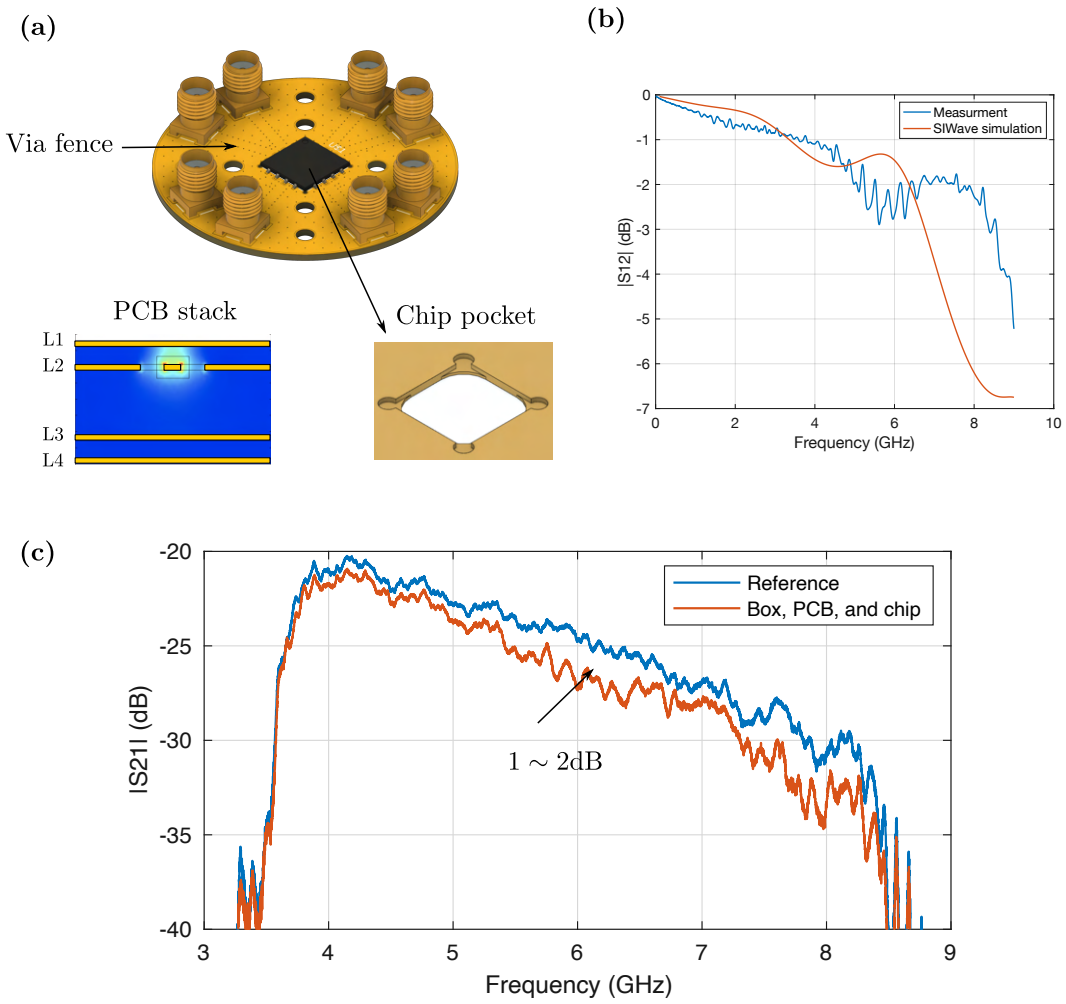

Figure 3.8: PCB design: (a) CAD drawing of the designed 4-layer PCB, (b) S21 comparison between simulation and experimental data, and (c) closed-loop PCB and RF cavity test in a dilution fridge.

process was employed (small high-speed vias filled with epoxy and plated with copper). Via fences - rows of metalized holes drilled through the substrate material- were used to reduce cross-talk between adjacent signal lines and supress slotline modes. The spacing between the vias should remain small compared to the wavelength (subwavelength regime $\sim \lambda/20$). The *soldermask* layer - a thin layer of polymer that is used to protect the copper from oxidation and shorts during operation - was completely removed from the L1 and L4 layers except for the SMA connector area. The exposed copper is then plated with gold to prevent oxidation

and improve the solderability of copper contacts through electroless nickel immersion gold (ENIG) plating process. A PCB cutout to remove lossy FR-4 laminate beneath the chip was made in addition to a *partial-milling* of the corners to form ledges that carry the chip with the aid of a small amount of GE varnish, as illustrated in Fig. 3.8(a).

The PCB S-parameters between two SMA connectors and two wirebonds were simulated using Ansys SIWave, demonstrating good agreement with the experimental measurement data, as shown in Fig. 3.8(b). The return loss is primarily limited by the wirebond parasitic inductance and capacitance. Aluminum wire bonding was chosen over gold since it is superconductive and suppresses ohmic losses. A 1 mm wirebond with a 25 µm diameter is modeled approximately by a 1 nH inductor and 20 fF capacitance, resulting in an impedance of $Z = \sqrt{L/C}$ =223 Ω, interface reflection coefficient $\Gamma = (Z - Z_0)/(Z + Z_0) \approx 0.63$, and stub reflection ≈ 0.1.

The PCB and RF cavity shield were tested in a closed-loop connection in a dilution fridge, as shown in Fig. 3.8(c). An approximate 1–2 dB insertion loss and −60 dB crosstalk to nearest neighbors were measured in the 4–8 GHz range, with no appearance of box modes. Further reduction in insertion loss can be achieved by replacing the FR-4 with low-loss Rogers laminates.

3.3 Epitaxial Si/SiGe superlattice investigation

In this section, we investigate the fabrication of a 1D epitaxial phononic superlattice. The term "epitaxial" implies that the crystal structure of the deposited SiGe layer aligns with and grows in a well-ordered manner on the crystalline structure of the silicon substrate. The process typically involves introducing precursor gases, such as silane (SiH_4) and germane (GeH_4), into a high-temperature reactor chamber. Under controlled conditions, these gases decompose, and SiGe atoms are deposited onto the silicon substrate, forming a SiGe layer. The composition of the SiGe layer can be adjusted by controlling the ratio of silicon to germanium precursors. The primary motivation for realizing an epitaxial phononic bandgap is the low TLS density (unlike the etched PhC in SOI). However, the 1D superlattice has an incomplete phononic bandgap and exhibits phonon modes at non-orthogonal directions. Even in the orthogonal direction, there are non-overlapping longitudinal and transversal bandgap, as shown in Fig. 2.9(b). So, we expect a reduction (rather than elimination) in the phonon density of states and a slight increase in the TLS lifetime (Γ_t), with the advantage of a lower TLS density (ρ) compared to the SOI membrane.

When the lattice mismatch between SiGe and the substrate (usually silicon) is large, strain accumulates as the SiGe layer grows. At some critical thickness, the strain becomes too high, and the material undergoes relaxation, resulting in the creation of defects. The lattice constant for $Si_{1-x}Ge_x$ is

$$a(x) = 5.4 + 0.2x + 0.027x^2 \text{ Å} \tag{3.4}$$

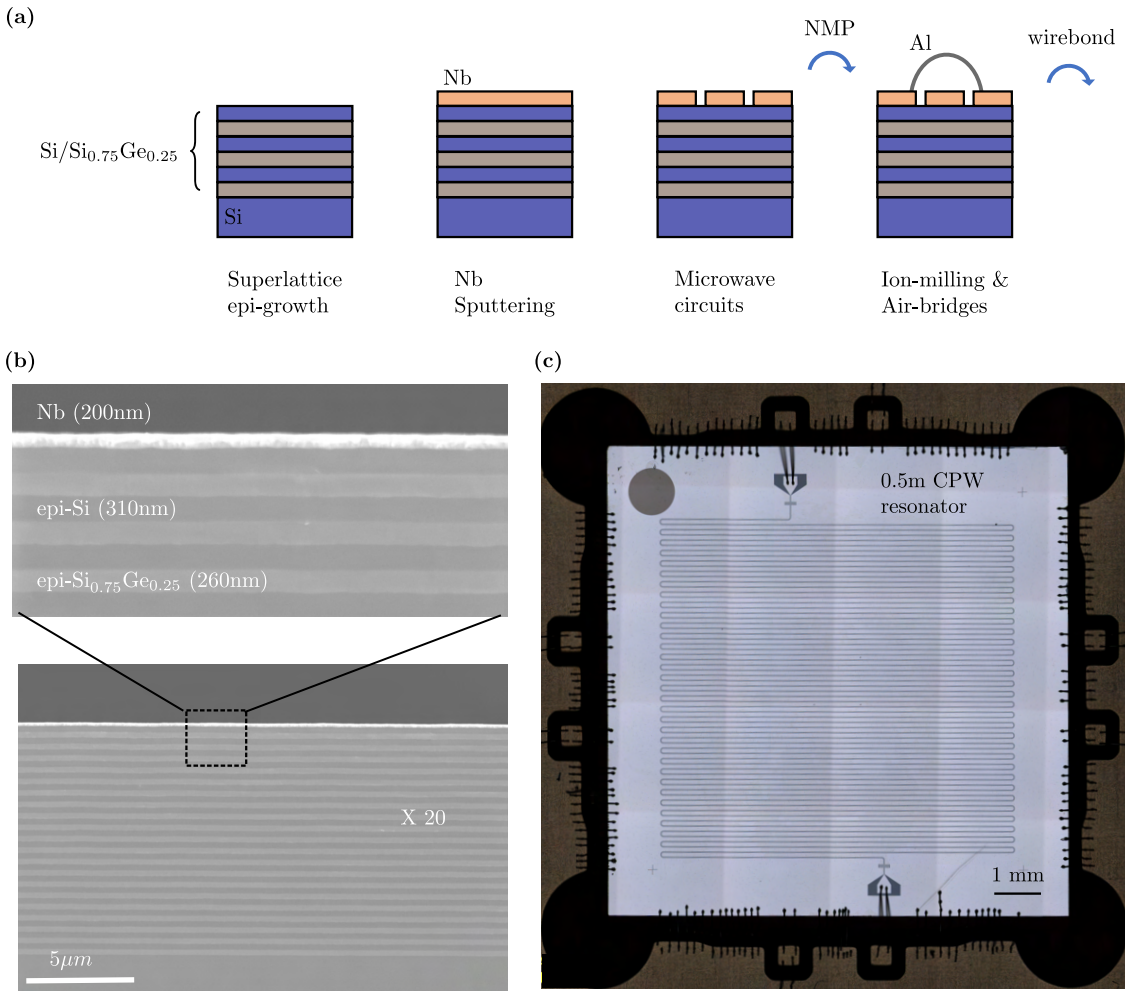

Figure 3.9: Si/SiGe superlattice: (a) fabrication process flow, (b) cross-section SEM image, and (c) a microscope image of the fabricated 0.5m CPW resonator.

We proceed with designing a longitudinal phononic bandgap around 7 GHz with a bandwidth of approximately 1 GHz, following the derivation presented in Section 2.3.1. The density (ρ), Young's modulus (E), shear modulus (G), and the Poisson ratio (ν) for $Si_{1-x}Ge_x$ are given by:

$$\begin{aligned} \rho(x) &= 2.32 + 3.49x - 0.49x^2 \text{ g cm}^{-3} \\ E(x) &= 130.2 - 28.1x \text{ GPa} \\ G(x) &= 51.0 - 10.85x \text{ GPa} \\ \nu(x) &= 0.278 - 0.005x \end{aligned} \tag{3.5}$$

The Lamé constants can be retrieved from the above moduli using Eq. 2.90. The superlattice

specification can be achieved with N=20 pairs of Si with a thickness of 310 nm and $Si_{0.75}Ge_{0.25}$ with a thickness of 260 nm. Unfortunately, this exceeds the critical thickness limit (∼10 nm), and film relaxation will occur [61]. However, the film quality will still be in near-epitaxial condition and is worth investigating.

The fabrication process flow is illustrated in Fig. 3.9(a). We start from a high resistivity undoped silicon wafer and proceed in removing the native oxide for smooth epi-growth in two steps. The first is a gentle dip in HCl and HF in a wet bench followed by DI water rinse. The second step is to perform a vacuum back at 1100 °C with H_2 inside the epitaxial chamber (Applied Material - Epi 200 Centura). This is a reduction process that remove the native oxide as in

$$SiO_2 + H_2 \longrightarrow SiO\uparrow + H_2O\uparrow \tag{3.6}$$

Next, we grow 260 nm of $Si_{0.75}Ge_{0.25}$ at 650 °C, followed by 310 nm of Si at 800 °C. The process is repeated to create 20 pairs, and a temperature ramp step is used in between the two layers to avoid thermal stress. Next, we sputter 200 nm of superconducting Nb (RF-sputter). A cross-section of the grown stack is shown in Fig.3.9(b). We perform optical lithography and dry etch to define a 0.5 m CPW resonator in transmission mode with a

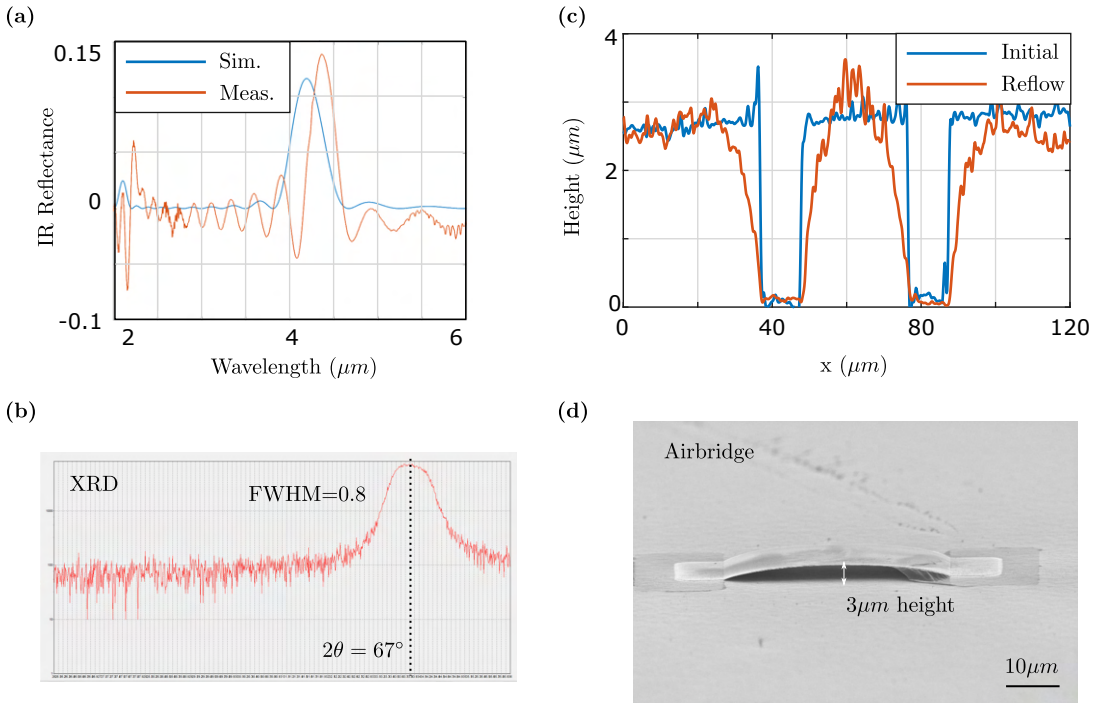

Figure 3.10: Si/SiGe superlattice characterization: (a) IR reflection from FTIR measurement, (b) XRD characterization, (c) 3D profiling of the scaffold resist before and after reflowing, and (d) SEM image of airbridge test structure.

Free Spectral Range (FSR) of 100 MHz. This generates a comb of resonances, where the internal (κ_i) and external (κ_e) decay rates can be extracted at different frequencies (inside and outside the phononic bandgap) using Eq.2.63. The device is shown in Fig. 3.9(c). The detailed steps of the fabrication process flow can be found in the appendix.

A rapid way to assess the quality of the superlattice is to test the optical bandgap, which occurs in the mid-IR spectrum. The optical reflectivity can be computed using the same analysis presented in Section 2.3.1, while substituting the appropriate permittivity (ϵ) and permeability (μ) for $Si_{1-x}Ge_x$:

$$\begin{aligned} \epsilon_r^2(x) &= 3.42 + 0.37x + 0.22x^2 \\ \mu(x) &= 1 \end{aligned} \tag{3.7}$$

The simulation results are in good agreement with the Fourier-transform infrared spectroscopy (FTIR) measurement, as illustrated in Fig. 3.10(a). Next, we assess the crystal quality of a single layer of grown $Si_{0.75}Ge_{0.25}$ film through X-ray crystallography (XRD). We measured a Full Width at Half Maximum (FWHM) of 0.8° at 2θ =67°, as shown in Fig. 3.10(b).

A final issue to report is that the very long CPW resonator is highly susceptible to slot-line mode excitation, making resonance tracking intractable. Hundreds of airbridges are needed to suppress the slot-line modes, which is not practical to implement with wire bonds, as done for the SOI qubit. We developed a lithography-based airbridge process [62]. The process starts by spinning 3 µm-thick resist and reflowing it, giving a smooth arch that acts as a scaffold for the Al airbridge, as shown in Fig. 3.10(c). This is followed by ion milling and 200 nm Al evaporation, similar to the bandaid process described for the SOI qubit. Finally, a second lithography step is performed to define the pads, followed by aluminum wet etching. A test structure of an airbridge is shown in Fig. 3.10(d). Further efforts are still needed to characterize the device and optimize the Si/SiGe superlattice growth. The complete set of process parameters is detailed in Appendix A.

Chapter 4

Experimental setup and calibration

To observe quantum effects, the microwave circuit has to be cooled down to milli-Kelvin temperatures for two main reasons. First, the circuit must be well-decoupled from uncontrolled degrees of freedom, ensuring that the energy levels of the system are considerably less broad than their separation ($\omega_q \gg \kappa_i$). For a transmon, visible inharmonicity requires $\kappa_i/2\pi \ll E_c/\hbar \sim 200\,\mathrm{MHz}$. The first step is to eliminate ohmic losses in the metal by operating in the superconducting regime. For aluminum, cooling below the critical temperature ($T < T_c \sim 1.4\,\mathrm{K}$) allows a Q-factor up to 10^6, corresponding to a 5 kHz linewidth at a 5 GHz qubit frequency. However, a microwave oven runs at 2.45 GHz and reaches a Q-factor up to 10^6, yet quantum effects are not typically observed in the kitchen. A second and more stringent condition requires the energy needed to excite the qubit to be much larger than thermal excitation, $\hbar\omega_q \gg k_B T$. More specifically, the excited state probability of a qubit with frequency ω_q and at a temperature T follows the Bose-Einstein distribution:

$$P_e = \frac{1}{e^{\hbar\omega_q/k_B T} - 1} \tag{4.1}$$

Therefore, to attain $P_e \approx 10^{-9}$ at $\omega_q = 5\,\mathrm{GHz}$, the qubit has to be cooled down to $T = 10\,\mathrm{mK}$, a feasible temperature with a $^3\mathrm{He}{-}^4\mathrm{He}$ dilution refrigerator. In practice, however, $P_e = 0.1\%$, indicating an effective $T_{\mathrm{eff}} = 35\,\mathrm{mK}$, a discrepancy that has not yet been fully understood but is thought to be due to non-equilibrium quasiparticles [63], which lose energy to the qubit, driving it out of thermal equilibrium. These quasiparticles, or broken Cooper pairs, can be generated by blackbody radiation from higher temperature stages reaching the sample via the wires or stray light [64]. In this chapter, the operational principle of the $^3\mathrm{He}{-}^4\mathrm{He}$ dilution refrigerator will be briefly overviewed, followed by a discussion on the sample-stage design, magnetic shielding, and wiring strategies. The second part of the chapter discusses the developed RF-FPGA hardware used to control and readout the qubit, whereas the final chapter discusses protocols used to calibrate a tunable transmon qubit before measurements.

4.1 Dilution refrigerator

A dilution refrigerator (DR) is a type of cryogenic device commonly used to cool quantum circuits to a few millikelvins. The Bluefors LD250 - a commercially available DR unit used in this work- consists of two co-working refrigeration subsystems: (i) the pulse tube refrigeration (PTR) which acts as a precooler to (ii) the dilution refrigeration subsystem. Both systems are closed-cycle refrigerators with helium gas as the refrigerant (a monotonic ideal gas with a low condensation temperature). The working principles will be briefly presented next, and an in-depth discussion can be found in Ref[65].

4.1.1 Pulsed tube refrigerator

The PTR relies on the theory of oscillatory compression and expansion of an ideal gas, typically ^{4}He, within a closed volume at pressures varying from 10 to 30 bar. A simplified schematic of a single-stage orifice pulse tube refrigerator (OPTR) is shown in Fig. 4.1(a). The system consists of: (i) a compressor that periodically pressurizes/depressurizes the gas; (ii) heat exchangers (X1, X2, X3) that exchange heat with the environment/device; (iii) a regenerator made of a porous medium with a large heat capacity, acting as a heat reservoir (heat capacitor); (iv) a pulse tube where the gas is pushed and pulled; (v) an orifice that controls the flow resistance; and (vi) a buffer acting as a gas tank with practically constant pressure. An attractive feature of PTR, unlike Stirling or Gifford–McMahon refrigerators, is the absence of any moving parts at its cold end (typically due to the displacer). This significantly reduces vibrations on the connected experiment and enhances reliability. The typical vibration of PTR is in the order of 5–10 µm, much lower than 50–100 µm for a Gifford–McMahon refrigerator. The operation of the pulse tube depends on a regenerative cycle, but the nature of this cycle and the mechanism of heat pumping are challenging to explain due to thermoacoustic oscillation occurring in the tube. In other words, different elements of gas in the tube undergo different series of thermodynamic processes at any given time, and plotting macroscopic properties of the bulk gas is not possible (e.g., T-S or P-V curve). A qualitative explanation will be given, and more details can be found in Refs [66, 67].

First, the piston acts as a pressure wave generator, pressurizing/depressurizing the gas in the system cyclically. In the pressurizing phase, the gas enters the regenerator with a temperature of T_H and leaves the regenerator at a colder temperature, T_L, where the heat is transferred into the regenerator material. Additionally, the heat of compression on the compressor side is transferred by heat exchanger X_1 to the surroundings, typically via chilled water. At the pulse tube, about one-third of the gas flows through the orifice to the reservoir, giving a heat of compression, Q_0, through heat exchanger X_3. The oscillating gas that flows through the impedance or orifice separates the heating and cooling effects, and the function of the pulse tube is mostly to insulate the processes at its two ends. Around one-third of the gas in the middle portion of the pulse tube never leaves the tube and forms a temperature gradient that insulates the two ends (gas displacer). As a result, the pulse tube must be

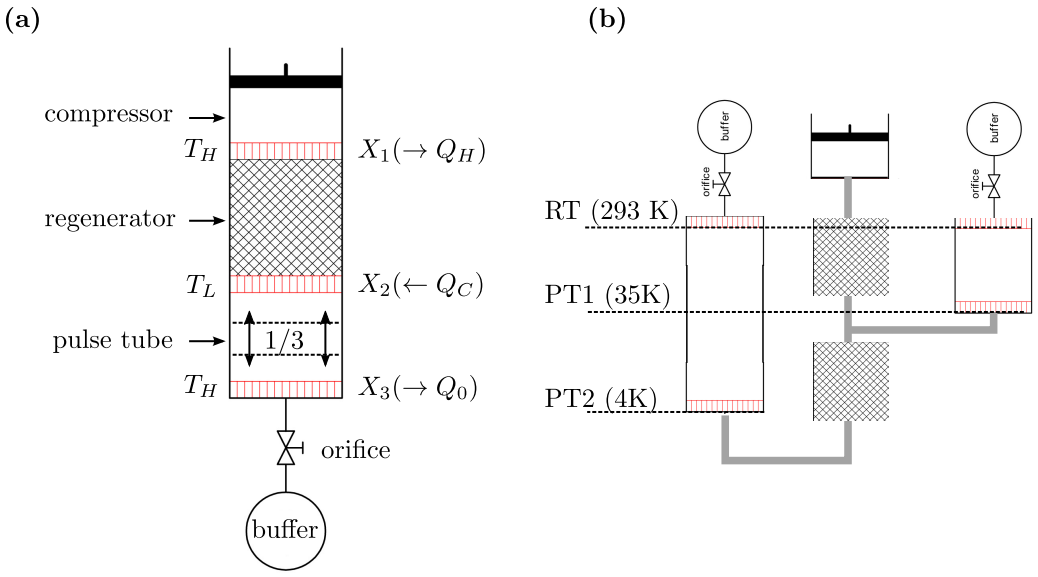

Figure 4.1: Pulse tube schematics reproduced from [68]: (a) single stage system, and (b) two-stage system.

large enough so that gas coming from the regenerator traverses only a portion of the pulse tube before the flow is reversed.

During the depressurizing phase, the gas in the pulse tube flows back to the generator with a temperature below T_L, providing the desired cooling power Q_C. The reason the temperature is less than T_L is due to the heat of compression dissipated by heat exchanger X_3 during the pressurizing phase (or, more accurately, the net enthalpy transfer from and to the pulse tube). Finally, the heat stored in the regenerator is transferred back into the gas, and the cycle repeats. For maximum cooling efficiency, high-efficiency regenerators and heat exchangers must be used. Additionally, the phase between the pressure wave generated by the compressor and the gas velocity in the tube has to be optimized, which can be done by adjusting the impedance to the buffer and the buffer size. Present pulse-tube coolers reach around 15–20 K as single-stage units and around 2 K as double-stage units. A two-stage parallel connection is shown in Fig. 4.1(b), which resembles the top three plates of a commercial DR. We use the PT415 cryocooler from Cryomech with a base temperature of 2.8K and a cooling capacity of 40 W at 45 K in the first stage, with 1.5 W at 4.2 K in the second stage.

4.1.2 ^{3}He–^{4}He dilution refrigerator

All dilution refrigerators rely on a stable cold environment at approximately 4 K. This can be simply achieved by the latent heat of evaporation of liquid ^{4}He with a boiling point of 4.2 K at atmospheric pressure. Reducing the pressure of ^{4}He allows 1.2 K temperatures, and using the ^{3}He isotope allows 0.25 K due to much higher vapor pressure. Modern dilution refrigerators deploy a 2-stage pulsed tube cryocooler, similar to the one discussed in the previous section, to create a 4 K environment. An illustrative schematic of the DR unit is shown in Fig. 4.2(a).

To explain the operation of the DR, we list first the main differences between ^{3}He and ^{4}He isotopes:

- ^{3}He has a lower latent heat of evaporation than ^{4}He and thus a higher vapor pressure. P_3/P_4 is 74 at 1 K but about 10^4 at 0.5 K. Additionally, the specific heat of ^{3}He is larger than the specific heat of ^{4}He, providing a larger cooling reservoir.

- Pure ^{4}He has a nuclear spin of $I = 0$, is a boson fluid, obeys Bose-Einstein statistics, and undergoes a superfluid transition at 2.17 K. Pure ^{3}He has a nuclear spin of $I = 1/2$, is a fermion fluid, obeys Fermi statistics, and doesn't show a superfluid transition until much lower temperatures when two fermions pair up and act as a boson, analogous to the formation of Cooper pairs (bosons) from two electrons (fermions).

- ^{3}He is a much rarer isotope and can be extracted from the by-products of certain nuclear reactions, making it much more expensive. A typical price of ^{3}He is about 150 $ per liter of liquid, whereas ^{4}He can be obtained commercially for about 6 $ per liter of liquid.

- The superfluid phase transition of liquid ^{4}He is depressed when we dilute the Bose liquid ^{4}He with the Fermi liquid ^{3}He, as shown by the phase transition diagram in Fig. 4.2(b). Upon further cooling, the mixture eventually separates into two immiscible phases, one rich in ^{4}He and the other rich in ^{3}He. Because of its lower density, the ^{3}He-rich liquid floats on top of the ^{4}He-rich liquid. If the temperature is decreased to near absolute zero, the ^{3}He-rich liquid becomes pure ^{3}He (concentrated phase), but surprisingly, the ^{3}He in the ^{4}He-rich phase approaches a constant concentration of 6.6%. This finite solubility is the key to the operation of the dilution refrigerator.

The enthalpy of ^{3}He in ^{4}He is higher than that for pure ^{3}He. This is because ^{3}He in ^{4}He behaves as a Fermi gas, and a gas has a higher enthalpy than a liquid. Analogous to evaporation cooling, if we can remove ^{3}He atoms from the diluted phase (^{3}He in ^{4}He), ^{3}He atoms from the concentrated phase will absorb energy from the surroundings and cross the phase boundary to occupy the vacant energy states (evaporate Fermi liquid to Fermi gas), causing a cooling power, as explained in [65].

$$\dot{Q} = \dot{n}_3(95T_{mc}^2 - 11T_{ex}^2) \tag{4.2}$$

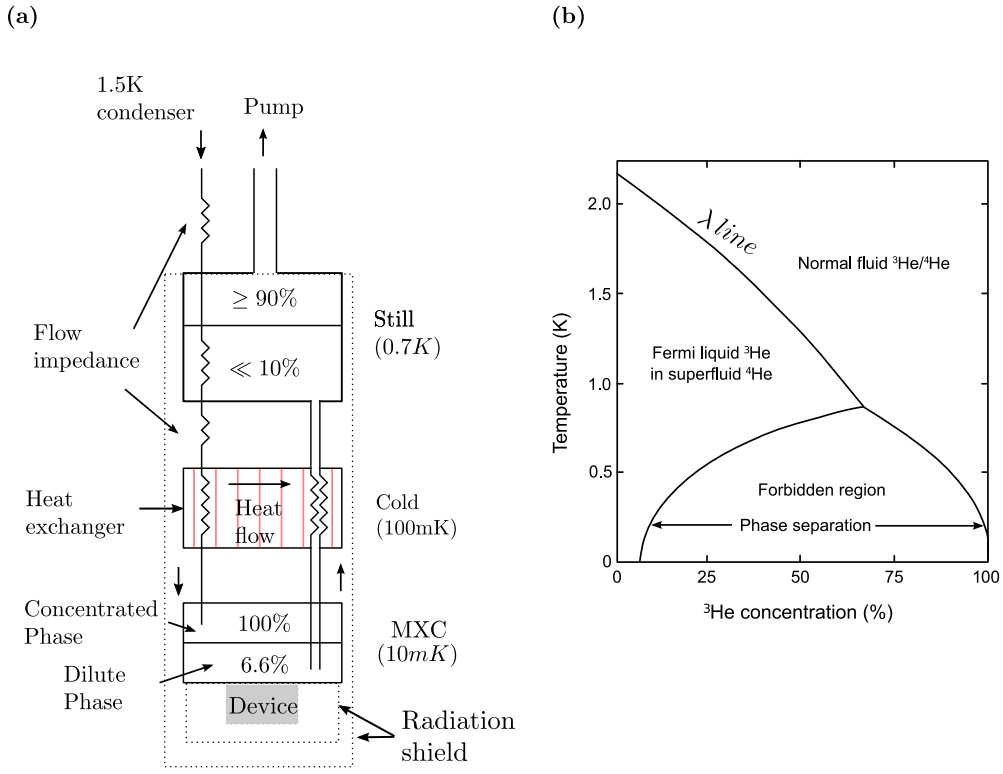

Figure 4.2: ^{3}He$-^4$He dilution refrigerator: (a) system schematic reproduced from [65] and (b) phase diagram as a function of temperature and ^{3}He concentration.

The ^{4}He component of a dilution refrigerator is effectively just a static background that facilitates the phase transition between ^{3}He fermi-liquid and ^{3}He fermi-gas. The difference between dilution refrigeration and evaporative cooling is the finite solubility of ^{3}He in ^{4}He. The lowest achievable temperature in an evaporator is limited by the exponentially decreasing vapor pressure ($\dot{Q} \propto \exp(-1/T)$). The effective vapor pressure in a dilution refrigerator (the concentration of ^{3}He in the Fermi gas) is constant with temperature ($\dot{Q} \propto T^2$), allowing access to much lower temperatures.

In order to selectively remove only ^{3}He from the diluted ^{4}He, the mixing chamber (MXC) is connected to a distiller ('still'), which is heated to around 0.7 K. The distiller distills the ^{3}He from the ^{4}He due to the difference in vapor pressure. The variance in ^{3}He concentration between the still and the mixing chamber results in an osmotic pressure gradient along the connecting tube that pulls ^{3}He from the mixing chamber. The extracted ^{3}He is then taken all the way to room temperature, cleaned with a liquid nitrogen trap, and recirculated back to the system, as illustrated in Fig. 4.2(a).

The complete circulation starts with ^{3}He entering the cryostat at a high pressure of a few hundred millibars. The ^{3}He is precooled to 60 K by the first-stage pulsed tube, then to 4 K by the 2nd stage pulsed tube, and further to 1.2–1.5 K by a vacuum-pumped ^{4}He bath (decreasing the pressure of the helium reservoir depresses its boiling point below 4.2 K). The liquefied ^{3}He is then cooled further through a combination of heat exchangers with the liquid dilute phase and the Joule Thompson expansion happening in the flow impedance to 700 mK. Subsequently, the ^{3}He flows through a secondary impedance and heat exchangers, being cooled by the returning ^{3}He gas. Finally, the pure ^{3}He enters the mixing chamber, the coldest area of the system, where a dilution process takes place, cooling the stage down to 10 mK.

4.1.3 Device shielding

Besides cooling the sample, the DR system should suppress electromagnetic noise and quasiparticle generation sources that cause qubit relaxation and dephasing. There is a wide range of techniques used to shield a device from static and dynamic electromagnetic fields, and readers seeking in-depth information on the topic are referred to Ref [69].

Radiation shield

A significant decoherence mechanism is the presence of quasiparticles (broken Cooper pairs) that take the qubit out of thermal equilibrium. One common source of energy to break a Cooper pair is stray infrared light, which contains photons with energy $\hbar\omega > 2\Delta$, where Δ is the superconducting energy gap. The quality factor for a resonator with frequency f_r is inversely proportional to the quasiparticle density n_{qp}, as discussed in [70].

$$\frac{1}{Q} = \frac{\alpha}{\pi}\sqrt{\frac{2\Delta}{hf_r}}\frac{n_{qp}}{D(E_F)\Delta} \tag{4.3}$$

with $D(E_F)$ being the two-spin density of states and α representing the kinetic inductance. Unlike large gap superconductors (e.g., Nb, TiN), Aluminum has a small superconducting gap ($\Delta/\hbar$ =88 GHz) with a long quasiparticle recombination time (2 ms). For stray light with power P and energy $hf > 2\Delta$, the rate equation of the total number of quasiparticles is:

$$\frac{\delta N_{qp}}{\delta t} = \frac{P}{\Delta} + G - RN_{qp} \tag{4.4}$$

Without stray light ($P = 0$), the quasiparticle density due to the sample black-body radiation is $n_{qp} = D(E_F)\sqrt{2\pi k_B T\Delta}\exp(-\Delta/k_B T)$, and the quality factor of the Al resonator is inversely proportional to the temperature. Approximately, for a 10^6 quality factor of an Al resonator, thermal excitation can be suppressed beyond recognition if the device is cooled below 100 mK. However, under strong infrared (IR) radiation, $n_{qp} \propto \sqrt{P/\Delta}$, and therefore,

96% of the black-body radiation from the 4.2 K stage can be absorbed by the sample, causing significant loss.

Successive layers of radiation shielding can minimize this effect. The first shielding layer is the electromagnetic (EM) cavity described in section 3.2.1, emphasizing the need for nearly light-tight mounting. In addition, the LD250 is equipped with an Au-Sn-plated copper shield mounted to the MXC plate at 100 mK and an Au-plated copper shield mounted to the still plate at 700 mK, as illustrated in Fig. 4.2(a). Infrared-absorbing epoxy can also be used to enhance the IR shielding [71].

Magnetic shield

The copper radiation shields discussed previously don't block static or slowly varying magnetic fields, which might have detrimental effects on superconducting qubits for the following reasons:

- Aluminum is a type-1 superconductor, and superconductivity is abruptly destroyed via a first-order phase transition when the strength of the applied magnetic field rises above a critical value $H > H_c$.
- Even at $H < H_c$, superconducting vortices do form in thin-film type-I superconductors. Besides adding flux-pinning sites in the ground plane (see section 3.1.6), a reduction in the global magnetic field suppresses vortex depinning.
- Slowly varying magnetic fields due to large moving objects can cause the tunable SQUID qubit to dephase over time. For example, the Earth's magnetic field is approximately 50 µT, and the tunable transmon used in this work has a SQUID area of 300 µm^2. This means that the presence of the Earth's magnetic field will add $7.5\Phi_0$ flux and shift the qubit frequency by around 2 GHz from the 4 GHz tuning range. However, fluctuations in the field (not its average) are what cause qubit dephasing. An estimation of the dephasing rate due to two-sided flux noise spectral density $S_\Phi(\omega)$, which typically scales as $1/f^\alpha$ in a tunable transmon, can be obtained perturbatively [72]:

$$\Gamma_\Phi = \frac{1}{2}(\frac{\partial\omega}{\partial\phi})^2 S_\phi(\omega) \tag{4.5}$$

The first stage of magnetic shielding can be achieved by using Aluminum as the material for the device cavity box, as discussed in section 3.2.1. When Al superconducts, the Meissner state acts as a strong diamagnet, repelling the magnetic field from its interior. A similar shielding mechanism is accomplished via the Au-Sn-plated Cu can that is mounted to the MXC plate (Sn is the superconductor). However, the most effective method we are using is a dual-cylinder made from Cryo-Netic material. Cryo-Netic is a ferromagnetic shield made from a nickel-iron alloy followed by heat treatment. It has an average $\mu_r = 70000$ and a saturation level of 7000 G. A COMSOL simulation was performed to optimize the

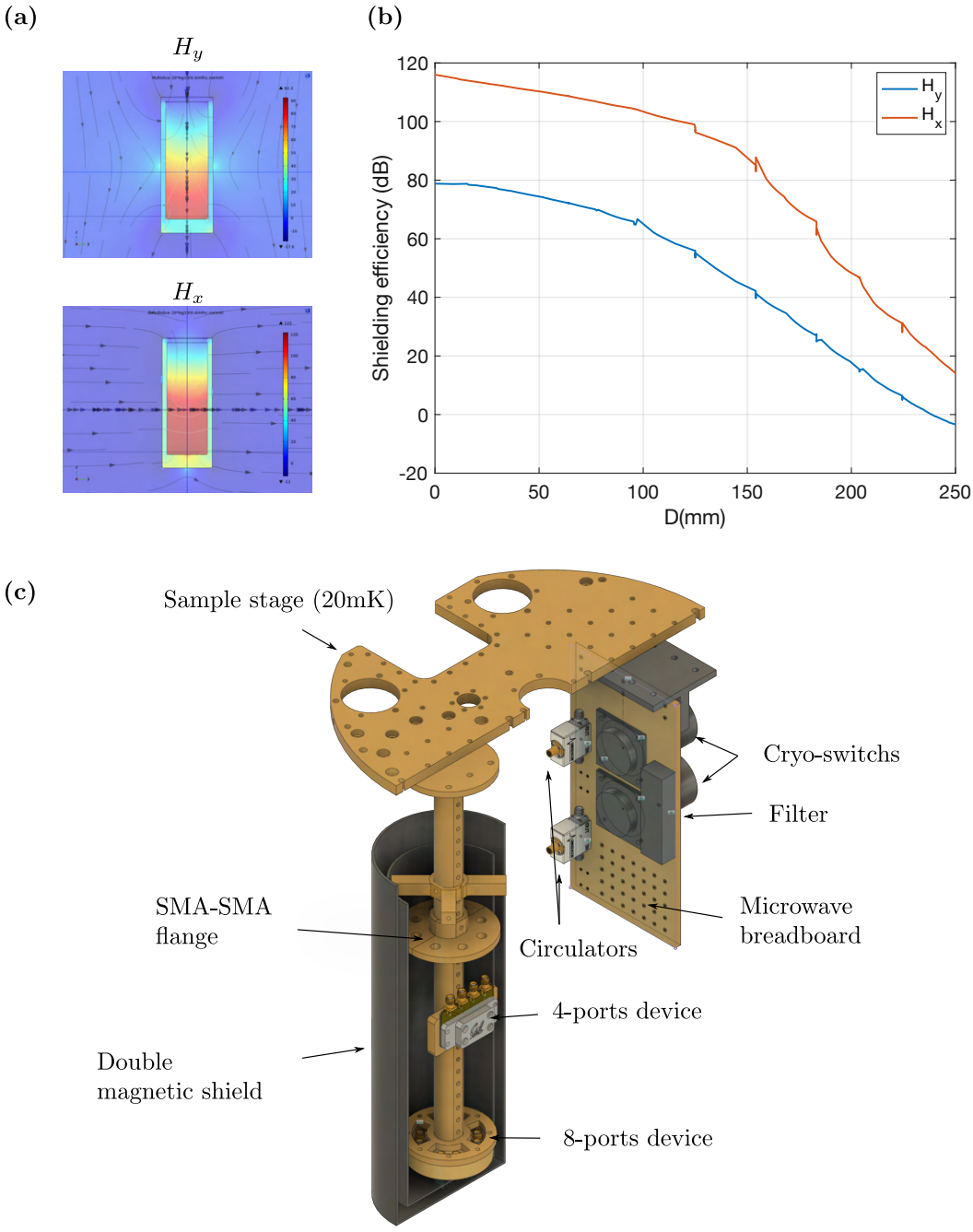

Figure 4.3: Magnetic shielding and stage design: (a) cross-section of the simulated static magnetic field due to external horizontal H_x and vertical source field H_y,(b) magnetic shielding efficiency η, and (c) CAD view of the designed sample stage.

geometry of the cylinder, as shown in Fig. 4.3(a) and (b). The higher the aspect ratio of the cylinder, the higher the isolation at its closed end. The used shield has an inner/outer length of 250 mm/290 mm, a radius of 45 mm/55 mm, and a thickness of 1.5 mm. The shielding efficiency (defined as $\eta = 20\log(H_{out}/H_{in})$) is around 120 dB for the horizontal field H_x and 80 dB for the vertical field H_y.

Sample stage design

We design the sample stage that is used to carry and position the packaged device deep inside the dual magnetic shield, as illustrated in Fig. 4.3(c). Additionally, a microwave breadboard is mounted to carry auxiliary microwave components such as mechanical switches, circulators, filters, etc. The parts are machined from high-purity oxygen-free copper, followed by gold-plating to prevent surface oxidation. Typically, tin is used for adhesion between gold and copper, but it is avoided here for its diamagnetic properties when it superconducts.

4.1.4 System wiring

As discussed in Section 4.1.3, multi-stage shields were used to protect the qubit from detrimental thermal noise and infrared (IR) radiation. Complete isolation is not possible due to the necessity of measurement. To interface with a single tunable qubit, we need four coaxial RF lines: readout resonators drive (Tx), readout resonator probe (Rx), qubit drive (XY), and qubit flux (Z), as depicted in Fig. 4.4(a). The coaxial RF lines serve as conduits for measurement signals as well as thermal noise from the outside environment, all the way to the heart of the quantum circuit. The objective is to preserve the measurement signals and suppress thermal noise as much as possible. An in-depth treatment of quantum noise can be found in Ref [73].

RF cables: thermal conduction of noise via cables from higher temperature stages to lower temperature stages should be suppressed by choosing cables with low thermal conductivity. However, poor thermal conductivity is often associated with poor electrical conductivity, leading to attenuation (except for superconductors). This attenuation is desirable for the Tx, XY, and Z lines, as the signals needed to control and read the qubit state are at the few-photon levels. We use UT-085-SS-SS stainless steel cables with a poor thermal conductivity of $0.5\,\mathrm{W\,K^{-1}\,m^{-1}}$ and an attenuation of $1\,\mathrm{dB\,m^{-1}}$ at 5 GHz. The signal returned by the qubit readout should be transferred with minimal losses until the first stage of amplification (HEMT at PT2). For the Rx line segment between the MXC (20 mK) and PT2 (4 K) stages, we use UT-085-NbTi niobium-titanium superconductor with a critical temperature T_C =10 K. In the superconducting regime, the NbTi cable has low thermal conductivity ($0.03\,\mathrm{W\,K^{-1}\,m^{-1}}$) and attenuation of $0.01\,\mathrm{dB\,m^{-1}}$ at 5 GHz.

RF Attenuators: the number of thermal photons due to black radiation at temperature T and frequency ω is given by the Bose-Einstein distribution $n_{\mathrm{BE}}(T,\omega) = 1/[\exp(\hbar\omega/k_BT)-1]$. At a typical qubit frequency, $n_{\mathrm{BE}}(T = 300\ \mathrm{K}) \approx 10^3$, whereas $n_{\mathrm{BE}}(T = 20\ \mathrm{mK}) \approx 10^{-7}$. Therefore, signal-to-thermal noise must be suppressed by more than 100 dB to reach the stage

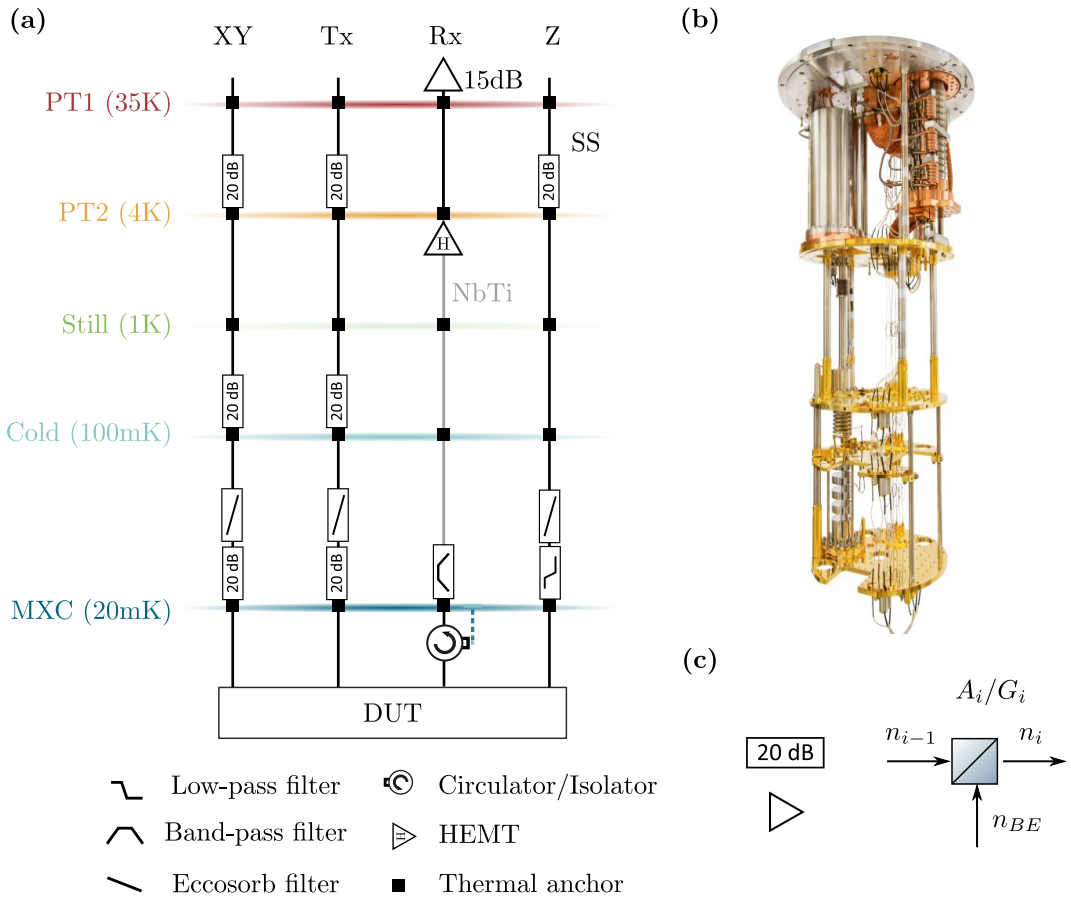

Figure 4.4: DR system wiring: (a) schematic of tunable qubit DR wiring; (b) picture of the installed LD250 DR system; and (c) beam splitter as a model of an attenuator/amplifier.

thermal limit, which is not practical due to the limited cooling power of the MXC stage. A typical value of 10^{-3} is usually used, requiring around $n_{\mathrm{BE}}(T = 300\ \mathrm{K})/10^{-3} = 60$ dB of attenuation per drive line. Attenuation is achieved through a resistor, and the resistor adds its own black body radiation to the signal (Johnson-Nyquist noise). Every attenuator with attenuation A_i is pictured as a fictitious beam splitter, as illustrated in Fig. 4.4(c), and the transmitted noise is given by[74]:

$$n_i(\omega) = \frac{n_{i-1}(\omega)}{A_i} + \frac{A_i - 1}{A_i} n_{BE}(T_i, \omega). \tag{4.6}$$

For example, an attenuator $A_i = 20$ dB $= 100$ passes 1% of the signal and 99% of the black-body radiation at temperature $n_{\mathrm{BE}}(T)$. It is evident that having all the attenuation at room temperature is ineffective. Also, having all the attenuation at the MXC stage is desirable but

not practical due to limited cooling power. Therefore, attenuators are typically distributed across the DR stages, with the key idea of not attenuating the noise by more than the noise added by the attenuator itself in the form of black body radiation. A rule of thumb is to balance the first and the second term of Eq. 4.6, which gives $A_i^{i-1} \approx n_{\mathrm{BE}}(T_{i-1})/n_{\mathrm{BE}}(T_i)$. Estimating the required attenuation, we have $A_{\mathrm{PT1}}^{\mathrm{RT}} \approx$6 dB (ignored), $A_{\mathrm{PT2}}^{\mathrm{RT}} \approx$20 dB, $A_{\mathrm{Still}}^{\mathrm{PT2}} \approx$6 dB (ignored), $A_{\mathrm{CP}}^{\mathrm{PT2}} \approx$23 dB, and $A_{\mathrm{MXC}}^{\mathrm{CP}} \approx$50 dB. The last value is large for the available cooling power and thus limited to 20 dB. This results in a noise floor $n_{\mathrm{BE}} = 10^{-3}$ at the MXC, corresponding to an effective temperature T_{eff} =42 mK. We can proceed to estimate the decoherence in the XY-line by calculating using Fermi Golden rule.

$$\Gamma_{\uparrow}^{XY} = g^2 S_V(\omega_q) \tag{4.7}$$

Here, $g \approx 2\pi \times 445$ GHz is the vacuum Rabi frequency for our qubit, as given by Eq. 2.26, and the voltage two-sided noise power spectral density is $S_V^{th}(T,\omega) = 2\hbar\omega n_{BE} R \approx 0.4\,(\mathrm{pV})^2/\mathrm{Hz}$. This results in $T_1 \approx 2$ s, which is much larger than what can be attained in practice and is typically limited by other factors.

For the Z-line, a larger current is typically required, and therefore, we added only 20 dB attenuation at the 4 K stage. We can proceed to calculate the dephasing, which is linked to the two-sided current noise power spectral density $S_I^{th}(T,\omega) = 2\hbar\omega n_{BE}/R$ as described in [75]:

$$\Gamma_2^Z = \frac{1}{2}(\frac{\partial\omega}{\partial I})^2 S_I(\omega_q) = \frac{1}{2}(M\frac{\partial\omega}{\partial\Phi})^2 S_I(\omega_q) \tag{4.8}$$

For mutual inductance $M = 2$ pH, and assuming a linear tuning slope of $\Delta\omega/\Delta\Phi \approx 3\,\mathrm{GHz}/\Phi_0$, and $n_B(4\,\mathrm{K})$ noise through a 20 dB attenuator resulting in $S_I^{\mathrm{th}}(T = 4\ \mathrm{K}) \approx 3\,(\mathrm{pA})^2/\mathrm{Hz}$, we get an estimate of $T_2^* \approx 400$ ms, a time much larger than what can typically be attained and is often limited by other noise factors. Therefore, the current noise at 4 K level is acceptable, and $A_{\mathrm{PT2}}^{\mathrm{RT}} \approx 20$ dB is installed at the PT2 (4 K) stage. A cryo-compatible attenuator from RFMW Ltd was used, and the distribution of the attenuator is shown in Fig. 4.4(a).To put the values into scale, we compare the voltage (current) fluctuations for the XY (Z) line at room temperature and at the MXC plate after attenuation. In the classical high-temperature limit where $\hbar\omega \ll k_B T$, the Bose-Einstein distribution gives the Rayleigh–Jeans law $n_{\mathrm{BE}} = k_B T/\hbar\omega$. The Johnson-Nyquist noise at room temperature is thus $S_V^{\mathrm{th}}(T = 295\ \mathrm{K}) = 2k_B T R \approx 0.5\,(\mathrm{nV})^2/\mathrm{Hz}$ and $S_I^{\mathrm{th}}(T = 295\ \mathrm{K}) = 2k_B T/R \approx 150\,(\mathrm{pA})^2/\mathrm{Hz}$. The addition of 60 dB attenuation has suppressed the room temperature noise to $0.4\,(\mathrm{pV})^2/\mathrm{Hz}$ and $3\,(\mathrm{pA})^2/\mathrm{Hz}$, respectively.

Amplifers/isolators: the Rx line carries only a few photons from the readout resonator and phase-preserving amplification (equal quadrature gain) is necessary. However, there must be noises added by the process, as an amplification without added noise would violate the Heisenberg uncertainty principle. An amplifier is a time-reversed attenuator, or a negative resistance, and can be similarly modeled (with a little caution) by a fictitious beam splitter. Similar to Eq. 4.6 and replacing A_i by $1/G_i$, we have:

$$n_i(\omega) = G_i n_{i-1}(\omega) + (G_i - 1) n_{amp}(T_i, \omega) \tag{4.9}$$

For example, a $G_i = 100 = 20dB$ amplifier will amplifiy signal noise n_{i-1} by a factor of 100 whereas add and multiply its own noise n_{amp} by a factor 99. Analogs to the attenuator, we proceed with balancing the two terms of Eq. 4.9 to obtain the optimal value for the gain is $G_i \approx n_{amp}/(n_{amp} - n_{i-1})$. The signal coming from the qubit has a very low noise $n_{MXC} \approx 10^{-7}$, therefore, the first stage amplifier should have the lowest noise possible n_{amp}. We use high-electron mobility transistor (HEMT) amplifier (LNF-LNC4_8C) with a 42 dB gain over 4–8 GHz and a noise temperature of 1.5 K, thus mounted at the PT2 stage (4 K). Around 44 dB of isolation towards the sample is provided by a 2-circulator (2 x LNF-CIC4_8A) in series, thermalized at MXC stage, and used to protect the qubit from any HEMT backactions. A common amplification scheme is to use Traveling Wave Josephson Parametric Amplifiers (TWPA) that provide near-quantum limited amplification before the HEMT [76].

Filters: in the Rx line, a reflective bandpass filter (Keenlion KBF-4/8-2S) with less than 1 dB insertion loss is installed at the MXC stage after the isolators and before the HEMT to suppress noise at frequencies outside the working bandwidth (4–8 GHz). In the Z-line, the bandwidth of typical flux pulses is at most 1 GHz, allowing to set the qubit frequency in a few nanoseconds. We install a 1.3 GHz lowpass filter (Minicircuits VLFX-1300+) at the MXC stage to suppress thermal noise at qubit frequencies. We added Eccosorb IR filters (QMC-CRYOIRF-002MF-S) on all the drive lines (Tx, XY, Z), which help in further suppressing IR radiation with minimal insertion loss. This is because typical commercial microwave filters don't work well beyond 20 GHz, and customized filters are required.

4.2 Measurement hardware

4.2.1 Readout chain (Tx, Rx)

Depending on whether the qubit is in the $|g\rangle$ or $|e\rangle$ state, the readout resonator undergoes a dispersive shift by a frequency $\omega_r \pm \chi$, as described by the dispersive Hamiltonian in Eq. 2.34, representing a quantum nondemolition measurement. In this scenario, driving the cavity results in a qubit-state-dependent coherent state. This state can be linked through a series of transformations along the connecting line to the quadrature of a scattered microwave field $[\hat{V}_i, \hat{V}_Q]$ around ω_r. Given that the resonator frequency typically falls within the 6–8 GHz range, the $[\hat{V}_i, \hat{V}_Q]$ quadrature can be measured through double heterodyning, as illustrated in Fig. 4.5(a).

The first heterodyning stage is digitally processed using the Zynq UltraScale+ RFSoC - a centaur chip featuring a Processor Subsystem (PS) and Programmable Logic (PL) unit. The PL unit comprises 12-bit 4GSPS RF-ADCs (x8), 14-bit 6.5GSPS RF-DACs (x8), and 60.5 Mb FPGA fabric. We use the QICK (Quantum Instrumentation Control Kit) FPGA overlay, specifically designed for superconducting quantum qubit applications [77]. The overlay integrates signal generator blocks for driving the DACs and readout blocks for driving the ADCs. Both blocks incorporate direct memory access (DMA) for signal storage and are controlled

by a virtual timed processor (tProc) that ensure synchronous signaling and acquisition. The signal generator block combines a 384 MHz bandwidth IQ envelope (2.6 ns time-resolution) with a fast direct digital synthesizer (DDS) operating at up to 6 GHz sampling frequency. The resulting 3 GHz signal falls within the first Nyquist zone of the 6.5GSPS DAC. The DDS block is configured to run continuously in the background to maintain phase coherence between different control pulses. The DDS mixer is inherently balanced, eliminating the need for typical analog IQ mixer calibration. The received signal undergoes down-conversion using the same DDS unit, followed by digital low-pass filtering, decimation, averaging, and storage for subsequent analysis. The round-trip latency for the entire chain is approximately 120 ns. This enables rapid interactive feedback and facilitates Feedforward protocols such as active-reset and error correction [78].

The second heterodyning stage employs an external local oscillator (LO) (LMX2595) set at a frequency of 8.5 GHz. Mixers (DM0412LW2) are then utilized to upconvert the intermediate frequency (IF) signal from the RFSoC to a higher frequency (RF) in a phase-preserving fashion, denoted as $\omega_{LO} \pm \omega_{IF}$. The LO power for mixing is adjusted using 10 dB amplifiers (picosecond 5828), a low-pass filter (MC VLFX-2500+) is employed to eliminate spurious DAC noises in the IF before mixing, and a bandpass filter (MC VLF-7200+ and MC VHF-4400+) is used to isolate the left sideband ($\omega_{LO} - \omega_{IF}$) after mixing. This results in a real-time bandwidth from 5.5–8 GHz. A symmetric chain is implemented on the down-conversion side before ADC sampling.

As discussed in Section 2.1.6, the number of cavity photons needed to operate in the dispersive regime must be much lower than $n \ll n_{critc} \approx (\Delta/2g)^2$ (around 1-10 microwave photons). This translates to an input power of $P = \langle n \rangle \hbar\omega\kappa_e \approx -130$ dBm in the microwave bus, using Eq. 2.61. Accounting for -60 dB attenuation in the DR system and -30 dBm generated signal, we added -40 dB (x2 MC FW-20+) attenuators to exploit the full DAC range. The receiver signal undergoes low-noise 40 dB amplification (2x MC ZX60-83LN-S+) to adjust the signal level for ADC sampling.

4.2.2 Qubit control chains (XY, Z)

The XY-line utilizes the same double heterodyning chain as the Tx-line, except for the filter choice, attenuation, and the LO frequency, as illustrated in Fig. 4.5(b). The LO (LMX2595) is set at 8 GHz with a 10 dB amplifier (picosecond 5828) before the mixer (MC ZX05-153LH-S+). The IF signal is first low-pass filtered (Mini-Circuits VLFX-2500+) and then amplified by 17 dB to improve the net RF-LO isolation (MC ZX60-123LN-S+0). The mixed RF signal undergoes a tight bandpass filter (MC VLF-6000+ and MC VHF-5050+), resulting in a real-time bandwidth of 5–7.5 GHz. The attenuation required at the end of the chain can be inferred from the 60 aF capacitive coupling of the XY line to the transmon. The loss rate $\kappa_{xy} \approx 500$ Hz at $\omega_q = 6$ GHz, and the Rabi frequency for a $\tau = 100$ ns π pulse is $\Omega_0 = \pi/\tau \approx 2\pi \times 30$MHz. The required peak power $P_p = \hbar\omega_q\Omega_0^2/(4\kappa_{xy}) \approx -80$ dBm. Given an 80 dB attenuation in the DR system on a -10 dBm generated signal, we add only 1–5 dB (MC FW-xx) at the end of the chain. Finally, a direct continuous wave LO sweep from 0–

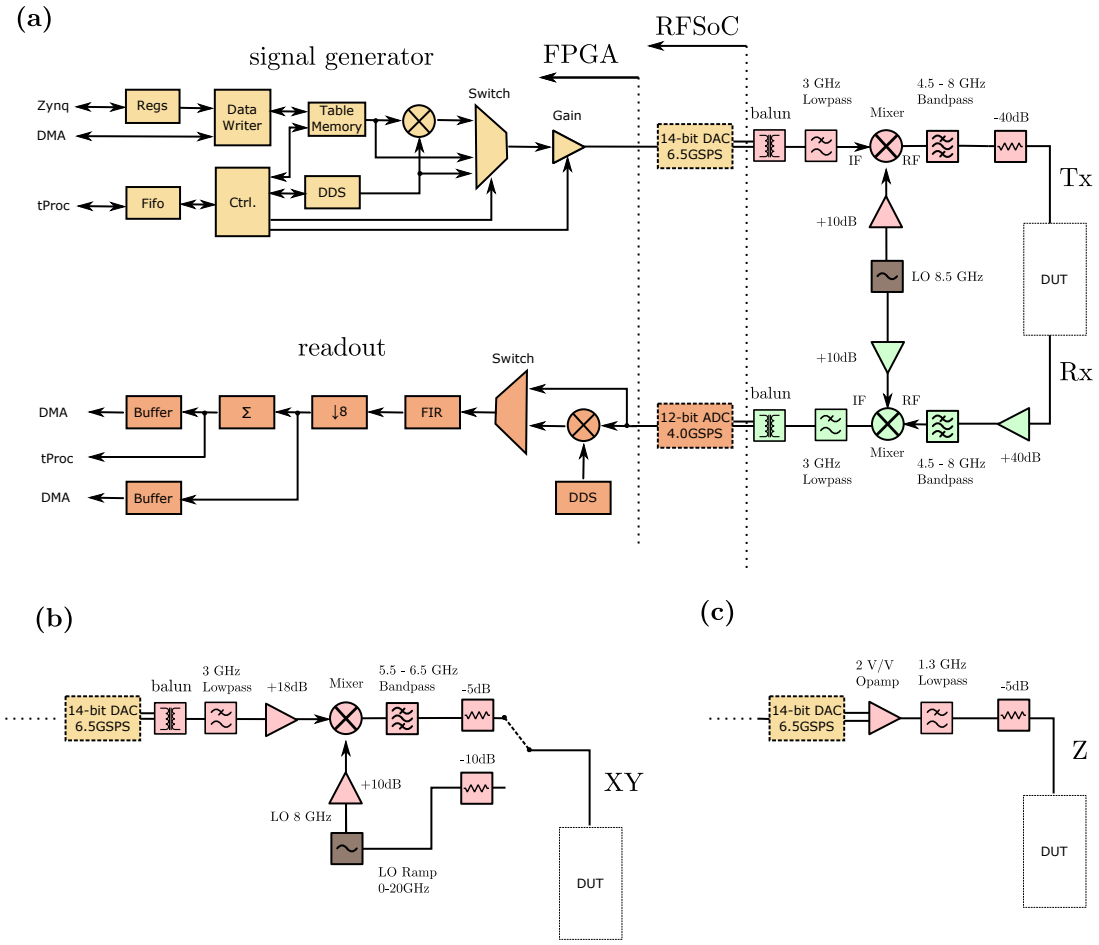

Figure 4.5: Measurement hardware: (a) double-heterodyning for the Tx/Rx readout loop, (b) double-heterodyning for the XY-line, and (c) direct pulse generation for the Z-line.

20 GHz was made available through another route for two-tone spectroscopy measurements, typically conducted over a bandwidth much larger than what can be mixed and filtered.

The differential DAC outputs for the XY and Tx lines were converted to single-ended outputs using high-frequency baluns (Mini-Circuits TCM2-33WX+) suitable for frequencies from 10–3000 MHz. However, for the Z-line, DC or near DC signals are required to park and stabilize the qubit at the desired frequency. Therefore, we used a DC to 800 MHz Differential-to-Single-Ended DAC Output Amplifier with a 5000 V μs^{-1} slew rate for fast qubit tuning (TI THS3217), followed by a 1.3 GHz low-pass filter (MC VLFX-1300), as shown in Fig. 4.5(c). For a SQUID mutual inductance $M = \phi_0/mA \approx 2\,\text{pH}$, we need to supply a current in the range of $\pm 0.5\,\text{mA}$ to induce a full flux quantum Φ_0. The amplifier produces a 100 mA on a

50 Ω termination and 10 mA after a 20 dB attenuator at the 4K stage in the DR. Therefore, only a small attenuation in the range of 2–10 dB is added on demand to maximize the Z-line resolution. The current will be slightly larger given the short termination of the Z-line at the transmon end.

4.2.3 Performance characterization

Heterodyning imperfections lead to the presence of unwanted signals at frequencies of ω_{LO} (LO leakage), $\omega_{LO}+\omega_{IF}$ (sideband leakage), ω_{IF} (IF leakage), and $nLO \pm mIF$ for integers n and m (mixer nonlinearity spurs). The impact of electronic noise on single-qubit operation is reviewed in detail in [79]. The filter choice for the XY and Tx lines has a 50 dB attenuation over a 2 GHz bandwidth, as illustrated in Fig. 4.6(a).

A second source of imperfection is the coherence of the system's master clock. Qubit phase coherence is measured relative to the rotating frame defined by the master clock of the measuring apparatus. Therefore, any instability of the rotating frame (coordinate system) can be interpreted as a phase decoherence in the transmon itself. The measured LO phase noise is plotted in Fig. 4.6(b) and is around -90 dBc/Hz. The relationship between LO phase noise to the phase decoherence is given by [80]

$$\Gamma_2^{LO} = \frac{1}{2}\omega^2 S_\Phi(\omega) \tag{4.10}$$

which leads to $T_2 \approx 31$ s, and therefore does not limit our measurements.

Finally, we characterize the speed of our Z-line pulse with a capacitive load from a 20 dB attenuators and 2 m-length coaxial cable. The average rise and fall time is approximately 5 ns, which allow traversing a 3 GHz qubit frequency, as shown in Fig. 4.6(c). This aspect is crucial for minimizing Landau–Zener (LZ) transitions with TLSs along the qubit path. The probability for the qubit to transition its excitation to the TLS is given by [81]. The final assembled Xilinx FPGA and microwave mixing front end can fit into a small enclosure, as shown in Fig. 4.6(d).

4.3 Tunable transmon calibration

The ultimate goal of calibrating a qubit is to perform high-fidelity single-qubit gates along with accurate discriminating measurements of the $|g\rangle$ and $|e\rangle$ states. In this section, we will present the required calibration sequence for a tunable transmon, which is necessary before measuring and operating the device. Additionally, we will use the information obtained to infer the fabricated qubit circuit parameters and compare them with the designed values, serving as a feedback for process control .

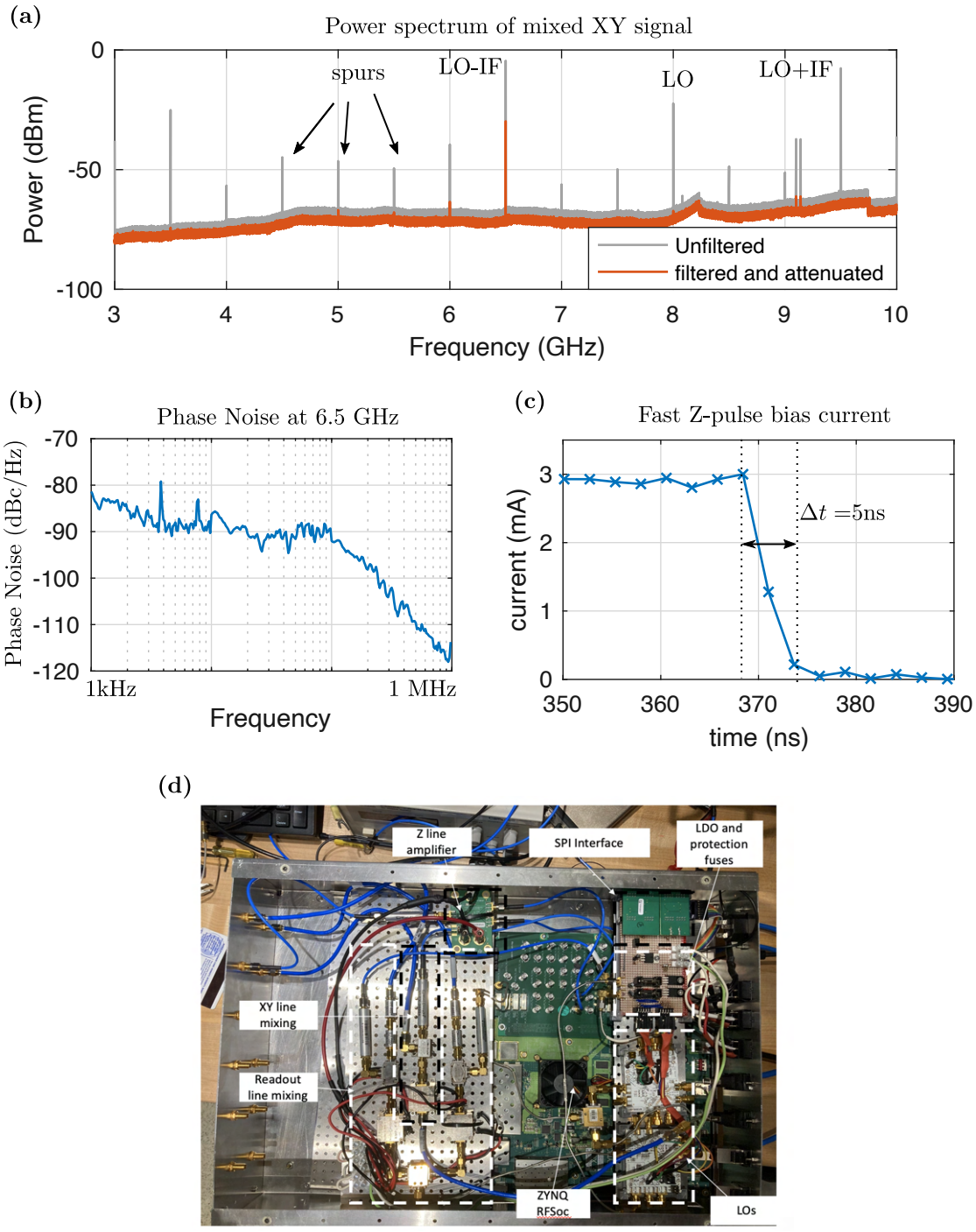

Figure 4.6: Room Temperature microwave characterization: (a) power spectrum scan of the XY line with and without filters, (b) local oscillator phase noise, (c) Z-line rise/fall time, and (d) image of the assembled FPGA measurement hardware.

4.3.1 Calibration sequences

Detailed discussions of full single and two-qubit calibration sequences can be found in Refs. [77, 82, 83, 84]. In the order of execution, the major steps in calibrating a single tunable transmon qubit are:

1. **Readout calibration:** identify the readout resonator frequency and configure a readout pulse amplitude and duration to ensure operating in the dispersive regime of the Jaynes–Cummings model. Additionally, ensure that the receiver is synchronous and phase-coherent with the transmitter for reliable measurement of the readout resonator quadratures.

2. **Qubit calibration:** perform calibration sequences on the qubit to determine its frequency at the flux-insensitive point, inharmonicity, dispersive shift, and the pulse information required to execute X_π and $X_{\pi/2}$ single-qubit gates.

3. **Pulses refinement:** revisit the frequency and amplitude choices of the readout resonator/qubit and perform pulse optimization based on single-shot readout measurements.

4. **Z-line calibration:** establish a map between the qubit frequency and the Z-line current, and estimate the pulse delay between the XY and Z-lines.

5. **Qubit state discrimination:** define a high-fidelity discriminator that classifies the readout quadrature measurement into $|g\rangle$ or $|e\rangle$ qubit states, then measure the thermal excited state populations of the qubit (p_{th}).

6. **Qubit coherence measurements:** we test our calibration with simple measurements of the relaxation time (T_1) and Ramsey dephasing time (T_2^*).

Readout calibration

The first task is to locate the readout resonance (ω_r), which can be rapidly done with a wide scan using a vector network analyzer (VNA). Once located, we proceed with pulse-based measurements using the FPGA hardware. As shown in Fig. 4.7(a), we first measure the time-of-flight (t_{TOF}) for the readout pulse and use it to trigger the receiver for acquisition. Next, we measure the group delay ($\tau_g = -\partial\phi/\omega$) through a high-resolution scan over a small frequency range, which helps unwrap the accumulated propagation phase in the cables and simplifies the fitting process ($\bar{S}_{21} = e^{-i\omega\tau_g} S_{21}$). Finally, a spectroscopic scan of the resonance is performed and the data are fitted to the following complex Lorentzian model of a hanging resonator (a modified version of Eq. 2.64):

$$\bar{S}_{21} = a e^{-i\omega\tau_g} \frac{\kappa_i/2 - i\Delta}{(\kappa_i + |\kappa_e| e^{i\phi_0})/2 - i\Delta} \tag{4.11}$$

In practice, the observed Lorentzian line shape is asymmetric due to the asymmetric input and output impedance of the readout bus (fabrication imperfections, unequal wire bonds, etc). The asymmetry can be accounted for by allowing κ_e to be a complex value, where $|\kappa_e|$ has the physical meaning of the decay rate [60]. If we have perfectly balanced impedance, then $\phi_0 = 0$ and κ_e is real. We also note that for accurate fitting, the readout pulse duration should be much larger than the resonator linewidth ($\tau_r \gg 1/\kappa$).

In order to operate the resonator in the dispersive regime ($n \ll n_{\text{crit}} \approx (\Delta/2g)^2$), we perform a spectroscopic scan of the resonance while sweeping the readout amplitude. After a certain threshold, we observe a punch-out of the resonance (a frequency shift from the quantum limit to the classical limit) that is roughly equal to the Lamb shift $\Lambda = g^2/\Delta$, as depicted in Fig. 4.7(b). The 2D data can also be fitted to extract the resonance frequency ($\omega_r/2\pi$) and the internal/external quality factors, Q_i/Q_e using Eq. 4.11, as shown in Fig. 4.7(c) and (d) respectively. We notice that Q_e remains fixed as a function of power, whereas Q_i increases due to TLS saturation.

Qubit calibration

We turn our attention next to the tunable transmon and locate the flux-insensitive frequency (ω_q^{max}), which will serve as a reference point for subsequent calibrations and measurements. First, we perform readout spectroscopy while sweeping the SQUID flux via the Z-line, as shown in Fig. 4.8(a). Since the qubit frequency oscillates periodically every flux quantum Φ_0, so will the readout resonator by $\delta\omega_r \propto g^2/\Delta$. The maximum (minimum) qubit frequency $\omega_q^{max}(\omega_q^{min})$ can then be mapped to Z-line amplitude $A_z^{max}(A_z^{min})$. In theory, A_z^{max} should occur under zero Z-line current. However, due to stray magnetic fields, the flux-insensitive point is slightly offset. The results are plotted in Fig. 4.8(a) along with the frequency fit. To identify ω_q^{max}, we set the Z-line to A_z^{max} and perform two-tone spectroscopy. A probe tone of ω_r is sent to the resonator, and a pulse probe is sent to the qubit (via the XY-line) with swept values of the frequency and amplitude, as illustrated in Fig. 4.8(b). From the measured chevron pattern, we locate the qubit frequency $\omega_q^{max}/2\pi \approx$6.35 GHz and infer the inharmonicity by noting that the two-photon transition appears red-shifted by $E_c/2\hbar$ from the qubit frequency, resulting an inharmonicity of $\alpha/2\pi \approx E_c/\hbar \approx$180 MHz. The linewidth can be fitted to the following Lorentzian lineshape

$$P_e(\omega) = \frac{1}{2}\frac{\Omega_R^2}{\gamma_1\gamma_2 + \delta_q^2\gamma_1/\gamma_2 + \Omega_R^2} \tag{4.12}$$

with relaxation rate γ_1, dephasing rate γ_2, Rabi frequency Ω_R, and $\delta_q = (\omega_q + \chi) - \omega_d$ being the detuning between the Lamb-shifted qubit transition frequency and the drive frequency [20]. The line shape experiences power broadening and evolves from the bare qubit linewidth given by $2\gamma_2$ to $2\sqrt{1/T_2^2 + \Omega_R^2 T_1/T_2}$. The power broadening can be exploited to locate the qubit frequency faster and give a rough estimate of its coherence. Finally, the dispersive shift χ can be measured by observing the shift of the readout resonator with or without a

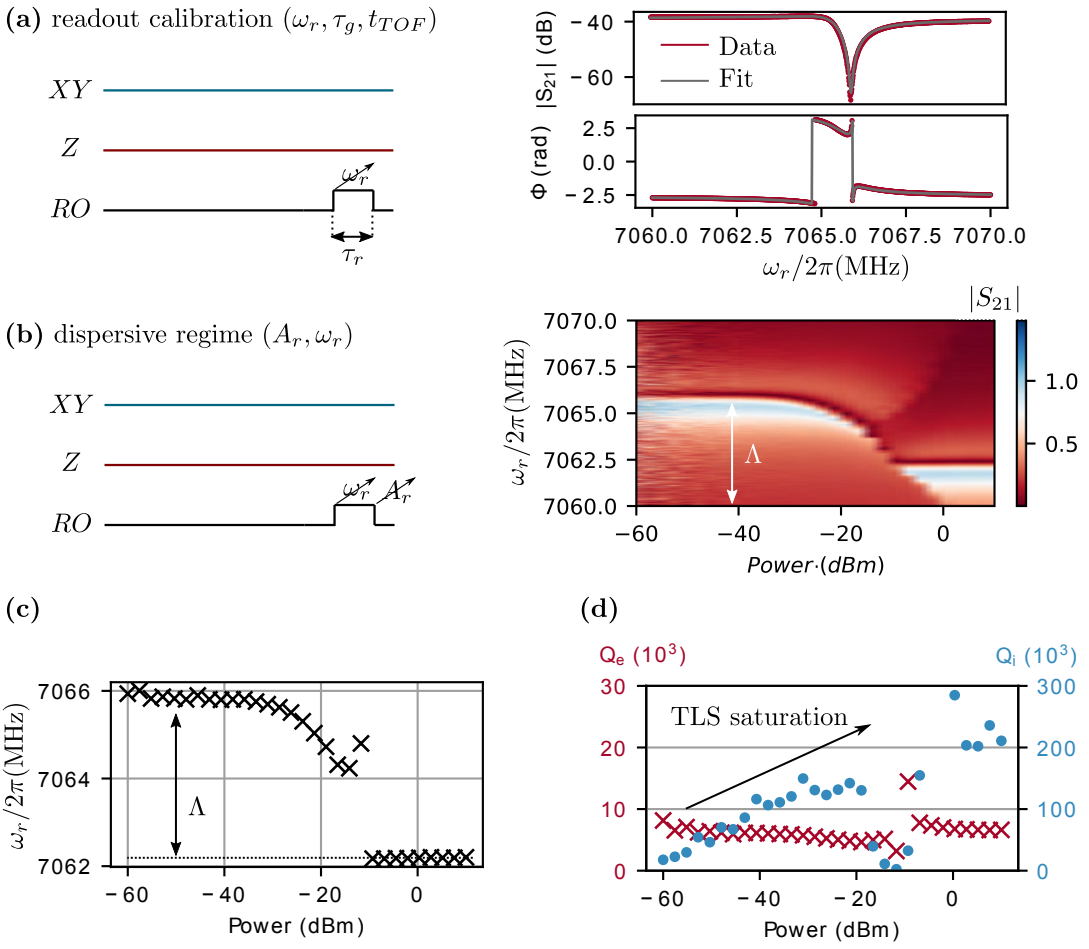

Figure 4.7: Readout calibration: (a) complex Lorentzian fitting of the readout resonance, (b) resonator spectroscopy as a function of power, where the fitted frequencies and quality factors are presented in (c) and (d), respectively.

continuous XY tone at ω_{xy}, which will set the qubit, on average, to a population of $p_q \approx 1/2$, as illustrated in Fig. 4.8(c).

Next, we sweep the XY pulse duration (τ_{xy}) for a fixed amplitude(A_{xy}) and frequency (ω_q^{max}) to observe a Rabi oscillation with an exponential decay, as shown in Fig. 4.9(a). We set $\tau_{xy}^{\pi} = 100\,\text{ns}$ for a fast qubit gate compared to the qubit lifetime/dephasing, yet long enough to avoid exciting high-order transmon states (much longer than the inharmonicity $h/\alpha \approx 5\,\text{ns}$). The amplitude is then swept, but this time with a Gaussian pulse of the following form

$$A_{xy}^{\pi}(t) = \frac{1}{2\pi\sigma^2} e^{-\frac{(t-\mu)^2}{\sigma^2}} \tag{4.13}$$

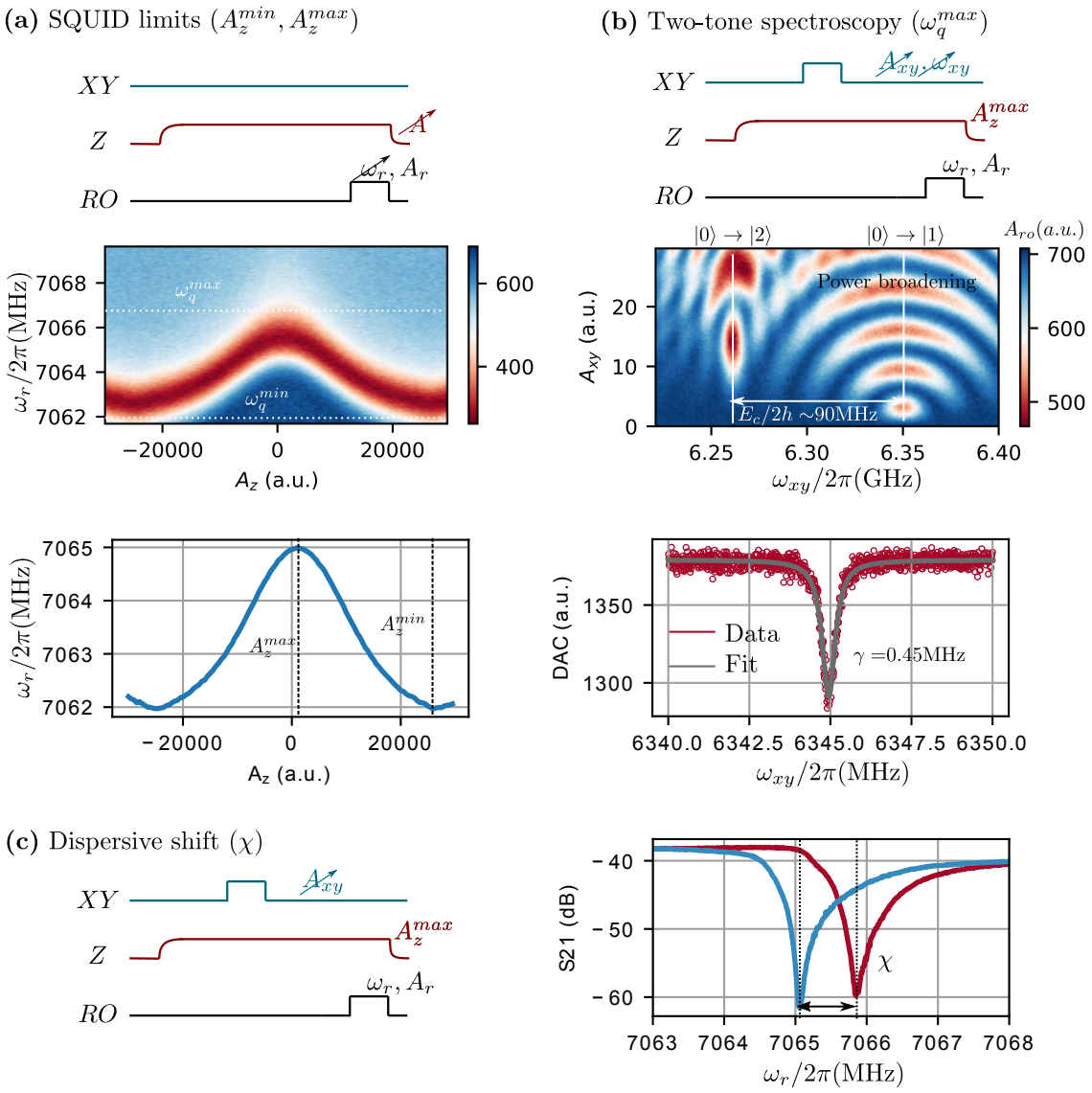

Figure 4.8: Qubit spectroscopy: (a) SQUID limits and tunability range, (b) two-tone spectroscopy, and (c) dispersive shift measurement.

with $\sigma = \tau_{xy}^{\pi}/4 = 25\,\text{ns}$, as shown in Fig. 4.9(b). Compared to a flat pulse, a Gaussian pulse reduces spectrum broadening that causes leakage to higher transmon states [85]. Assuming the readout amplitude is proportional to the excited state population (P_e), the measured Rabi oscillation is proportional to the mean readout signal and can thus be fitted to

$$P_e(A) = a \sin\left(\frac{\pi A}{2A_{xy}^{\pi}}\right) + b \tag{4.14}$$

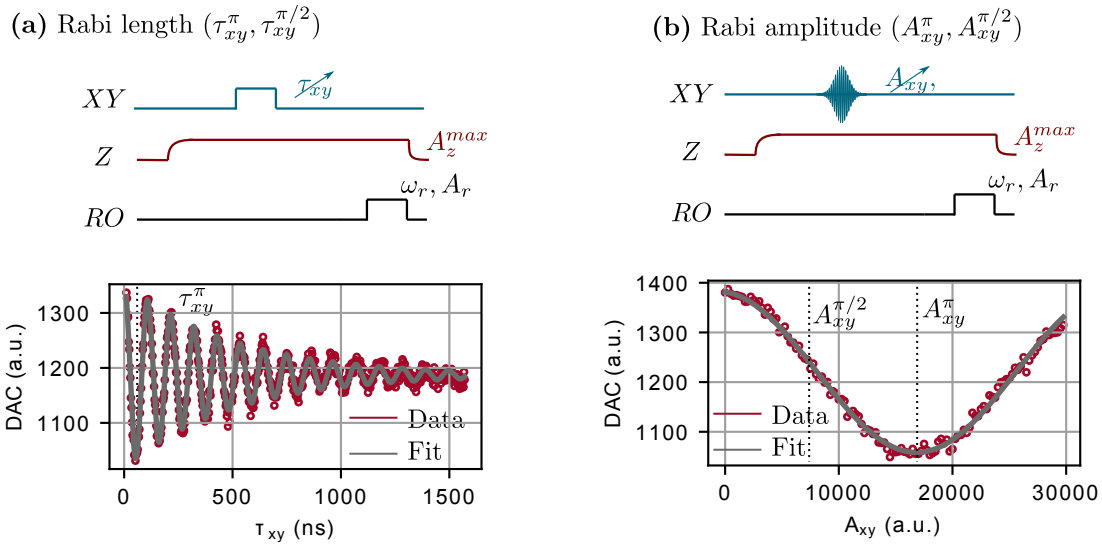

Figure 4.9: Qubit gate calibration and Rabi oscillations by sweeping: (a) the length of flat XY pulse, and (b) the amplitude of a Gaussian XY pulse.

Here, A_{xy}^{π} and $A_{xy}^{\pi/2}$ are the pulse amplitudes corresponding to X_{π} and $X_{\pi/2}$ rotations, respectively. With these rotations in hand, we can prepare the qubit in any arbitrary state.

Pulses refinement

Readout fidelity can be further enhanced by performing the following refinement step: the qubit is prepared in the $|g\rangle$ and $|e\rangle$ states, and the corresponding readout IQ shots are collected. We repeat the measurement N times for different readout frequencies (ω_r) and amplitudes (A_r) as illustrated in Fig. 4.10 (a) and (b), respectively. The goal is to maximize the signal-to-noise ratio (SNR), as defined in [20]:

$$\mathrm{SNR}^2 = \frac{|\mu_e - \mu_g|^2}{\sigma_e^2 + \sigma_g^2} \tag{4.15}$$

with a mean μ_x and standard deviation σ_x of state $|x\rangle$. We can observe from the plots that there is a better choice of readout frequency/amplitude that yields a higher SNR than the one chosen previously. This is because a few photons in the cavity result in poor SNR, whereas too many photons, even in the dispersive regime ($n \ll n_c$), lead to measurement-induced leakage and phase errors on the qubit [86].

Next, we refine the qubit drive frequency, which was determined previously via two-tone spectroscopy, which in practice s susceptible to systematic errors due to AC Stark shift. If our choice exactly matched the qubit frequency ω_q^{max}, then two consecutive $X_{\pi/2}$ pulses

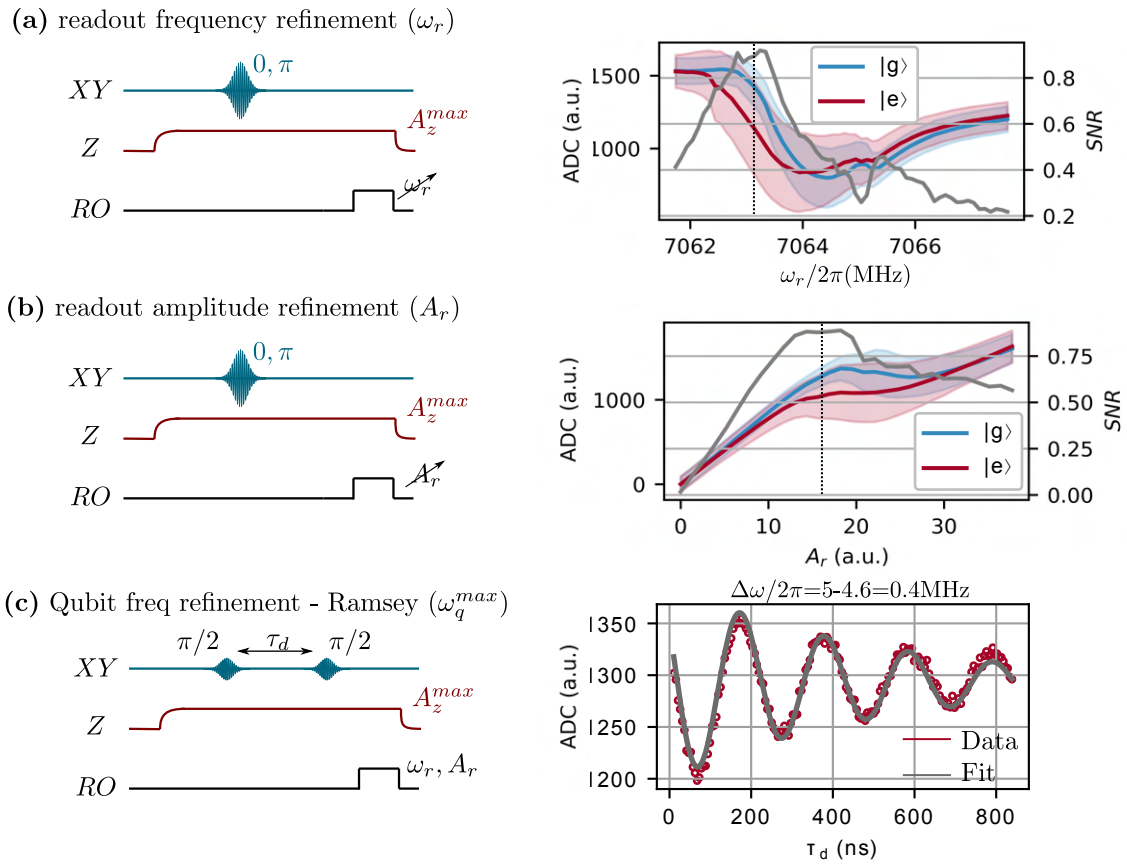

Figure 4.10: Pulse refinement: (a) readout frequency shots optimization, (b) readout amplitude shots optimization, and (c) qubit frequency optimization via Ramsey sequence.

separated by a time less than the dephasing should take the qubit from the $|g\rangle$ to the $|e\rangle$ state. This is because, in the rotating frame, the state will be stationary on the Bloch sphere. However, a slight detuning from the qubit frequency will cause the state to precess by $\delta\omega$, as given by Eq. 2.28. This effect can be used to precisely tune the frequency of our qubit drive. We intentionally offset the drive frequency by Δ and measure the qubit precession (δ) - known as Ramsey fringes - as illustrated in Fig. 4.10(c). The results can be fitted to a decaying sinusoid function:

$$P_e(\tau) = a\cos(\delta\tau_d + \theta)\exp(-\Gamma_\phi\tau) \tag{4.16}$$

where Γ_ϕ is the dephasing rate. The phase shift θ accounts for potential additional rotations caused by AC Stark shifts and by the Bloch vector precession starting already during the preparation pulse. The corrected qubit frequency is then $\omega_q = \omega_{\text{est}} + \Delta - \delta$. The intentional

upward shift in the qubit drive allows better curve fitting as well as discrimination between positive and negative frequency errors.

Z-line calibration

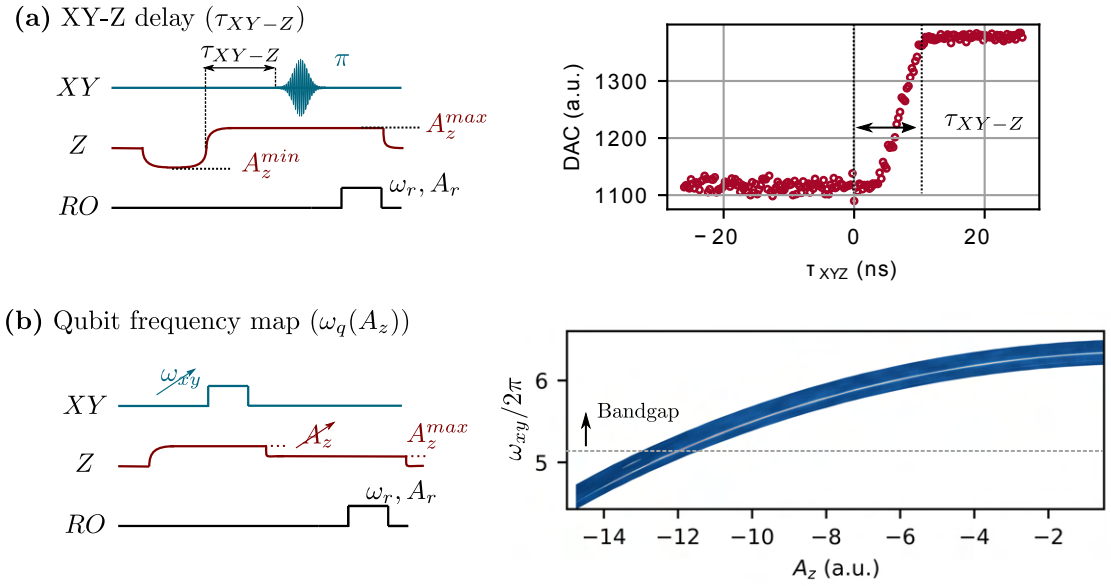

Figure 4.11: Z-line calibration (a) the delay between XY and Z lines and (b) the qubit frequency map as a function of Z-line amplitude.

It is important to estimate the delay difference between the Z and XY pulses, which typically arises due to differences in cable lengths and electronics. This is crucial to ensure that we perform and finish the qubit gate before moving it to another frequency. The delay is measured by bringing the qubit from a frequency far away from the reference point (ω_q^{max}) at time t_0. At a time of $t_0 + \tau_{xy}$, we fire an X_π pulse followed immediately by a readout measurement, as illustrated in Fig. 4.11(a). The minimum delay time is then determined to be $\tau_{XY-Z} \approx 10\,\text{ns}$, which is sufficient for the qubit to reach from a distant frequency, settle, and be fully excited by the X_π pulse.

To determine the map that links the qubit frequency to the Z-line amplitude, we perform a two-tone spectroscopy (fixed readout frequency and a fixed range of XY frequencies) while sweeping the Z-line amplitude A_z, as illustrated in Fig. 4.11(b). To accelerate the mapping, we scan adaptively by centering the XY-frequency range on the detected qubit frequency of the previous scan. Since the real-time bandwidth of the FPGA hardware is 3 GHz, we observe a split of the Lorentzian peak as we move from the 1st to the 2nd Nyquist zone, and weaker signals thereafter. The rest of the SQUID mapping can be extrapolated by fitting to

the following functional form

$$\omega_q(A_z) = a\sin(bA_z + \theta) + c \tag{4.17}$$

Alternatively, we can skip the mixer and filters in the XY chain and connect the local oscillator directly to the XY line, as shown in Fig. 4.5(b). This allows for a much wider (but slower) scan, ranging from 0–20 GHz.

Qubit state discrimination

To discriminate between the $|g\rangle$ and $|e\rangle$ states of the qubit, we perform shot measurements for each and plot the corresponding IQ data, as illustrated in Fig. 4.12(a). The blobs represent approximately two-dimensional Gaussian statistical distributions $[\hat{V}_i, \hat{V}_q]$, which can be theoretically traced through a series of transformations, including smearing and rotation to the coherent resonator drive, that itself depends on the qubit state. First, we determine the amount of phase ϕ_r needed to rotate the IQ coordinates so that the means (depicted

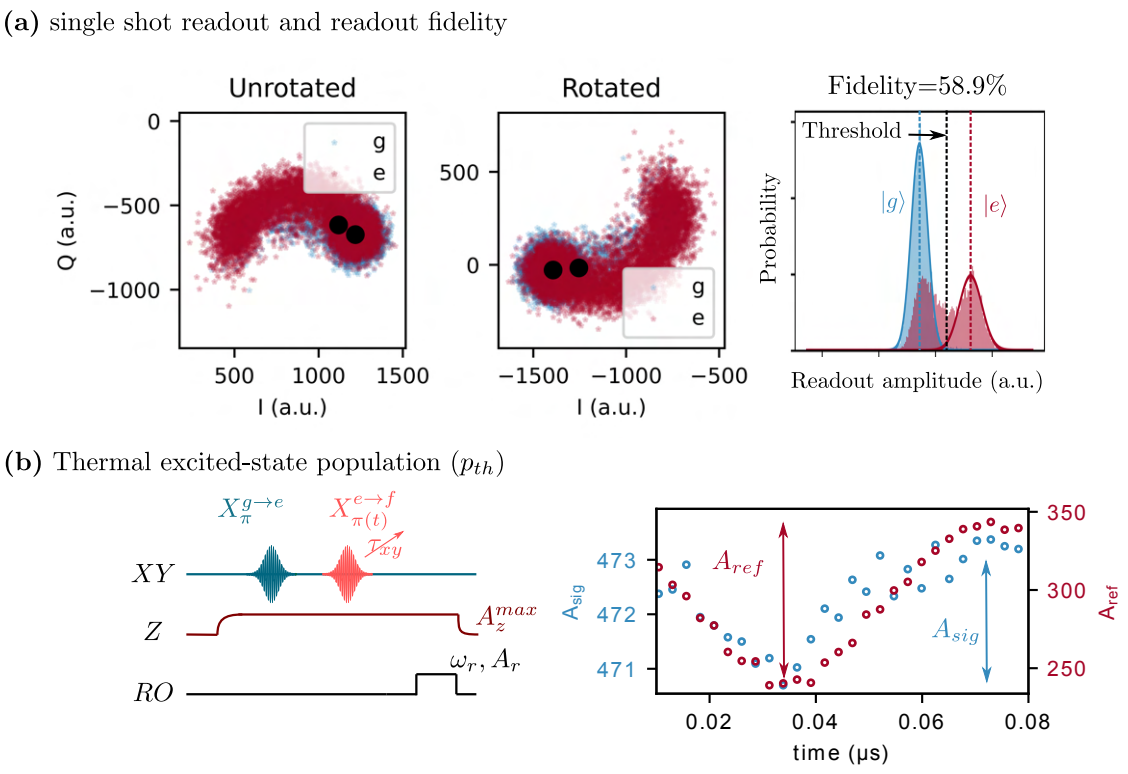

Figure 4.12: Qubit state calibration: (a) single-shot readout calibration, and (b) thermal/residual excited-state population measurement.

as black circles) of the blobs are aligned horizontally. Subsequently, the blobs are projected onto the I-axis, resulting in a clean 1D Gaussian distribution for the $|g\rangle$ state and double Gaussian peaks for the $|e\rangle$. The latter is due to the short qubit lifetime used in this study, causing the excited state to decay during the readout measurement pulse. The means of the 1D Gaussian distribution can be used to normalize the readout signal and map it to the qubit population. However, it's important to note that the value can exceed the [0,1] range, and the mapping is not linear at high readout power. Alternatively, the qubit state can be determined based on a logical condition that is more reflective of the quantum nature and is not a function of readout power. This can be done by calculating the threshold of the discriminator that bisects the I-axis and classifies the readout shots into $|g\rangle$ or $|e\rangle$ state with maximum fidelity. Measurement fidelity is defined as [20]

$$F_m = 1 - [P(e|g) + P(g|e)] \approx 1 - \mathrm{erfc}(\frac{\mathrm{SNR}}{2}) \tag{4.18}$$

here, $P(\sigma|\hat{\sigma})$ is the probability that a qubit in state $\hat{\sigma}$ was measured to be in state σ, and erfc is the complementary error function. Numerically, this can be computed by calculating the contrast of detection

$$C_j = \frac{\sum_{-\infty}^{j} g_i - \sum_{-\infty}^{j} e_i}{\sum_{-\infty}^{\infty} g_i/2 + \sum_{-\infty}^{\infty} e_i/2} \tag{4.19}$$

where g_i and e_i represent the number of measured shots for $|g\rangle$ and $|e\rangle$ in bin i. The detection threshold is then determined by $A_r^{thr} = \arg\max C_j$, and the fidelity is calculated as $F = \max C_j$. With these parameters in hand, all subsequent measurements can be expressed in terms of the qubit classified states ($|g\rangle$ and $|e\rangle$) instead of the projected IQ blobs.

Finally, in this work, it was important to calculate the thermally excited-state population of the qubit (p_{th}) that reflects the physical temperature of the device. However, this is not exactly the same as $P(e|g)$ as it includes read-out induced errors. To obtain an accurate estimate of p_{th}, we record the amplitudes $A_{\mathrm{ref}}(A_{\mathrm{sig}})$ of the $|e\rangle \rightarrow |f\rangle$ Rabi-oscillations with (without) a reference X_π pulse, as described in [87]. The pulse sequence and Rabi-oscillations are plotted in Fig. 4.12(b), and p_{th} can be calculated from

$$p_{th} \approx \frac{A_{sig}}{A_{ref} + A_{sig}}, \tag{4.20}$$

which is approximately 2.8% in our device and lower than the measured $P(e|g) \approx 8\%$ that is affected by readout fidelity.

Qubit coherence measurements

To measure the qubit relaxation time T_1 at frequency ω_q, we excite the qubit with an X_π pulse at the reference frequency ω_q^{max} where the calibration was performed. Next, the qubit is tuned and held at ω_q for a time τ_d, and then tuned back to ω_q^{max} for state measurement.

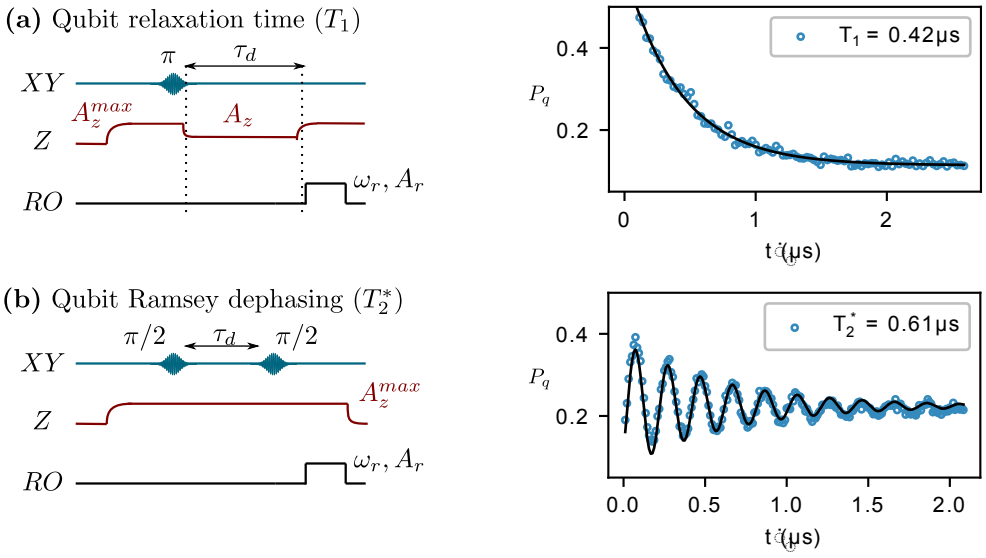

Figure 4.13: Qubit coherence measurements: (a) relaxation time T_1, and (b) Ramsey dephasing time T_2^*.

The pulse sequence and results are depicted in Fig. 4.13(a), and the data can be fitted to the following exponential form to extract the relaxation time T_1

$$P_e(\tau) = a\exp(-\tau/T_1) + b \tag{4.21}$$

The dephasing time T_2^* at ω_q^{max} can be measured using a Ramsey sequence (two $X_{\pi/2}$ pulses separated by τ_d). The pulse sequence and results are presented in Fig. 4.13(b), where the decaying sinusoid can be fitted to the following functional form

$$P_e(\tau) = a\cos(\delta\tau_d + \theta)\exp(-\tau/T_2^*) + b \tag{4.22}$$

We note that performing a swap exchange to measure T_2^* at other frequencies (as done for T_1) is challenging as the qubit will experience precision and accumulate a large phase that is practically intractable.

4.3.2 Parameters extraction summary

From the calibration sequences presented so far, we can infer some of the device parameters and compare them with the designed values. For the fabricated qubit, we measure the following parameters: $\omega_q/2\pi = 6.3\,\text{GHz}$, $\alpha/2\pi = -180\,\text{MHz}$, $\omega_r/2\pi = 7.06\,\text{GHz}$, $\Lambda/2\pi = 4\,\text{MHz}$, and $\chi/2\pi = 1\,\text{MHz}$. Here, $\alpha = \omega_{21} - \omega_{10}$ represents the anharmonicity, which is inferred from the two-photon excitation (Fig. 4.8 (b)). ω_r is the readout resonator frequency, $2\chi = \omega_{r,|0\rangle} - \omega_{r,|1\rangle}$ denotes the dispersive shift, and $\Lambda = g^2/\Delta$ represents the Lamb shift.

These measured values imply a Josephson energy $E_J/\hbar = 30\,\mathrm{GHz}$ in the transmon limit ($E_J \gg E_C$), where $\hbar\omega_q \approx \sqrt{8E_JE_C} - E_C$, and a charging energy $E_C \approx -\hbar\alpha$. The readout-qubit coupling is $g/2\pi = 55\,\mathrm{MHz}$, where $g \approx \sqrt{-\Delta\chi(1+\Delta/\alpha)}$, and the detuning is $\Delta = \omega_q - \omega_r$. The readout resonator has an extrinsic quality factor of $Q_e = 3.7k$ and an intrinsic quality factor $Q_i = 0.14 - 1.7 \times 10^5$, ranging from the single photon limit to the power-saturated limit.

Chapter 5

Non-Markovian dynamics of a superconducting qubit in a phononic bandgap

5.1 Introduction

A superconducting quantum processor with practical utility requires a large number of highly coherent, error-corrected qubits [88, 89, 90] to achieve quantum advantage [91, 92, 10]. Scaling recent logical qubit demonstrations [93] will require further improvements in gate and readout errors, as well as qubit footprint miniaturization. Miniaturizing superconducting qubits while improving their coherence is a challenging task, as miniaturization often leads to increased dissipation due to stronger coupling to two-level systems (TLSs). TLSs are surface or bulk defects within disordered or amorphous solids. Their strong electric and elastic dipole moments make them the dominant dissipation channel of current superconducting qubits [16, 94, 95]. Large planar qubits can reduce TLS-induced dissipation by minimizing energy participation of lossy interfaces [96, 97]. While this approach enabled improvements in qubit coherence up to a few hundred microseconds, simultaneous improvements to lifetime and footprint remain as outstanding challenges for scaling [6, 98, 99, 100].

In this work, we demonstrate an alternative approach to address the qubit footprint-dissipation trade-off by using a phonon-engineered qubit with a modified TLS bath. The electric and elastic dipole moments of TLSs mediate coupling between the superconducting qubit and the phonon bath, resulting in a phononic Purcell decay channel for the qubit. We use a phononic bandgap metamaterial as a mechanical Purcell filter to suppress the spontaneous phonon emission of TLSs, which in turn, influences the qubit relaxation time. We use the qubit to populate the TLS bath and to characterize the modified dissipative dynamics of the qubit and the TLSs [101, 102]. We observe a strong enhancement of TLS lifetime in the phononic bandgap, along with a signature of qubit lifetime improvement. The observations are well-modeled with Solomon equations for a qubit coupled to a TLS

environment [103, 26], and show non-Markovian qubit dynamics inside the phononic bandgap [104, 105]. We discuss prospects for combining phonon protection and miniaturization to enable next-generation quantum processors.

5.2 A superconducting qubit on a phononic bandgap metamaterial

According to the standard tunneling model, TLSs display strong electric (∼1 Debye) and elastic (∼1 eV) dipole transition matrix elements that result in their strong interactions with superconducting circuits and phonons [16, 106, 107]. Their linear electromechanical response can be considered as atomic-scale piezoelectricity that converts the energy of superconducting qubits to phonons. As illustrated in Fig. 5.1(b), a TLS couples to the oscillating electric field of the qubit and dissipates it to the substrate via phonon emission at a rate Γ_t^k. Consequently, the qubit experiences Purcell decay through each TLS with a rate Γ_{qt}^k. When higher order coherent effects can be ignored, the total qubit decay rate is then the sum of its intrinsic decay rate Γ_q (from non-TLS sources) and the Purcell decay rates due to the TLS ensemble:

$$\Gamma_1 = \Gamma_q + \sum_k \frac{2g_k^2 \Gamma_m}{\Gamma_m^2 + \Delta_k^2} \tag{5.1}$$

where Δ_k is the detuning between the qubit and the kth TLS, g_k is their transverse coupling strength, and $\Gamma_m = (\Gamma_q + \Gamma_t^k)/2$ is the mutual decoherence rate in the absence of dephasing [103].

The TLS lifetime is determined by the spontaneous phonon emission (Γ_t^k) rate and can be improved by suppressing the phonon density of states. If the spectral density of the phonon-protected TLS (ρ) is much smaller than mutual decoherence time ($1/\Gamma_m$), the decay rates of the qubit (Γ_1) and TLSs (Γ_t^k) are closely linked [108]. In this regime, the qubit decay Γ_1 is also expected to be suppressed, and the phononic crystal can be viewed as a mechanical Purcell filter that suppresses TLS-induced phonon emission from a superconducting qubit.

We study the modified qubit-TLS interactions on a phononic metamaterial with an engineered phonon density of states. Our device consists of an all-aluminum tunable transmon qubit on a suspended 2D phononic crystal membrane (Fig. 5.1(a)) [109]. The transmon consists of a compact interdigitated capacitor shunted to the ground through two symmetric Josephson junctions that form a superconducting quantum interference device (SQUID), as shown in Fig. 5.1(d). The SQUID loop is inductively coupled to a Z-control line for qubit frequency tuning. The transmon is capacitively coupled to an XY line for qubit control and to a $\lambda/2$ coplanar waveguide resonator for fast dispersive readout. The device is mounted at the mixing chamber stage (∼10 mK) of a dry dilution refrigerator and enclosed in multiple layers of radiation and magnetic shields.

The qubit capacitor is formed by interdigitating 1 µm-wide fingers with 1 µm gaps. The capacitor is fully engraved by the underlying phononic crystal structure as shown in

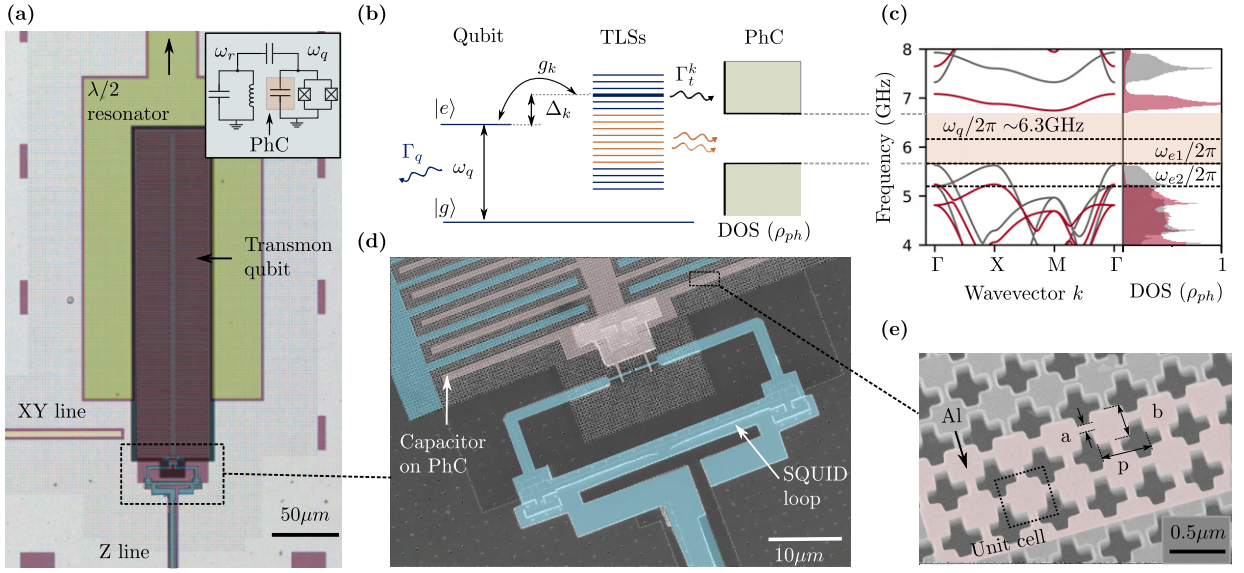

Figure 5.1: **A superconducting qubit on a phononic bandgap metamaterial.** (a) Optical micrograph (false-colored) of the transmon qubit fabricated on a suspended silicon phononic metamaterial. Inset: equivalent circuit. (b) The qubit and the kth TLS interact with coupling strength g_k and detuning Δ_k, and decay to their respective environments at rates Γ_q and Γ_t^k. (c) Simulated band structure and density of states (DOS) of the fabricated phononic crystal (PhC). Lower band edges $\omega_{e1}/2\pi = 5.6\,\text{GHz}$ and $\omega_{e2}/2\pi = 5.2\,\text{GHz}$ are for the 190 nm-thick Si (gray) and 220/50nm-thick Si/Al (red) unit cells. The complete phononic bandgap is shaded in brown. Maximum transmon frequency $\omega_q/2\pi \approx 6.3\,\text{GHz}$. (d,e) False-colored scanning electron micrographs of the SQUID loop and interdigitated capacitor on the phononic crystal. The device tested in this work does not have a phononic crystal around the Josephson junctions. (e) Unit cell dimensions: $\{a, b, p\} = \{70,\ 320,\ 445\}\,\text{nm}$.

Fig. 5.1(e). We design the 260 µm × 60 µm capacitor using an effective medium description for the dielectric constant of the phononic crystal (section 2.3.3). The mass loading due to aluminum electrodes alters the phononic band structure and shifts the lower band edge from 5.6 GHz to 5.2 GHz (Fig. 5.1(c)), a signature that will be visible in subsequent qubit measurements. The common bandgap is centered at 6.2 GHz with a 1.2 GHz bandwidth. At $\omega_q/2\pi = 6.3\,\text{GHz}$, we measure a qubit lifetime of $T_1 = 0.42\,\mu\text{s}$ and Ramsey dephasing time of $T_2^* = 0.61\,\mu\text{s}$. We tune the qubit frequency from 6.3 GHz down to 4 GHz and do not observe any avoided level crossings with TLSs(see Fig. 4.11(b)). The frequency response implies that the qubit incoherently interacts with a high-density bath of weakly coupled TLSs, consistent with the large mode volume and surface participation ratio of the design [19].

5.3 Qubit-driven TLS hole-burning inside a phononic bandgap

Qubit-TLS interactions can result in coherent or incoherent dynamics depending on the ratio of interaction strength (g_k) to the mutual decoherence rate (Γ_m). For $|g_k| > \Gamma_m$, coherent qubit-TLS oscillations can be observed using swap spectroscopy with individual TLSs [110]. For $|g_k| < \Gamma_m$ or in the case of dense TLS bath (approaching the continuum limit), the qubit and TLS population dynamics follow the Solomon rate equations [26]:

$$\dot{p}_q = -\Gamma_q(p_q - p_{th}) - \sum_k \Gamma_{qt}^k (p_q - p_t^k) \tag{5.2}$$

$$\dot{p}_t^k = -\Gamma_t(p_t^k - p_{th}) - \Gamma_{qt}^k (p_t^k - p_q) \tag{5.3}$$

where p_q, p_t, p_{th} refer to the qubit, TLS, and thermal excited state populations. In this regime, the average TLS lifetime can be measured by using a qubit-driven hole-burning sequence where we first excite the TLS bath using the qubit, and infer the bath properties from the qubit-bath thermalization dynamics. The hole-burning sequence in Fig. 5.2(a) consists of X_π pulses that prepare the qubit in the $|e\rangle$ state at a reference frequency ω_0. The excitation is subsequently exchanged with the TLS environment at ω_q by letting the qubit relax ($\tau_r > 1/\Gamma_1$). After N hole-burning pulses, we use the qubit to probe the qubit-bath thermalization dynamics as they resonantly interact at frequency ω_q for duration τ_d.

For $\Gamma_1 \gg \Gamma_t$, the qubit-TLS bath thermalization rate is faster than that of the TLSs to the phonon bath. In this regime, the qubit population approximates the equilibrium TLS population for $\tau_d \gg 1/\Gamma_1$. Fig. 5.2(b) shows the TLS population as a function of the number of hole-burning pulses N. Around $N = 200$, the TLS bath can be populated from its thermal state to around $p_{eq} \approx 30\%$ near the center of the phononic bandgap (∼6.28 GHz, black). This response shows the presence of long-lived TLSs and the emergence of a non-Markovian bath inside the phononic bandgap. This is in stark contrast to measurements performed at frequencies outside the phononic bandgap (∼4.5 GHz, gray data), where the TLSs cannot be populated and measured using the pulse sequence due to their very short lifetime (10–100 ns in Refs. [111, 19]).

These observations can be explained by considering the steady-state populations that are determined by the TLS excitation rate through the qubit ($(1-p_t)/\tau_r$) and the energy decay rate from N TLSs resonantly interacting with the qubit ($Np_t\Gamma_t$). The competition between these rates results in a steady state population $p_t \approx \Gamma_r/(\mathrm{N}\Gamma_t + \Gamma_r)$. We use this relation to infer the effective number of TLSs resonantly interacting with the qubit N = 100 TLSs at 6.28 GHz. Outside the phononic bandgap, $p_t \approx 0$ due to the fast, Markovian relaxation of the TLS bath.

We probe the spectral distribution of the populated TLS bath, and observe a peak around the hole-burning frequency with a linewidth of 6.8 ± 0.2MHz, which includes the dephasing of the probe qubit and the probed TLSs (Fig. 5.2(c)). This indicates that the populated TLSs

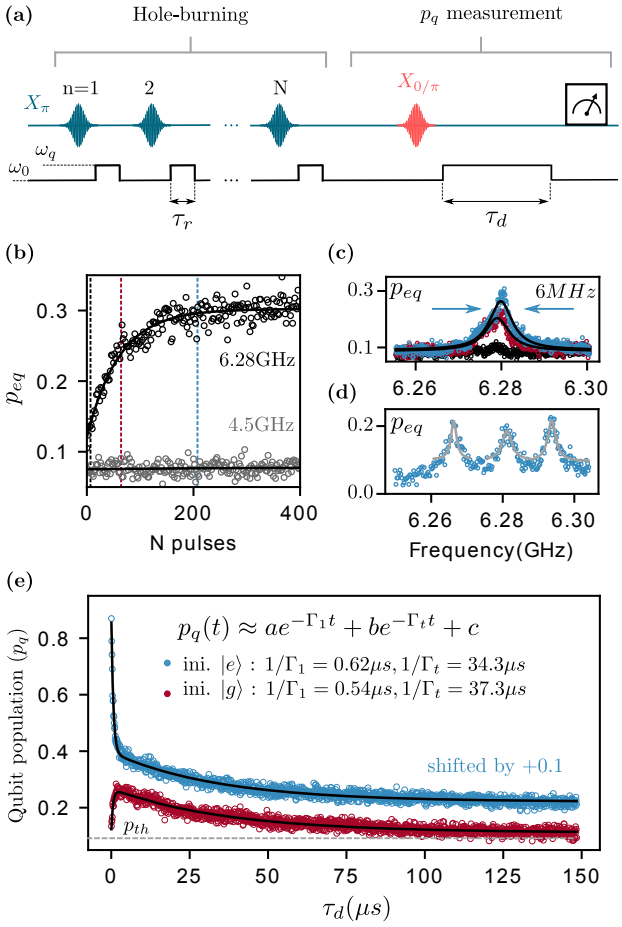

Figure 5.2: **Saturating phonon-gapped two-level systems with a qubit.** (a) Sequence for hole-burning the TLS bath and measuring its dynamics with a qubit. The qubit is prepared in the excited state at $\omega_0/2\pi = 6.3\,\text{GHz}$ and is allowed to decay at $\omega_q/2\pi = 6.28\,\text{GHz}$ by waiting for $\tau_r = 1\,\mu\text{s} > 1/\Gamma_1$. After N repetitions, the thermalization dynamics of the qubit and the saturated TLS bath are measured with the qubit initialized in state $|g\rangle$ or $|e\rangle$. The TLS equilibrium population $p_{eq} \approx p_q(\tau_d = 5\,\mu\text{s})$ as a (b) function of pulse number N inside (black) and outside (gray) the phononic bandgap, and (c) as a function of frequency around 6.28 GHz for $N = 0, 50, 200$ (black, red, blue). (d) Hole-burning at three adjacent frequencies using interleaved polarization pulses. (e) Qubit relaxation dynamics from states $|g\rangle$ (red) and $|e\rangle$ (blue) following $N = 200$ polarization pulses at 6.28 GHz. Fast (Γ_1^{-1}) and slow (Γ_t^{-1}) decay constants correspond to the qubit and TLS lifetimes. The thermal population is $p_{th} \approx 0.028$ (see Fig. 4.12(b)).

are dense ($\rho \approx 15\,\mathrm{MHz}^{-1}$) and share similar Purcell decay rates. As shown in Fig. 5.2(d), we use interleaved polarization pulses at different frequencies to saturate the TLS bath at different spectral regions, confirming the uniform, high-density distribution of the TLS bath (Fig. 5.2(d)). Under the dense and uniform bath approximation ($\Gamma_{qt}^k \approx \Gamma_{qt}$), the rate equations simplify to

$$\dot{p}_q = -\Gamma_1(p_q - p_{th}) + \Gamma_q^{TLS} p_{t,0}^* e^{-\Gamma_t t}. \tag{5.4}$$

where $\Gamma_q^{TLS} = \sum_k \Gamma_{qt}^k$, and $p_{t,0}$ represents the initial TLS population. For long-lived TLSs ($\Gamma_t \ll \Gamma_1$), the solution of the differential equation can be approximated by a biexponential form $p_q(t) \approx ae^{-\Gamma_1 t} + be^{-\Gamma_t t} + p_{th}$ (section 2.2.4). In Fig. 5.2(e), we probe the qubit decay after $N = 200$ polarization pulses with the qubit initialized in the $|g\rangle$ and $|e\rangle$ states. By fitting the data to a biexponential form, we observe that, on average, the qubit lifetime is $1/\Gamma_1 = 1/(\Gamma_\uparrow + \Gamma_\downarrow) \approx 0.58\,\mu\mathrm{s}$, where $\Gamma_\uparrow(\Gamma_\downarrow)$ is the upward (downward) transition rate and depends on the TLS population. However, the qubit lifetime ($1/\Gamma_1$) remains independent of the TLS population, and the TLS lifetime ($1/\Gamma_t$) is independent of the qubit initialization (section 2.2.4).

5.4 Non-Markovian dynamics of a phonon-protected superconducting qubit

To probe the effectiveness of the phononic bandgap, we performed the hole-burning pulse sequence used in Fig. 5.2(e) over the frequency range of 4–6.25 GHz, with a time delay of up to $\tau_d = 250\,\mu\mathrm{s}$. This measurement captures both the slow and fast qubit dynamics from which the qubit ($1/\Gamma_1$) and TLS ($1/\Gamma_t$) lifetimes can be extracted. As shown in Fig. 5.3(a), the qubit population at long delays rapidly vanishes when we move the qubit outside the phononic bandgap ($\omega < \bar{\omega}_{e2}$). The qubit decay due to TLSs can be estimated by noting that $\Gamma_q^{TLS} \propto b\Gamma_1$ where $\Gamma_q^{TLS} = \sum_k \Gamma_{qt}^k$ (Eq. 2.84). We use the results presented in Fig. 5.3(b) to experimentally locate the band edges corresponding to the Si ($\bar{\omega}_{e1}/2\pi = 5.4\,\mathrm{GHz}$) and Si/Al ($\bar{\omega}_{e2}/2\pi = 5.05\,\mathrm{GHz}$) unit cells. For $\bar{\omega}_{e2} < \omega < \bar{\omega}_{e1}$, a subset of the TLS bath leaves the bandgap and becomes short-lived, reducing both the qubit and average TLS lifetime (Fig. 5.3(c) and (d)). The phononic bandgap improves the TLS lifetime from values below the detection limit ($< 1\,\mu\mathrm{s}$) to an average of 34 µs. The qubit lifetime (Fig. 5.3(d)) shows frequency dependence and experiences a smooth increase at the band edge due to the suppression of the TLS decay. As will be shown in the next section, an approximate model of the qubit-TLS interaction can be constructed from the TLS lifetimes and Eq. 5.1, from which we estimate a coupling strength $g/2\pi \sim 50\,\mathrm{kHz}$, TLS density $\rho \sim 20\,\mathrm{MHz}^{-1}$ (in good agreement with the estimation from Fig. 5.2(c)), and the intrinsic qubit decay rate $\Gamma_q/2\pi \sim 5\,\mathrm{kHz}$.

We observe a small residual population inside the bandgap that decays far beyond $\tau_d = 250\,\mu\mathrm{s}$ suggesting the presence of a distribution of lifetimes for the TLS bath. To probe the long lifetime, we measured the relaxation dynamics of the qubit up to 20 ms for three

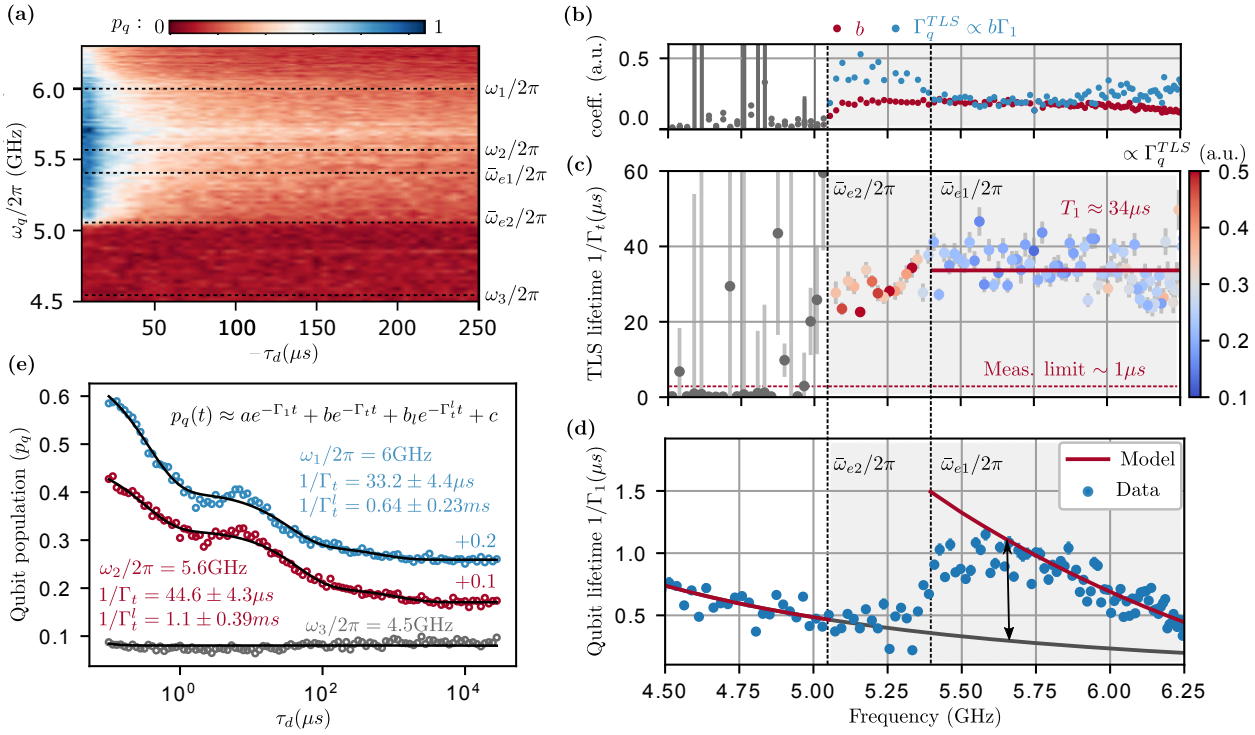

Figure 5.3: **Non-Markovian dynamics of a phonon-protected qubit.** (a) Qubit relaxation dynamics inside ($\omega > \bar{\omega}_{e2}$) and outside ($\omega < \bar{\omega}_{e2}$) the phononic bandgap after $N = 200$ polarization pulses. Experimentally extracted band edges: $\bar{\omega}_{e2}/2\pi$ =5.4 GHz and $\bar{\omega}_{e1}/2\pi$ = 5.05 GHz. Linecuts of the data are fit to the model in Fig. 5.2(e) to infer: (b) amplitude b (red) and TLS-induced qubit decay rate $\Gamma_q^{TLS} \propto b\Gamma_1$ (blue), (c) TLS lifetime ($1/\Gamma_t$), and (d) qubit lifetime ($1/\Gamma_1$). (c) The average TLS lifetime is 34 µs inside the phononic bandgap ($\omega > \bar{\omega}_{e1}$), and drops below the detection limit (<1 µs) outside the bandgap ($\omega < \bar{\omega}_{e2}$). Color-coding represents Γ_q^{TLS}. (d) Qubit lifetime undergoes a smooth increase at the band edge $\bar{\omega}_{e1}$. The model (section 5.5) suggests around twofold qubit lifetime improvement when compared with the model prediction without a phononic bandgap. (e) Slow-relaxation dynamics of the qubit for $\{\omega_1, \omega_2, \omega_3\}/2\pi = \{6, 5.6, 4.5\}$ GHz measured up to 20 ms. A tri-exponential model captures the additional slow decay timescale Γ_t^l for the TLS bath.

different frequencies as shown in Fig. 5.3(e). By fitting the data to a tri-exponential form $p_q(t) \approx ae^{-\Gamma_1 t} + be^{-\Gamma_t t} + b_l e^{-\Gamma_t^l t} + c$, we extract two major time scales of the TLS bath. We measured $1/\Gamma_t(1/\Gamma_t^l)$ of 33.2 µs (0.64 ms) for $\omega_1/2\pi = 6$ GHz and of 44.6 µs (1.1 ms) for $\omega_2/2\pi = 5.6$ GHz.

The relaxation time t $1/\Gamma_t^l$ can be limited by Purcell decay through the qubit. This effect becomes pronounced when measuring a small number of long-lived TLSs ($N/\Gamma_q \ll 1/\Gamma_t^l$). To study this effect, we used a modified TLS hole-burning sequence where the qubit is detuned

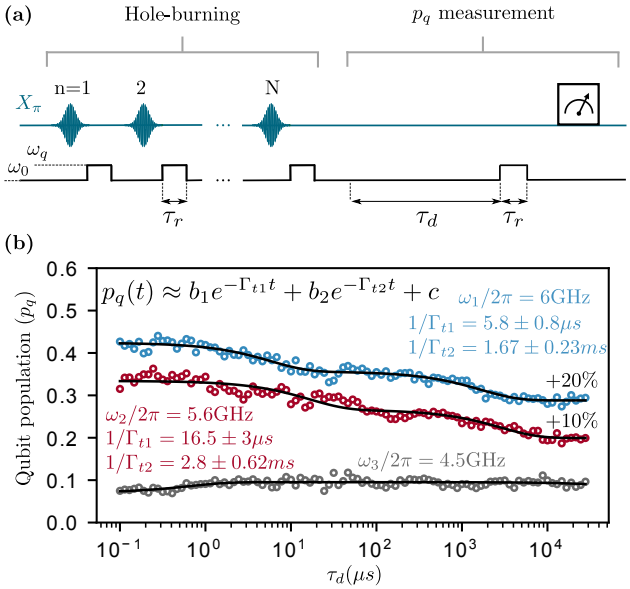

Figure 5.4: Qubit-detuned TLS decay: (a) Pulse sequence for TLS hole-burning and population measurement. The qubit is prepared in the excited state at $\omega_0/2\pi = 6.3\,\text{GHz}$ and is allowed to decay at ω_q by waiting for 1 µs. After the sequence is repeated N times, the qubit is detuned to ω_0 for τ_d, followed by thermalization at ω_q for 1 µs and qubit readout at ω_0. (b) Long-relaxation dynamics of the qubit for $\{\omega_1, \omega_2, \omega_3\}/2\pi = \{6, 5.6, 4.5\}$ GHz, measured up to 20 ms and plotted on a logarithmic scale. The curve is fitted to a biexponential form, and the lifetimes are provided in the inset.

from the TLS frequency ω_q throughout the duration τ_d, allowing the TLS bath to decay independently, as shown in Fig. 5.4(a). At the end of the sequence, the qubit is allowed to thermalize with the TLS population for τ_r, followed by a qubit readout measurement. The sequence was performed at the same frequency points of Fig. 5.3(e), and the results were fitted to the biexponential form $p_q(t) \approx b_1 e^{-\Gamma_{t1} t} + b_2 e^{-\Gamma_{t2} t} + c$. Detuning the qubit increased the long-TLS lifetime $1/\Gamma_{t2}$ from 0.64 ms to 1.67 ms at $\omega_1/2\pi = 6\,\text{GHz}$, and from 1.1 ms to 2.8 ms at $\omega_2/2\pi = 5.6\,\text{GHz}$. This suggests that the TLS and the qubit can Purcell-limit each other's lifetime.

5.5 Qubit lifetime modeling

To gain more insight into the TLS bath properties, we fitted the measured qubit lifetime $(1/\Gamma_1)$ of Fig. 5.3(d) to the qubit-decay formula (Eq. 5.1). We simplified the TLS lifetime $(1/\Gamma_t)$ into a piecewise function of 34 µs for $\omega/2\pi > 5.2\,\text{GHz}$ and 100 ns otherwise, as shown

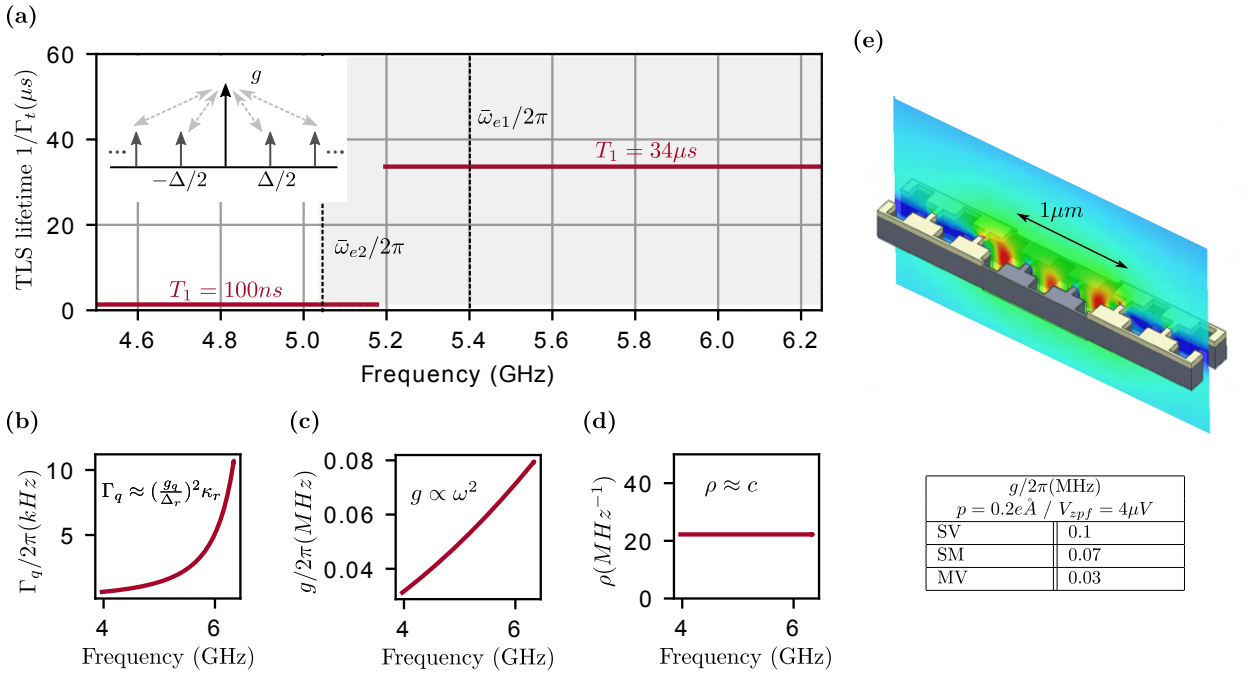

$g/2\pi$(MHz) $p = 0.2eÅ$ / $V_{zpf} = 4\mu V$	
SV	0.1
SM	0.07
MV	0.03

Figure 5.5: Qubit lifetime model parameters: (a) TLS lifetime $1/\Gamma_t$; (b) intrinsic qubit decay rate Γ_q; (c) coupling strength g; (d) TLS density ρ; and (e) electrostatic simulation of the average Qubit-TLS coupling strength ($g = pE/\hbar$), computed in 3 nm-thick substrate-vacuum (SV), substrate-metal (SM), and metal-vacuum (MV) interfaces.

in Fig. 5.5(a). The model assumes that the TLSs are uniformly distributed at a constant density $\rho = 2\pi/\Delta$ with uniform coupling strength g (inset of Fig. 5.5(a)). The sum of this distribution can be found analytically as in Eq. 2.87.

The intrinsic qubit decay $\Gamma_q = (\frac{g_r}{\omega_r - \omega})^2\kappa_r$ due to Purcell decay via the readout resonator is set by $\omega_r/2\pi = 7.1\,\text{GHz}$, a decay rate of $\kappa_r/2\pi = 2\,\text{MHz}$, and a qubit coupling strength of $g_r/2\pi = 48\,\text{MHz}$ (Fig. 5.5(b)). For the model shown in Fig. 5.3(d), we find an average qubit-TLS coupling strength $g/2\pi = a\omega^2$ with $a \approx 5 \times 10^{-11}\,\text{MHz}^{-1}$ and spans a range of 0.03–0.08 MHz (Fig. 5.5(c)). However, the frequency dependence is quadratic $g \propto \omega^2$ instead of the $g \propto \sqrt{\omega}$ frequency dependence expected from the single photon amplitude. One possible reason for the discrepancy is the oversimplification of the model, where, in practice, g has a complicated spatial and frequency dependence. Finally, the density of TLS per unity frequency $\rho \approx 20\,\text{MHz}^{-1}$ (Fig. 5.5(d)), and is constant as expected from the standard tunneling model and our estimate from hole-burning sequences [16]. The model fails to capture the region of the band edge, particularly between ω_{e1} and ω_{e2} (see Fig. 5.3(d)), where a large subset of TLSs are outside of the complete bandgap.

To estimate the average Qubit-TLS coupling strength g, we performed a 3D electrostatic

simulation for one period of the interdigitated capacitor, as shown in Fig. 5.5(e). We set the voltage between the two electrodes to V_{zpf}=4 µV, which was estimated from the measured qubit parameters at $\omega/2\pi = 6.3$ GHz using $V_{zpf} = \omega\sqrt{\hbar Z_T/2}$, and the transmon impedance $Z_T = (\Phi_0/\pi e)\sqrt{E_C/2E_J}$. The average electric field in a 3 nm thick layer on the substrate-vacuum (SV), substrate-metal (SM), and metal-vacuum (MV) interfaces are computed. From this data, the coupling strength to a TLS with a dipole moment of 0.2 eÅ can be obtained via $g = pE/\hbar$, and the results are summarized in the table of Fig. 5.5(e). The values are in good agreement with the model estimate shown in Fig. 5.5(c).

Chapter 6

Conclsusion and perspectives

We showed that embedding a superconducting qubit inside a phononic bandgap enhances the TLS bath lifetime and results in non-Markovian qubit dynamics. The TLSs inside the phononic bandgap exhibited relaxation times ranging from 34 µs to 1.1 ms, extending up to 2.8 ms when the qubit is detuned. Outside the bandgap, the relaxation time is less than 1 µs (limit of detection), consistent with the 10–100 ns measured values reported in [111, 19]. While the precise mechanism limiting the TLS lifetime is currently unknown and subject to further study, we expect that lower disorder phononic metamaterials with larger bandgaps would result in further improvements to TLS lifetimes and suppress non-resonant relaxation mechanisms [112, 113].

An intriguing question is whether our phonon engineering approach, which leads to enhancements in TLS lifetimes, can also improve the lifetimes of future superconducting qubits. The qubit relaxation rate and its relation to TLS lifetimes are governed by Eq. 5.1, exhibiting two main limits that are illustrated in Fig. 6.1(a). The *Fermi-limit* is reached when the density of TLSs is large and approaches the continuum. In this regime, the TLS relaxation rate does not have a strong influence on the qubit lifetime, and the qubit decay rate follows that of Fermi's golden rule, $\Gamma_q^{TLS} \propto g^2\rho$. The *Purcell-limit* is reached when the density of TLSs is small, and the relevant TLS distribution can be truncated to a few nearest neighbors. In this limit, the TLS relaxation rate has a direct influence on the qubit lifetime, and the qubit decay rate follows the Purcell formula, $\Gamma_q^{TLS} \propto (g/\Delta)^2\Gamma_t$.

Our experiment is in the Fermi-limit where we observe only a modest improvement in the qubit lifetime inside the bandgap (Fig. 5.3(d)) due to the high TLSs density ($\rho \approx 20\,\mathrm{MHz}^{-1}$). Commonly used qubits also operate in the Fermi-limit regime and mitigate TLS loss through optimized fabrication processes (reduce ρ) and large planar geometries that reduce TLS coupling strength (reduce g) and energy participation ratio [19, 98]. Therefore, phononic shielding is not expected to significantly improve their lifetime. However, phonon-shielding is expected to be more effective for miniaturized qubits operating in the *Purcell-limit* with low TLS density. We take the recently developed Al/AlO_x/Al merged element transmon (Mergemon) as an example [114], which has near unity energy participation ratio in the thin AlO_x dielectric layer, and a reported TLS density per unit volume of $\rho_0 = 100\,\mu\mathrm{m}^{-3}\,\mathrm{GHz}^{-1}$

[19]. This allows us to establish an analytical relationship between the TLS density and coupling strength ($\rho \approx 1.425 \times 10^6[\mathrm{Hz}]/g^2$). To see this, the Mergemon's capacitance is modeled as that of a parallel plate, where $C = \epsilon A/d$. The electric field in the AlO_x dielectric layer is given by $E = V_{zpf}/d$. Using this, we can obtain the coupling strength to defect TLSs with a dipole moment p as $g = pE/\hbar$. The TLS density per unit frequency can be expressed as:

$$\begin{aligned} \rho &= \rho_0 A d \\ &= \frac{\rho_0 A V_{zpf} p}{\hbar} \times \frac{1}{g} \\ &= \frac{\rho_0 C V_{zpf}^2 p^2}{\epsilon \hbar^2} \times \frac{1}{g^2} \\ &\approx 1.425 \times 10^6 [Hz] \frac{1}{g^2} \end{aligned} \tag{6.1}$$

where in the last line, we assumed a 3.8 GHz qubit frequency and a capacitance $C = 70\,\mathrm{fF}$, from which we obtain a zero-point voltage fluctuation of $V_{zpf} = 4\,\mu\mathrm{V}$. The AlO_x relative permittivity $\epsilon_r = 10$ has a TLS density per unit volume per unit frequency $\rho_0 = 100\,\mu\mathrm{m}^{-3}\,\mathrm{GHz}^{-1}$ and a dipole moment of $p = 0.2\,\mathrm{e\AA}$. For the Mergemon design reported in [114] with area $A = 1.4\,\mu\mathrm{m}^2$ and dielectric thickness $d = 2\,\mathrm{nm}$, we have $\rho = 0.35\,\mathrm{GHz}^{-1}$ and $g/2\pi \approx 10\,\mathrm{MHz}$.

We also assume a uniform distribution of the TLSs, which allows for an analytical expression of the sum in Eq. 5.1 (section 2.2.5). In Fig. 6.1(b), the Mergemon relaxation time ($1/\Gamma_1$) is plotted as a function of the TLS relaxation time ($1/\Gamma_t$) and coupling strength (g), assuming no intrinsic loss ($\Gamma_q = 0$). The color map clearly illustrates the Fermi-limited and Purcell-limited regimes, showing quantitatively the influence of the TLS lifetime on the qubit lifetime in each regime. Our numerical calculations validate the limited improvement of the qubit lifetime in this work ($g/2\pi \approx 0.05\,\mathrm{MHz}$, $\rho \approx 20\,\mathrm{MHz}^{-1}$), and also affirm the $\sim$100 µs reported Mergemon lifetime with ($g/2\pi \approx 10\,\mathrm{MHz}$, $\rho \approx 0.4\,\mathrm{GHz}^{-1}$) [114]. The Mergemon with 1.4 µm area clearly operates in the Purcell limit, and phonon shielding is expected to improve its TLS-limited lifetime to the millisecond timescale.

We note that the impact of the phononic crystal on the TLS and qubit Ramsey coherence time T_2^* is currently unknown. The dephasing of high-frequency TLSs are dominated by the longitudinal coupling with many low-frequency TLS fluctuators ($\hbar\omega < k_B T$), resulting in telegraphic noise and spectral diffusion [16]. We expect that the emergence of non-Markovian qubit-TLS dynamics and long relaxation times via phonon engineering will yield similar improvements in coherence via dynamical decoupling [115, 116].

Finally, it is advantageous to explore other phononic crystal shield designs with lower TLS density, such as the epitaxial Si/SiGe superlattices presented in section 3.3. Increasing the qubit frequency, which is otherwise avoided due to ($g \propto \sqrt{\omega_q}$), will allow overcoming the critical thickness growth limit of the superlattice, enabling the development of fully epitaxial shields with low TLS defects.

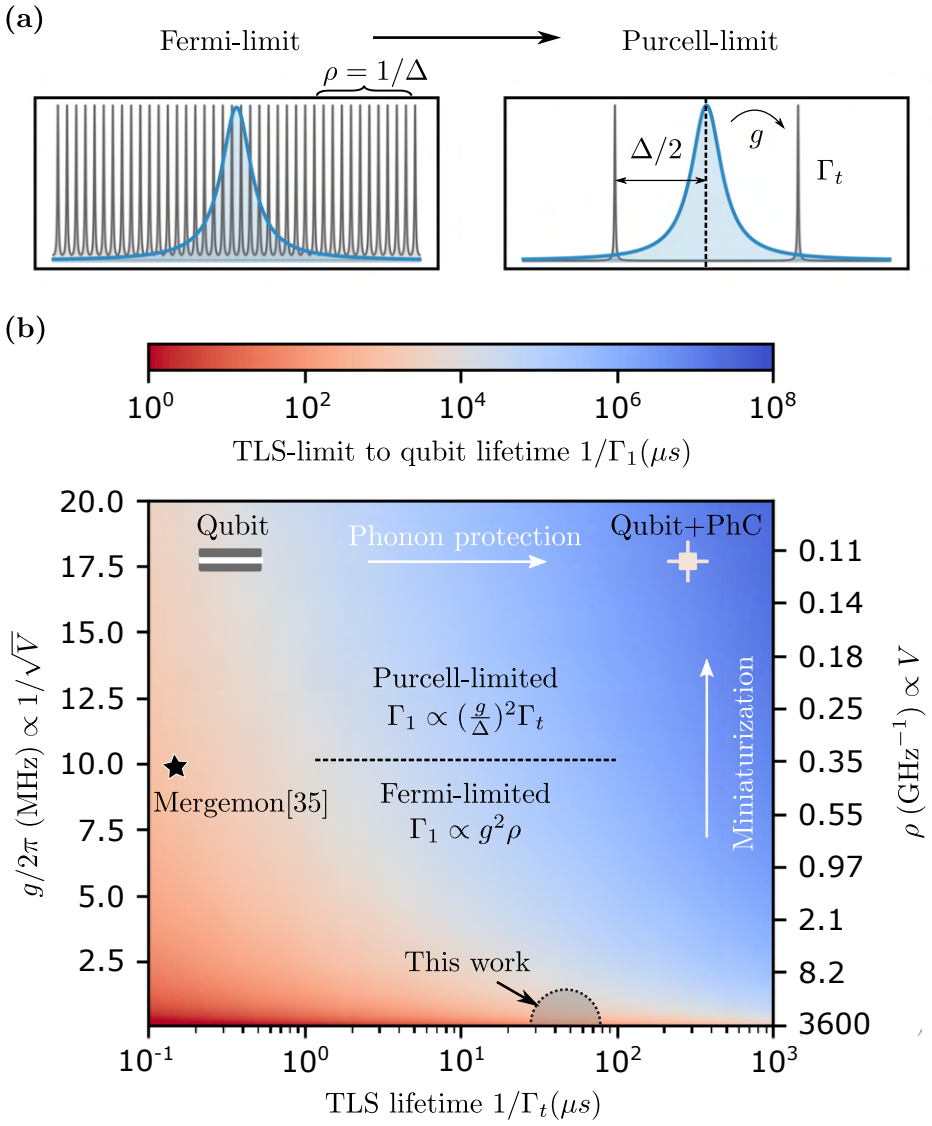

Figure 6.1: **Qubit-TLS interaction regimes.** (a) Illustrative model of qubit (blue) and TLS (gray) spectra in the Fermi and Purcell limits. (b) TLS-limited qubit relaxation time $1/\Gamma_1$ calculated using the analytical sum of Eq. 5.1 and assuming $\Gamma_q = 0$, $g \propto 1/\sqrt{V}$ and $\rho \propto V$, where V is the dielectric volume. The parameters assume full participation ratio Al/AlO_x/Al Mergemon qubit from Ref. [114]. Reducing the qubit size transitions the relaxation rate from being Fermi-limited (independent of Γ_t) to being Purcell-limited (proportional to Γ_t). The model predicts significant improvements in the TLS-limited qubit lifetime by combining miniaturization and phonon shielding (upper right-hand corner).

Appendix A

Fabrication process

A.1 SOI Qubit

Aluminium sputtering	
Acid clean	(msink8) - piranha clean (H_2SO_4+H_2O_2) for 10 min + QDR - dilute HF dip for 1 min + QDR (msink6) - piranha clean (H_2SO_4+H_2O_2) for 10 min + QDR - dilute HCL for 1 min + QDR - dilute HF for 1 min + QDR
Al sputter	(ast-sputter) - 200 sccm Ar, 3 mTorr, 150 W, 15 nm/min, 3 min (45 nm) or (aln2) - 15 sccm Ar, 2 kW 150 nm/min, 20 sec (50 nm)
Nb markers	
Resist coating	(picotrack1) - MIR701 1 µm- no HMDS
Exposure	(MLA150) - Dose: 210 mJ, focus: -2, (CD 1 μm), - CD adjustment: -200 nm x, -200 nm y - High quality patterning option
Development	(picotrack2) - MIR701 development recipe
Descum	(yes-g500) - Electron-free ion trap (AGG*A) - 200 W for 1 min with a carrier wafer
Nb sputter	(ast-sputter)

	- 130 sccm Ar, 2 mTorr, 500 W, 28 nm/min, 7 min (200 nm)
Lift off	(ASAP-liftoff) Recipe 7
Solvent clean	(msink1) - 30 min in 80 °C 1165 + QR

Dicing

Dicing	(picotrack1) - Spin protection resist: MIR701 2 µm coat recipe - no HMDS (Disco) - Dice SOI wafer to 1 cm ×1 cm chips
Solvent clean	(msink1) - 30 min in 80 °C 1165 + QDR

Phononic crystal & release holes

Resist coating	(msink1) - Dehydration bake: hot plate 150 °C for 2 min - Spin CSAR 62: 3000 rpm - 3000 acc - 60 s (230 nm) - Soft bake: 150 °C for 60 s
Exposure	(Cresteck 50keV - PhC) - Thermalization wait: 30 min - Current: 50 pA - Field size/ Resolution: 300 µm/60,000 dot (5 nm) - Dose: 170 µC cm^{-2} / 0.77 µs - Bias: −5 nm -PEC model (200nm ZIP on SOI) (Cresteck 50keV - holes) - Current: 1 nA - Field size/ Resolution: 600 µm/20,000 dot (30 nm) - Dose: 300 µC cm^{-2} 2.7 µs - Field Overlap: 10 μm / 10 μm -P.S. Beam drift issues of PhC are mitigated by sorting the writing order with beamer and writing the holes first for better thermalization
Development	(msink1) -Develop in cold AR600-546 for 1 min+30 s IPA
Al etch	(Lam7) -Santovac bondage -CL_2 45 sccm/BCL_3 45 sccm/He 15 sccm -ICP 200 W / RF 20 W -Etch time: 15 s →60 nm Al etch
Si etch	(Lam8) -CL_2 50 sccm/HBr 150 sccm/O_2 5 sccm -ICP 300 W / RF 50 W

	-Etch time: 90 s →250 nm Si etch -DI water passivation + N2 Dry
Stripping	(msink3) - 30 min in 80 °C 1165 + QDR - 2 min Acetone sonication - 2 min Isopropanol sonication - 1 min DI water rinse + N_2 dry (yes-g500) - Electron-free ion trap (AGG*A) - 400 W for 5 min with a carrier wafer

Microwave circuits

Resist coating	(msink1) -Dehydration bake: hot plate 150 °C for 2 min - Spin PMMA A6: 3000 rpm - 3000 acc - 60 s (400 nm) - Soft bake: 180 °C for 60 s
Exposure	(Cresteck 50keV) - Current: 20 nA - Field size/ Resolution: 1200 µm/10,000 dot (120 nm) - Dose: 210 µC cm^{-2}, 3 µs (2×1.5) - Multipass mode : 2, offset X=0.03 Y=0.03 (reduces stitching) - PEC model (400nm PMMA on SOI)
Development	(msink1) -Develop in RT MBIK/IPA 1:3 for 1 min+30 s IPA
Al etch	(Lam7) -Santovac bondage -CL_2 45 sccm/BCL_3 45 sccm/He 15 sccm -ICP 200 W / RF 20 W -Etch time: 30 s →60 nm Al etch + 30 nm Si overetch -DI water passivation + N2 Dry
Stripping	(msink3) - 30 min in 80 °C 1165 + QDR - 2 min Acetone sonication - 2 min Isopropanol sonication - 1 min DI water rinse + N_2 dry

Josephson junction

Bilayer resist	(msink1) -Dehydration bake: hot plate 150 °C for 2 min - Spin EL9: 2000 rpm - 1000 acc - 90 s (0.4 µm) - Soft bake: 150 °C for 90 s - Spin CSAR 62: 3000 rpm - 1000 acc - 60 s (0.2 µm)

	- Soft bake: 150 °C for 60 s
Exposure	(Cresteck 130keV- JJ) - Thermalization wait: 30 min - Current: 100 pA - Field size/ Resolution: 300 µm/60,000 dot (5 nm) - Dose: 1100 µC cm^{-2} 2.75 µs (Cresteck 130keV- Pads) - Current: 2 nA - Field size/ Resolution: 300 µm/20,000 dot (5 nm) - Dose: 1100 µC cm^{-2} 1.24 µs
Development	(msink1) -Develop in cold AR600-546 for 1 min+30 s IPA -Develop in cold IPA-MBIK for 1 min+30 s IPA
Descum	(yes-g500) - Electron-free ion trap (AGG*A) - 200 W for 1 min with a carrier wafer
Evaporation	(Plassys MEB550) - Pump to 4×10^{-8} mbar base pressure - Getter with Ti (3 min, 0.2 nm s^{-1}) - Evaporate Al (30 nm, 0.3 nm s^{-1}, $\theta = 45, \phi = 0$) - Wait: 10 min cooldown - Oxidation: 20 min at 20 mbar dynamic oxidation - Getter with Ti (3 min, 0.2 nm s^{-1}) - Evaporate Al (30 nm/40 nm, 0.3 nm s^{-1}, at $\theta = 45, \phi_1 = -90, \phi_2 = 90$)
Lift-off	(msink16) - 1 h Acetone bath at 50 °C - 1 min Acetone sonication and bath renewal - 1 h Acetone bath at 50 °C - 30 min in 80 °C 1165 + QDR - 2 min Acetone clean - 2 min Isopropanol clean - 1 min DI water rinse + N_2 dry
Bandage pads & Airbridges	
Bilayer resist	(msink1) -Dehydration bake: hot plate 150 °C for 2 min - Spin EL9: 2000 rpm - 1000 acc - 90 s (0.4 µm) - Soft bake: 150 °C for 90 s - Spin CSAR 62: 3000 rpm - 1000 acc - 60 s (0.2 µm) - Soft bake: 150 °C for 60 s
Exposure	(Cresteck 130keV- Pads) - Current: 2 nA

	- Field size/ Resolution: 300 µm/20,000 dot (5 nm) - Dose: 1100 µC cm^{-2} 1.24 µs
Development	(msink1) -Develop in cold AR600-546 for 1 min+30 s IPA -Develop in cold IPA-MBIK for 1 min+30 s IPA
Descum	(yes-g500) - Electron-free ion trap (AGG*A) - 200 W for 1 min with a carrier wafer
Evaporation	(Plassys MEB550) - Pump to 1×10^{-7} mbar base pressure - Getter with Ti (3 min, 0.2 nm s^{-1}) - Ion milling: 400 V 10 mA, V_{acc} =80 V,6 min of ion milling, 10 % duty-cycle (2 s on - 18 s off) - Evaporate Al (200 nm, 1 nm s^{-1}, $\theta = 0, \phi = 0$)
Lift-off	(msink16) - 1 h Acetone bath at 50 °C - 1 min Acetone sonication and bath renewal - 1 h Acetone bath at 50 °C - 30 min in 80 °C 1165 + QDR - 2 min Acetone clean - 2 min Isopropanol clean - 1 min DI water rinse + N_2 dry
Airbridges	(westbond) - bond 1: 380 for 40 ms - bond 2: 380 for 40 ms
Device Releasing	
Releasing	(Primax) -Recipe 2 : 10 min/cycle-12 cycles - 36 nm/min(Etch: 4.4 μm) (Vacoven3) - 200 °C in a vacuum oven (stress relief - optional)
PCB packaging	
Wirebonding	(westbond) - bond 1: 380 for 40 ms - bond 2: 380 for 40 ms

A.2 Si/SiGe resonator

Si/SiGe growth & Nb sputtering	
Acid clean	(msink6) - dilute HCL for 1 min + QDR - dilute HF for 1 min + QDR
Si/SiGe growth	(Amatepi) - High-T bake: 1100 °C for 10 min under H_2 - epi-$Si_{0.75}Ge_{0.25}$: 650 °C, SiH_4:60 sccm, GeH_4:10 sccm, 130 s (260 nm) - epi-Si: 800 °C, SiH_4:30 sccm, 180 s (310 nm) * repeat the last two steps for N=20 times
Nb sputter	(ast-sputter) - 130 sccm Ar, 2 mTorr, 500 W, 28 nm/min, 7 min (200 nm)
Dicing	
Dicing	(picotrack1) - Spin protection resist: MIR701 2 µm coat recipe - no HMDS (Disco) - Dice Si/SiGe wafer to 1 cm ×1 cm chips
Solvent clean	(msink1) - 30 min in 80 °C 1165 + QDR
Nb resonator	
Resist coating	(msink1) - Dehydration bake: hot plate 150 °C for 2 min - Spin MIR701: 6000 rpm - 3000 acc - 60 s (0.9 µm) - Soft bake: 90 °C for 90 s
Exposure	(MLA150) - Dose: 210 mJ, focus: -2, (CD 1 μm), - CD adjustment: −200 nm x, −200 nm y - High quality patterning option
Development	(msink 1) - Post exposure bake: 110 °C for 90 sec - Develop in MF-26A for 1 min+30 s DI water
Nb etch	(Lam7) -CL_2 130 sccm /He 10 sccm -ICP 400 W / RF 100 W -Etch time: 30 s →230 nm Nb etch
Stripping	(msink3) - 30 min in 80 °C 1165 + QDR - 2 min Acetone sonication

	- 2 min Isopropanol sonication - 1 min DI water rinse + N_2 dry
Airbridges	
Resist (scaffold)	(msink1) - Dehydration bake: hot plate 150 °C for 2 min - Spin MIR900: 4000 rpm - 1000 acc - 90 s (3 µm) - Soft bake: 90 °C for 90 s
Exposure	(MLA150) - Dose: 250 mJ, focus: -2, (CD 1 μm), - CD adjustment: -200 nm x, -200 nm y - High quality patterning option
Development	(msink 1) - Post exposure bake: 110 °C for 90 sec - Develop in MF-26A for 1 min+30 s DI water
Reflow	(msink1) Reflow bake: 150° for 5 min
Descum	(yes-g500) - Electron-free ion trap (AGG*A) - 200 W for 1 min with a carrier wafer
Evaporation	(Plassys MEB550) - Pump to 1×10^{-7} mbar base pressure - Getter with Ti (3 min, 0.2 nm s^{-1}) - Ion milling: 400 V 10 mA, V_{acc} =80 V,6 min of ion milling, 10 % duty-cycle (2 s on - 18 s off) - Evaporate Al (200 nm, 1 nm s^{-1}, $\theta = 0, \phi = 0$)
Resist (release)	(msink1) - Spin MIR701: 6000 rpm - 1000 acc - 90 s (0.9 µm) - Soft bake: 90 °C for 90 s
Exposure	(MLA150) - Dose: 250 mJ, focus: -2, (CD 1 μm), - CD adjustment: -200 nm x, -200 nm y - High quality patterning option
Development	(msink 1) - Post exposure bake: 110 °C for 90 sec - Develop in MicroDev for 1 min+30 s DI water *P.S. MIR701 attacks Al and should be avoided
Al wet etch	(msink16) Al Etchant: 3.5 min (or until clear) +30 s DI water *Caution must be taken not to over-etch
Release	(yes-g500) - Electron-free ion trap (AGG*A)

	- 400 W for 5 min with a carrier wafer (msink3) - 2 h in 80 °C 1165 + QDR - 2 min Acetone sonication - 2 min Isopropanol sonication - 1 min DI water rinse + N_2 dry (yes-g500) - Electron-free ion trap (AGG*A) - 400 W for 5 min with a carrier wafer
PCB packaging	
Wirebonding	(westbond) - bond 1: 380 for 40 ms - bond 2: 380 for 40 ms

Bibliography

[1] H. Kamerlingh Onnes. "The Resistance of Pure Mercury at Helium Temperatures." In: *Commun. Phys.* 12 (1 1911).

[2] J. Bardeen, L. N. Cooper, and J. R. Schrieffer. "Microscopic Theory of Superconductivity". In: *Phys. Rev.* 106 (1 Apr. 1957), pp. 162–164.

[3] B.D. Josephson. "Possible new effects in superconductive tunnelling". In: *Physics Letters* 1.7 (1962), pp. 251–253. ISSN: 0031-9163.

[4] P. W. Anderson and J. M. Rowell. "Probable Observation of the Josephson Superconducting Tunneling Effect". In: *Phys. Rev. Lett.* 10 (6 Mar. 1963), pp. 230–232.

[5] Ted Van Duzer and Charles W. Turner. *Principles of Superconductive Devices and Circuits, (Second Ed.)* USA: Prentice Hall PTR, 1998. ISBN: 0132627426.

[6] Irfan Siddiqi. "Engineering high-coherence superconducting qubits". In: *Nature Reviews Materials* 6.10 (2021), pp. 875–891.

[7] John M. Martinis, Michel H. Devoret, and John Clarke. "Energy-Level Quantization in the Zero-Voltage State of a Current-Biased Josephson Junction". In: *Phys. Rev. Lett.* 55 (15 Oct. 1985), pp. 1543–1546.

[8] Y. Nakamura, Yu. A. Pashkin, and J. S. Tsai. "Coherent control of macroscopic quantum states in a single-Cooper-pair box". In: *Nature* 398.6730 (1999), pp. 786–788.

[9] Jens Koch et al. "Charge-insensitive qubit design derived from the Cooper pair box". In: *Phys. Rev. A* 76 (4 Oct. 2007), p. 042319.

[10] Lov K. Grover. "A Fast Quantum Mechanical Algorithm for Database Search". In: *Proceedings of the Twenty-Eighth Annual ACM Symposium on Theory of Computing*. STOC '96. Philadelphia, Pennsylvania, USA: Association for Computing Machinery, 1996, pp. 212–219. ISBN: 0897917855.

[11] L. DiCarlo et al. "Demonstration of two-qubit algorithms with a superconducting quantum processor". In: *Nature* 460.7252 (2009), pp. 240–244.

[12] Abhinav Kandala et al. "Hardware-efficient variational quantum eigensolver for small molecules and quantum magnets". In: *Nature* 549.7671 (2017), pp. 242–246.

[13] Nissim Ofek et al. "Extending the lifetime of a quantum bit with error correction in superconducting circuits". In: *Nature* 536.7617 (2016), pp. 441–445.

[14] Frank Arute et al. "Quantum supremacy using a programmable superconducting processor". In: *Nature* 574.7779 (2019), pp. 505–510.

[15] P. G. Klemens and Franz Eugen Simon. "The thermal conductivity of dielectric solids at low temperatures (Theoretical)". In: *Proceedings of the Royal Society of London. Series A. Mathematical and Physical Sciences* 208.1092 (1951), pp. 108–133.

[16] Clemens Müller, Jared H Cole, and Jürgen Lisenfeld. "Towards understanding two-level-systems in amorphous solids: insights from quantum circuits". In: *Reports on Progress in Physics* 82.12 (Oct. 2019), p. 124501.

[17] Alexander P. M. Place et al. "New material platform for superconducting transmon qubits with coherence times exceeding 0.3 milliseconds". In: *Nature Communications* 12.1 (2021), p. 1779.

[18] Conal E. Murray. "Material matters in superconducting qubits". In: *Materials Science and Engineering: R: Reports* 146 (2021), p. 100646. ISSN: 0927-796X.

[19] R. Barends et al. "Coherent Josephson Qubit Suitable for Scalable Quantum Integrated Circuits". In: *Phys. Rev. Lett.* 111 (8 Aug. 2013), p. 080502.

[20] Alexandre Blais et al. "Circuit quantum electrodynamics". In: *Rev. Mod. Phys.* 93 (2 May 2021), p. 025005.

[21] P. Krantz et al. "A quantum engineer's guide to superconducting qubits". In: *Applied Physics Reviews* 6.2 (2019), p. 021318.

[22] David M Pozar. *Microwave engineering; 3rd ed.* Hoboken, NJ: Wiley, 2005.

[23] Markus Aspelmeyer, Tobias J. Kippenberg, and Florian Marquardt. "Cavity optomechanics". In: *Rev. Mod. Phys.* 86 (4 Dec. 2014), pp. 1391–1452.

[24] David M Pozar. *Microwave engineering; 3rd ed.* Hoboken, NJ: Wiley, 2005.

[25] A. A. Houck et al. "Controlling the Spontaneous Emission of a Superconducting Transmon Qubit". In: *Phys. Rev. Lett.* 101 (8 Aug. 2008), p. 080502.

[26] Martin Spiecker et al. *Solomon equations for qubit and two-level systems.* 2023.

[27] Emely Wiegand. "Quantum Optics and Waveguide Quantum Electrodynamics in Superconducting Circuits". PhD thesis. Göteborg, Sweden, 2021.

[28] I. Solomon. "Relaxation Processes in a System of Two Spins". In: *Phys. Rev.* 99 (2 July 1955), pp. 559–565.

[29] D. (Daniel) Royer. *Elastic waves in solids.* eng. Advanced texts in physics. Berlin ; Springer, 2000 - 2000. ISBN: 3540659323.

[30] David J. Bergman. "The dielectric constant of a composite material—A problem in classical physics". In: *Physics Reports* 43.9 (1978), pp. 377–407. ISSN: 0370-1573.

[31] Peter Groszkowski and Jens Koch. "Scqubits: a Python package for superconducting qubits". In: *Quantum* 5 (Nov. 2021), p. 583. ISSN: 2521-327X.

[32] M. Checchin et al. "Measurement of the Low-Temperature Loss Tangent of High-Resistivity Silicon Using a High-Q Superconducting Resonator". In: *Phys. Rev. Appl.* 18 (3 Sept. 2022), p. 034013.

[33] M. Checchin et al. "Measurement of the Low-Temperature Loss Tangent of High-Resistivity Silicon Using a High-Q Superconducting Resonator". In: *Phys. Rev. Appl.* 18 (3 Sept. 2022), p. 034013.

[34] Riccardo Manenti et al. "Full control of superconducting qubits with combined on-chip microwave and flux lines". In: *Applied Physics Letters* 119.14 (2021), p. 144001.

[35] Mohammad Mirhosseini et al. "Superconducting qubit to optical photon transduction". In: *Nature* 588 (7839 2020), pp. 599–603. ISSN: 14764687.

[36] F. Lecocq et al. "Control and readout of a superconducting qubit using a photonic link". In: *Nature* 591.7851 (Mar. 2021), pp. 575–579. ISSN: 1476-4687.

[37] U. Patel et al. "Coherent Josephson phase qubit with a single crystal silicon capacitor". In: *Applied Physics Letters* 102.1 (2013), p. 012602.

[38] Andrew J. Keller et al. "Al transmon qubits on silicon-on-insulator for quantum device integration". In: *Applied Physics Letters* 111.4 (2017), p. 042603.

[39] C. M. Quintana et al. "Characterization and reduction of microfabrication-induced decoherence in superconducting quantum circuits". In: *Applied Physics Letters* 105.6 (2014), p. 062601.

[40] Robert Mroczyński et al. "Optimization of Ultra-Thin Pulsed-DC Magnetron Sputtered Aluminum Films for the Technology of Hyperbolic Metamaterials". In: *Crystals* 10.5 (2020). ISSN: 2073-4352.

[41] Yasushi Nakajima et al. "Growth of Single-Crystal Aluminum Films on Silicon Substrates by DC Magnetron Sputtering*". In: *Japanese Journal of Applied Physics* 31.6R (June 1992), p. 1860.

[42] H. Cerva et al. "Aluminum Spiking Mechanism in Contact Holes Studied by High-Resolution Analytical TEM". In: *MRS Proceedings* 523 (1998), p. 115.

[43] Steven A. Vitale, Heeyeop Chae, and Herbert H. Sawin. "Silicon etching yields in F2, Cl2, Br2, and HBr high density plasmas". In: *Journal of Vacuum Science and Technology A* 19.5 (2001), pp. 2197–2206.

[44] Paul E. Riley. "Plasma Etching of Aluminum Metallizations for Ultralarge Scale Integrated Circuits". In: *Journal of The Electrochemical Society* 140.5 (May 1993), p. 1518.

[45] Eiji Suzuki et al. "Highly selective and precisely controlled aluminum etching by Ar/HBr/CH3F/O2 gas chemistry". In: *Japanese Journal of Applied Physics* 53.3S2 (Mar. 2014), p. 03DD01.

[46] Vinay Ambegaokar and Alexis Baratoff. "Tunneling Between Superconductors". In: *Phys. Rev. Lett.* 10 (11 June 1963), pp. 486–489.

[47] A. Dunsworth et al. "Characterization and reduction of capacitive loss induced by sub-micron Josephson junction fabrication in superconducting qubits". In: *Applied Physics Letters* 111.2 (2017), p. 022601.

[48] J M Kreikebaum et al. "Improving wafer-scale Josephson junction resistance variation in superconducting quantum coherent circuits". In: *Superconductor Science and Technology* 33.6 (Apr. 2020), 06LT02.

[49] Alexander Bilmes et al. "In-situ bandaged Josephson junctions for superconducting quantum processors". In: *Superconductor Science and Technology* 34.12 (Oct. 2021), p. 125011.

[50] P. J. Koppinen, L. M. Väistö, and I. J. Maasilta. "Complete stabilization and improvement of the characteristics of tunnel junctions by thermal annealing". In: *Applied Physics Letters* 90.5 (2007), p. 053503.

[51] Heini Ritala, Jyrki Kiihamäki, and Mikko Heikkilä. "Studies on aluminium corrosion during and after HF vapour treatment". In: *Microelectronic Engineering* 87.3 (2010). Materials for Advanced Metallization 2009, pp. 501–504. ISSN: 0167-9317.

[52] Zijun Chen et al. "Fabrication and characterization of aluminum airbridges for superconducting microwave circuits". In: *Applied Physics Letters* 104.5 (2014), p. 052602.

[53] G.E. Ponchak, J. Papapolymerou, and M.M. Tentzeris. "Excitation of coupled slotline mode in finite-ground CPW with unequal ground-plane widths". In: *IEEE Transactions on Microwave Theory and Techniques* 53.2 (2005), pp. 713–717.

[54] Gheorghe Stan, Stuart B. Field, and John M. Martinis. "Critical Field for Complete Vortex Expulsion from Narrow Superconducting Strips". In: *Phys. Rev. Lett.* 92 (9 Mar. 2004), p. 097003.

[55] C. Song et al. "Reducing microwave loss in superconducting resonators due to trapped vortices". In: *Applied Physics Letters* 95.23 (2009), p. 232501.

[56] Sihao Huang et al. "Microwave Package Design for Superconducting Quantum Processors". In: *PRX Quantum* 2 (2 Apr. 2021), p. 020306.

[57] Benjamin Lienhard et al. "Microwave Packaging for Superconducting Qubits". In: *2019 IEEE MTT-S International Microwave Symposium (IMS)*. 2019, pp. 275–278.

[58] J Wenner et al. "Wirebond crosstalk and cavity modes in large chip mounts for superconducting qubits". In: *Superconductor Science and Technology* 24.6 (Mar. 2011), p. 065001.

[59] E. T. Swartz and R. O. Pohl. "Thermal boundary resistance". In: *Rev. Mod. Phys.* 61 (3 July 1989), pp. 605–668.

[60] M. S. Khalil et al. "An analysis method for asymmetric resonator transmission applied to superconducting devices". In: *Journal of Applied Physics* 111.5 (2012), p. 054510.

[61] J. M. Hartmann, A. Abbadie, and S. Favier. "Critical thickness for plastic relaxation of SiGe on Si(001) revisited". In: *Journal of Applied Physics* 110.8 (Oct. 2011), p. 083529. ISSN: 0021-8979.

[62] Zijun Chen et al. "Fabrication and characterization of aluminum airbridges for superconducting microwave circuits". In: *Applied Physics Letters* 104.5 (Feb. 2014), p. 052602. ISSN: 0003-6951.

[63] J. Wenner et al. "Excitation of Superconducting Qubits from Hot Nonequilibrium Quasiparticles". In: *Phys. Rev. Lett.* 110 (15 Apr. 2013), p. 150502.

[64] John Mark Kreikebaum. "Superconducting Qubit Enabled Single Microwave Photon Detection". English. Ph.D. PhD thesis. United States – California, 2020, p. 121. ISBN: 9798582501268.

[65] Frank Pobell. *Matter and Methods at Low Temperatures*. Springer Berlin Heidelberg, 2007.

[66] R.N Richardson and B.E Evans. "A review of pulse tube refrigeration". In: *International Journal of Refrigeration* 20.5 (1997), pp. 367–373. ISSN: 0140-7007.

[67] Robert A. Ackermann. *Cryogenic Regenerative Heat Exchangers*. Springer US, 1997.

[68] A. T. A. M. de Waele. "Basic Operation of Cryocoolers and Related Thermal Machines". In: *Journal of Low Temperature Physics* 164.5 (June 2011), p. 179. ISSN: 1573-7357.

[69] Salvatore Celozzi and Rodolfo Araneo. *Electromagnetic Shielding*. John Wiley and Sons, Ltd, 2005. ISBN: 9780471654506.

[70] R. Barends et al. "Minimizing quasiparticle generation from stray infrared light in superconducting quantum circuits". In: *Applied Physics Letters* 99.11 (2011), p. 113507.

[71] J M Kreikebaum et al. "Optimization of infrared and magnetic shielding of superconducting TiN and Al coplanar microwave resonators". In: *Superconductor Science and Technology* 29.10 (Aug. 2016), p. 104002.

[72] David Isaac Schuster. "Circuit quantum electrodynamics". English. 3267357. PhD thesis. United States – Connecticut, 2007, p. 252. ISBN: 978-0-549-06717-7.

[73] Crispin W Gardiner and Peter Zoller. *Quantum Noise A Handbook of Markovian and Non-Markovian Quantum Stochastic Methods with Applications to Quantum Optics*. Springer, 2010. ISBN: 978-3-540-22301-6.

[74] S. Krinner et al. "Engineering cryogenic setups for 100-qubit scale superconducting circuit systems". In: *EPJ Quantum Technology* 6.1 (May 2019), p. 2. ISSN: 2196-0763.

[75] G. Ithier et al. "Decoherence in a superconducting quantum bit circuit". In: *Phys. Rev. B* 72 (13 Oct. 2005), p. 134519.

[76] C. Macklin et al. "A near–quantum-limited Josephson traveling-wave parametric amplifier". In: *Science* 350.6258 (2015), pp. 307–310.

[77] Leandro Stefanazzi et al. "The QICK (Quantum Instrumentation Control Kit): Readout and control for qubits and detectors". In: *Review of Scientific Instruments* 93.4 (2022), p. 044709.

[78] Yves Salathé et al. "Low-Latency Digital Signal Processing for Feedback and Feedforward in Quantum Computing and Communication". In: *Phys. Rev. Appl.* 9 (3 Mar. 2018), p. 034011.

[79] J.P.G. van Dijk et al. "Impact of Classical Control Electronics on Qubit Fidelity". In: *Phys. Rev. Appl.* 12 (4 Oct. 2019), p. 044054.

[80] Harrison Ball, William D Oliver, and Michael J Biercuk. "The role of master clock stability in quantum information processing". In: *npj Quantum Information* 2.1 (2016), p. 16033.

[81] Shlomi Matityahu et al. "Dynamical decoupling of quantum two-level systems by coherent multiple Landau–Zener transitions". In: *npj Quantum Information* 5.1 (2019), p. 114.

[82] Zijun Chen and John M. Martinis. "Metrology of Quantum Control and Measurement in Superconducting Qubits". Ph.D. United States – California: University of California, Santa Barbara, 2018, p. 241. ISBN: 978-0-355-73637-3.

[83] Daniel Thomas Sank and John M. Martinis. "Fast, Accurate State Measurement in Superconducting Qubits". Ph.D. United States – California: University of California, Santa Barbara, 2014, p. 229. ISBN: 978-1-321-35005-0.

[84] Evan Jeffrey et al. "Fast Accurate State Measurement with Superconducting Qubits". In: *Phys. Rev. Lett.* 112 (19 May 2014), p. 190504.

[85] Iavor I. Boradjiev and Nikolay V. Vitanov. "Control of qubits by shaped pulses of finite duration". In: *Phys. Rev. A* 88 (1 July 2013), p. 013402.

[86] Mostafa Khezri et al. *Measurement-Induced State Transitions in a Superconducting Qubit: Within the Rotating Wave Approximation*. 2022.

[87] X. Y. Jin et al. "Thermal and Residual Excited-State Population in a 3D Transmon Qubit". In: *Phys. Rev. Lett.* 114 (24 June 2015), p. 240501.

[88] Peter W. Shor. "Scheme for reducing decoherence in quantum computer memory". In: *Phys. Rev. A* 52 (4 Oct. 1995), R2493–R2496.

[89] Austin G. Fowler et al. "Surface codes: Towards practical large-scale quantum computation". In: *Phys. Rev. A* 86 (3 Sept. 2012), p. 032324.

[90] Emanuel Knill, Raymond Laflamme, and Wojciech H. Zurek. "Resilient quantum computation: error models and thresholds". In: *Proceedings of the Royal Society of London. Series A: Mathematical, Physical and Engineering Sciences* 454.1969 (1998), pp. 365–384.

[91] Joe O'Gorman and Earl T. Campbell. "Quantum computation with realistic magic-state factories". In: *Phys. Rev. A* 95 (3 Mar. 2017), p. 032338.

[92] Peter W. Shor. "Polynomial-Time Algorithms for Prime Factorization and Discrete Logarithms on a Quantum Computer". In: *SIAM Journal on Computing* 26.5 (1997), pp. 1484–1509.

[93] Rajeev Acharya et al. "Suppressing quantum errors by scaling a surface code logical qubit". In: *Nature* 614.7949 (Feb. 2023), pp. 676–681. ISSN: 1476-4687.

[94] Pablo Esquinazi, ed. *Tunneling Systems in Amorphous and Crystalline Solids*. Springer Berlin Heidelberg, 1998.

[95] J. Jäckle. "On the ultrasonic attenuation in glasses at low temperatures". In: *Zeitschrift für Physik A Hadrons and nuclei* 257.3 (1972), pp. 212–223.

[96] Hanhee Paik et al. "Observation of High Coherence in Josephson Junction Qubits Measured in a Three-Dimensional Circuit QED Architecture". In: *Phys. Rev. Lett.* 107 (24 Dec. 2011), p. 240501.

[97] J. Wenner et al. "Surface loss simulations of superconducting coplanar waveguide resonators". In: *Applied Physics Letters* 99.11 (Sept. 2011), p. 113513. ISSN: 0003-6951.

[98] Shingo Kono et al. *Mechanically Induced Correlated Errors on Superconducting Qubits with Relaxation Times Exceeding 0.4 Milliseconds*. 2023.

[99] Alexander P. M. Place et al. "New material platform for superconducting transmon qubits with coherence times exceeding 0.3 milliseconds". In: *Nature Communications* 12.1 (2021), p. 1779.

[100] Chenlu Wang et al. "Towards practical quantum computers: transmon qubit with a lifetime approaching 0.5 milliseconds". In: *npj Quantum Information* 8.1 (2022), p. 3.

[101] G. Andersson et al. "Acoustic spectral hole-burning in a two-level system ensemble". In: *npj Quantum Information* 7.1 (2021), p. 15.

[102] Naftali Kirsh et al. "Revealing the nonlinear response of a tunneling two-level system ensemble using coupled modes". In: *Phys. Rev. Mater.* 1 (1 June 2017), p. 012601.

[103] Martin Spiecker et al. "Two-level system hyperpolarization using a quantum Szilard engine". In: *Nature Physics* 19.9 (2023), pp. 1320–1325.

[104] Liang Xiang et al. *Quantify the Non-Markovian Process with Intervening Projections in a Superconducting Processor*. 2021.

[105] Guido Burkard. "Non-Markovian qubit dynamics in the presence of $1/f$ noise". In: *Phys. Rev. B* 79 (12 Mar. 2009), p. 125317.

[106] Kartiek Agarwal et al. "Polaronic model of two-level systems in amorphous solids". In: *Phys. Rev. B* 87 (14 Apr. 2013), p. 144201.

[107] L. B. Ioffe et al. "Decoherence in Superconducting Quantum Bits by Phonon Radiation". In: *Phys. Rev. Lett.* 93 (5 July 2004), p. 057001.

[108] Yaniv J. Rosen et al. "Protecting superconducting qubits from phonon mediated decay". In: *Applied Physics Letters* 114.20 (May 2019), p. 202601. ISSN: 0003-6951.

[109] Andrew J. Keller et al. "Al transmon qubits on silicon-on-insulator for quantum device integration". In: *Applied Physics Letters* 111.4 (July 2017), p. 042603. ISSN: 0003-6951.

[110] Jürgen Lisenfeld et al. "Electric field spectroscopy of material defects in transmon qubits". In: *npj Quantum Information* 5.1 (2019), p. 105.

[111] Yoni Shalibo et al. "Lifetime and Coherence of Two-Level Defects in a Josephson Junction". In: *Phys. Rev. Lett.* 105 (17 Oct. 2010), p. 177001.

[112] Mo Chen et al. *Phonon engineering of atomic-scale defects in superconducting quantum circuits*. 2023.

[113] Gregory S. MacCabe et al. "Nano-acoustic resonator with ultralong phonon lifetime". In: *Science* 6518 (), pp. 840–843.

[114] H.J. Mamin et al. "Merged-Element Transmons: Design and Qubit Performance". In: *Phys. Rev. Appl.* 16 (2 Aug. 2021), p. 024023.

[115] Carole Addis et al. "Dynamical decoupling efficiency versus quantum non-Markovianity". In: *New Journal of Physics* 17.12 (Dec. 2015), p. 123004.

[116] K. Khodjasteh and D. A. Lidar. "Fault-Tolerant Quantum Dynamical Decoupling". In: *Phys. Rev. Lett.* 95 (18 Oct. 2005), p. 180501.